

**HARD SURFACE COATING EXPERIMENTAL EVALUATION AND
THERMOMECHANICAL ANALYSIS OF A SEAL WITH MICRO
HEAT EXCHANGER**

A Thesis

Submitted to the Graduate Faculty of the
Louisiana State University and
Agricultural and Mechanical College
In partial fulfillment of the
Requirements for the degree of
Master of Science in Mechanical Engineering

In

The Department of Mechanical Engineering

by

Yifan Qiu

B.Engr., University of Science and Technology, Beijing, 1994

May 2002

ACKNOWLEDGEMENT

During the writing of this thesis, the author received many helps from the persons whom he would like to thank.

First of all, I would like to thank my major professor Dr. Michael Khonsari for all his help and advise during all of the works toward this thesis.

Secondly, I wish to thank Dr. Wenjin Meng, for his timely help, especially for his allowance for using his valuable coating apparatus and serving on the thesis committee along with Dr. Y. Ram.

I would also thank Mr. Bao Feng, for his kindly help in coating all the samples necessary for the experiments.

Finally, my parents and my sister are always my firmest support through all of my life. I would also give my thanks to them.

The author gratefully acknowledges the support of Louisiana Board of Regents (Grant number: LEQSF(2000-03)-RD-02) under the Industrial ties program for a project entitled "Novel Design, Testing and Analysis of Bearings and Seals."

TABLE OF CONTENTS

ACKNOWLEDGEMENTS	ii
LIST OF TABLES	v
LIST OF FIGURES.....	vi
ABSTRACT	x
CHAPTER 1 INTRODUCTION	1
1.1 Overview	1
1.2 Mechanical Seal	2
1.3 Previous Work Directed to Improve the Mechanical Seal Performances.....	11
1.4. Research Objectives	13
1.5 Thesis Outline	14
CHAPTER 2 THIN FILM COATING ON THE END SURFACE OF A RING	16
2.1 Coating Methods In The Research.....	16
2.2 Coating Procedure And Equipment	20
CHAPTER 3 TRIBOLOGICAL TESTS OF TI-C:H COATED RING ON DISK	24
3.1 Mechanical and Tribological Properties of Coatings	24
3.2 Testing Equipment and Procedure	28
3.3 Test Result and Discussion	31
3.3.1 Long duration dry test	31
3.3.2 Short Duration Dry Test	36
3.3.4 Discussion	41
CHAPTER 4 MANUFACTURING OF MICRO HEAT EXCHANGER	46
4.1 Propose	46
4.2 LIGA and Electroplating	47
4.3 Manufacturing of Micro Heat Exchanger	50
4.3.1 Dimensions and Materials	50
4.3.2 LIGA Process	51
4.3.3 Seal Assembly	54
CHAPTER 5 STRUCTURAL AND THERMAL ANALYSIS OF MICRO HEAT EXCHANGER	55
5.1 Previous Experiment Introduction	55
5.1.1 Testing Devices	55
5.1.2 Testing Input and Output	56
5.2. Transient Temperature Distribution Calculation	57
5.2.1 Abstraction of the problem	57
5.2.2 Heat Generation	59

5.2.3 Convection Heat Transfer Coefficient	61
5.2.4 Formulation of The Problem	65
5.2.5 Geometric Modeling	67
5.3 Posts Strength Calculation	69
5.3.1 Introduction	69
5.3.2 Method For Calculating Stress From Friction Torque	70
5.3.2.1 Friction Torque	70
5.3.2.2 Stress In The Seal Structure	71
5.3.2.3 Changing Posts Rectangle Distribution To Concentric Distribution	75
5.3.2.4. Method For The Calculation of Maximum Friction Torque	76
5.3.3 Matlab Code for Calculation of Stress Distribution of the Seal Structure	77
5.4 Result and Discussion	77
5.4.1 Post Structural Analysis	77
5.4.1.1 Maximum post stress under friction torque.....	77
5.4.1.2 Maximum Normal force for Seal structures with posts	81
5.4.2 Transient Heat Transfer Calculation	82
5.4.2.1 Comparison between Calculation and Experimental results	82
5.4.2.2 Relationship between Post Density And Steady State Temperature	87
5.4.2.3 Nondimensionalization of The Heat Transfer Problem	90
CHAPTER 6 SUMMARY AND CONCLUSION	95
6.1 Summary	95
6.2 Recommendations of Future Work	96
REFERENCES	97
APPENDIX 1: FLEXPDE CODE FOR MICRO HEAT EXCHANGER HEAT TRANSFER CALCULATION	99
APPENDIX 2: MATLAB CODE 1	105
APPENDIX 3: MATLAB CODE 2	107
APPENDIX 4: CALCULATION OF WEAR RATE	109
VITA	111

LIST OF TABLES

Table 1.1 Typical PV limits of materials	5
Table 1.2 PV limits of material pairs	6
Table 2.1(a) Parameters for different steps in Ti-C:H coating	23
Table 2.1(b) Ti gun current for coating samples	23
Table 3.1 Resolutions of several wear measurement techniques	27
Table 3.2 Test settings for long duration dry test	31
Table 3.3 Result of long duration dry tests	37
Table 3.4 Result of short duration dry tests	37
Table 4.1 Design parameters of seal prototype (design #1: high post density) [Kountouris, 1999]	52
Table 4.2 Design parameters of seal prototype (design #2: low post density) [Kountouris, 1999]	52
Table 5.1 Properties of rotating mating rings [Kountouris, 1999]	56
Table 5.2 Wear tests input parameters [Kountouris, 1999]	57
Table 5.3 Coefficients in equation 5.6 [Zukauskas, 1972]	62
Table 5.4 Input parameter for stress calculation	77
Table 5.5 Different post distributions	78
Table 5.6 Calculation results for posts' stresses	79
Table 5.7 Post density and maximum load capacity.....	81
Table 5.8 Parameters in heat transfer calculation	83
Table 5.9 Post density and steady state temperature	87

LIST OF FIGURES

Figure 1.1 Mechanical seal component [R. H. Warring 1981]	3
Figure 2.1 Evaporation deposition process schematic [Bunshah, R. F, 2000]	17
Figure 2.2 Typical sputter deposition system [Bunshah, R. F, 2000]	18
Figure 2.3 Radial-Flow plasma enhanced CVD reactor [Bunshah, R. F, 2000] ...	16
Figure 2.4 Deposition system used in present research	20
Figure 2.5 Deposition chamber layout [Feng, B, 2001]	21
Figure 2.6 The sample holder	22
Figure 3.1 Typical sliding tests geometries [Bushan,B. 1999]	26
Figure 3.2 CETR micro tribometer	28
Figure 3.3 The experiment setup	29
Figure 3.4 (a) Friction torque vs. time for coating produced under 0.2 amp Ti cathode current	32
Figure 3.4 (b) Friction torque vs. time for coating produced under 0.4 Amp Ti cathode current	32
Figure 3.4 (c) Friction torque vs. time for coating produced Under 0.6 amp Ti cathode current	33
Figure 3.4 (d) Friction torque vs. time for coating produced Under 0.8 amp Ti cathode current	33
Figure 3.4 (e) Friction torque vs. time for coating produced under 1.0 amp Ti cathode current	34
Figure 3.4 (f) Friction torque vs. time for coating produced under 1.2 amp Ti cathode current	34
Figure 3.4 (g) Friction torque vs. time for coating produced under 1.4 amp Ti cathode current	35
Figure 3.4 (h) Friction torque vs. time for coating produced	

under 1.6 amp Ti cathode current	35
Figure 3.4 (a) Friction torque vs. time for coating produced Under 0.2 Amp Ti Cathode Current In Short Duration Test	38
Figure 3.5 (b) Friction torque vs. time for coating produced under 0.4 amp Ti cathode current in short duration test	38
Figure 3.5 (c) Friction torque vs. time for coating produced under 0.6 amp Ti cathode current in short duration test	39
Figure 3.5 (d) Friction torque vs. time for coating produced under 0.8 amp Ti cathode current in short duration test	39
Figure 3.5 (e) Friction torque vs. time for coating produced under 1.0 amp Ti cathode current in short duration test	40
Figure 3.5 (f) Friction torque vs. time for coating produced under 1.2 amp Ti cathode current in short duration test	40
Figure 3.5 (g) Friction torque vs. time for coating produced . under 1.4 amp Ti cathode current in short duration test	41
Figure 3.5 (h) Friction torque vs. time for coating produced under 1.6 amp Ti cathode current in short duration test	41
Figure 3.6 Composition of a series of ti-c:h coatings in atomic fraction as a function of ti cathode current. [Cao, D. et al, 2001]	42
Figure 3.7 Average friction coefficient of the coating materials, wear rate of the mating material vs. Ti cathode current	43.
Figure 3.8 Wear scars of the coating produced under 1.6 amp Ti cathode current after 1600s of unlubricated ring-on-disk test	45
Figure 4.1 Typical LIGA process [Madou, M.J. 1997]	49
Figure 4.2 Last steps of LIGA process [Madou, M.J. 1997]	50
Figure 4.3 Seal prototype assembly drawing [Kountouris, D, 1999]	51
Figure 4.4 Fixture used in electroplating the micro heat exchanger structure [Kountouris, D, 1999]	53
Figure 5.1 Wear test equipment [Kountouris, 1999]	55

Figure 5.2 Outlook of seal prototype [Kountouris, 1999]	57
Figure 5.3 Domains of the system	58
Figure 5.4 Tubes arrangement (a) in-line (b) staggered	62
Figure 5.5 Correction factor for tube banks consisting 16-20 rows [Zukauskas, 1972]	63
Figure 5.6 Boundaries of the system	65
Figure 5.7 Geometry model of the problem	67
Figure 5.8 Schematic of posts distribution and its transformation in building the geometry model	69
Figure 5.9 Seal prototype and its three layer of components: (1) top layer (2) micro post layer (3) bottom layer	70
Figure 5.10 Force and moment on a single post	74
Figure 5.11 Post distribution transformation	75
Figure 5.12 Post model meshed and loaded	78
Figure 5.13 Contour plot of Von Mises stress distribution of a post	80
Figure 5.14 Von Mises stress vs. post density	80
Figure 5.15 (a) Temperature variation with time for no coolant situation	83
Figure 5.15 (b) Temperature variation with time for coolant flow rate of $6.7E-4$ kg/s	84
Figure 5.15 (c) Temperature variation with time for coolant flow rate of $1.19E-3$	84
Figure 5.15 (c) Temperature variation with time for coolant flow rate of 2 kg/s	85
Figure 5.16 Temperature time responses for post density from 1 to 12.31 posts/mm ²	88
Figure 5.17 Post density and seal steady statetemperature	89
Figure 5.18 Temperature-Time curve of seal without micro	

heat exchanger	89
Figure 5.19 Non-dimensionalized temperature variation with time for different coolant flow rate	92
Figure 5.20 Dimensional temperature variation with time for different coolant flow rate	93
Figure 5.21 Dimensional temperature variation with time for different seal dimensions	94
Figure A1 Typical wear groove cross-section obtained from stylus profiler	109

ABSTRACT

Mechanical face seals are important components of many rotating machinery. Minimizing the friction between seal faces and efficiently removing the heat generated between seal surfaces are two crucial considerations in the design of mechanical seal. Thin film coating and MEMS technology hold great promise for improving the performance of mechanical seals from the viewpoint of reducing friction and heat at the interface in these two aspects. To reveal what effect the coating and MEMS technology can have on tribological properties of seals, friction and wear characteristics of Ti-C:H coatings on seal-like rings and heat transfer performances of a seal prototype implanted with micro heat exchangers were studied in this thesis. Implanted micro-heat exchangers were built using the MEMS technology in a previous work.

Coating on seal-like rings was successfully implemented using CVD/PVD. Friction and wear properties of coatings with different compositions were investigated through a series of unlubricated ring-on-disk experiments in a tribometer. The results showed the Ti-C:H coatings tend to improve the tribological performance. However, the experimental results did not reveal a direct relationship between coating composition and its tribological properties.

Micro posts implanted seal prototype had been manufactured and tested in a previous work. In the present study, a finite element model was developed to simulate the experiment and evaluate the heat transfer characteristic of the seal prototype. The predictions of the model are in good agreement with the measured results. In addition, a method was developed for the calculation of the seal structure's maximum stress under

normal friction load. This method can be used for the structural analysis and failure prediction of seals with micro posts.

CHAPTER 1

INTRODUCTION

1.1 Overview

Tribology - the science of lubrication, friction and wear - has begun to extend its scope into more and more newly developed technologies. Among them, surface engineering and Micro Electro-Mechanical System (MEMS) are two of the most popular subjects.

MEMS originally referred to as the microscopic mechanical elements fabricated on silicon chips. The implementation techniques were similar to those utilized in integrated circuit manufacture for use as sensors, actuators, and other devices. Now, MEMS includes almost all types of micro devices [Madou, 1997]. One of the applications of micro devices is for building High-Aspect-Ratio Microstructures (HARMs), which are a class of microstructures with very high characteristic lateral dimensions to height ratio. Because of their high surface area to volume ratio, the application of this kind of microstructures in heat transfer field as heat exchangers is very promising [Stephens, 2001].

Adding heat exchangers in seals and bearings, where heat is generated between frictional surfaces, can be beneficial in order to remove heat and thus reduce wear. As can be seen later (chapters 4, 5), a large array of micro posts with height in the order of magnitude of millimeter and diameter of hundreds of micrometers can be electroplated underneath the seal surfaces. Experimental tests on a prototype have demonstrated the feasibility of this technology for improving the performance of a mechanical seal [Kountouris, 1999]. As part of this thesis, a finite element model is developed to

analyze the thermal properties of the seal prototype with implanted micro heat exchanger. Also, a method is developed to calculate the strength of the seal's structure.

The modern technologies used for improving the surface properties include coatings and surface treatments. Surface treatments can be classified as thermal treatments, mechanical treatment, diffusion and implantation. Coatings include hard coating and soft coatings. Techniques used to produce coatings are thermal spray, welding, cladding physical vapor deposition (PVD), chemical vapor deposition (CVD), physical chemical vapor deposition and so on [Bhushan, 1999]. A special coating device was developed in LSU Mechanical Department that integrates reactive magnetron sputter deposition and inductively coupled plasma assisted hybrid PVD/CVD, and enables one to deposit various compositions on different substrates. Experimental measurements have revealed that by coating a thin layer of the hard coating, such as TiN, Si_3N_4 , on the contacting surface of a seal, wear and friction can be significantly reduced [Peterson and Winner, 1980]. In this research titanium-containing hydrocarbon coatings are deposited on steel rings surfaces and their tribological properties are measured by.

1.2 Mechanical Seal

Seals are devices used in mechanical systems to avoid leakage of lubricant or process fluid from the systems or contamination of the systems from the environment [Bhushan, 1999]. Generally, seals are categorized into static and dynamic. The former is used where there is no relative movement between components. The latter is applied in places where sealing is required between surfaces with relative sliding such as between rotating shaft and the housing. Mechanical seals with their formal name as mechanical face seals belong to dynamic seals because they use a rotating component and a

stationary component to rub against each other in their contacting surfaces to form a sealing that closes the gap between a rotating shaft and the housing. Figure 1.1 shows the components of a conventional mechanical seal. A rotating seal ring with its own secondary seal with a driving mechanism is located on the shaft and rotates with it at the same speed. A stationary sealing ring with its secondary seal is installed on a gland or integral stuffing box cover against rotating ring. A pressing mechanism (such as a spring) is used to keep the rotating surface on the stationary surface to avoid leaking [Warring, 1981].

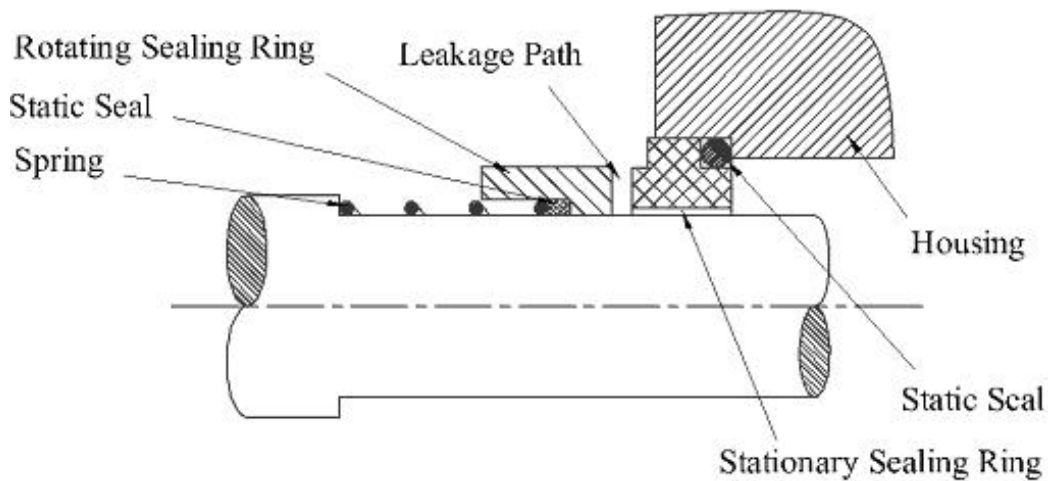


Figure 1.1 Mechanical seal components [Warring, 1981]

Great care should be taken in selecting seal materials and materials combinations to prevent leakage and minimize the friction and wear. Seal materials should have the following properties [Buck, 2001]:

- a. They must be wear resistant.
- b. They should have low coefficient of thermal expansion.
- c. They must have high overall strength.

- d. They should have good thermal properties, such as high thermal conductivity, to remove heat generated from the rubbing surfaces.
- e. They should have good resistant to corrosion from both inside and outside environment.
- f. They should be easy to manufacture and have low cost.

Material pairs used in seal assemblies are usually different in order to maintain an optimum operation result in terms of friction and wear. The selection of the material pairs should be made according to the following considerations [Buck, 2001]:

- a. A soft material and a hard material referred to as “hard face” and “soft face” are often used. The hardness difference between two materials is usually 20%.
- b. Low friction coefficient between rotating material and stationary material is needed to decrease the heat generation at the interface and thus reduce thermal expansion.
- c. The two materials should have high modulus of elasticity difference so that the stiffer material will be able to run into the softer one to make good sealing.

Wide varieties of materials are used as seal face materials in practice. For “hard faces,” materials range from plain stainless steel, lead bronze, Ni-resist to tungsten carbide and silicon carbide. The counter-face materials are mostly made with carbon composition with metal or resin filler.

Because of its direct relation to wear, the PV (pressure times linear velocity) value at the interactive surfaces is crucial in determining the performance of a mechanical seal.

For a circular surface, the PV value can be estimated by:

$$PV = \frac{W}{A} \mathbf{p} n r_{av} \quad (1.1)$$

where W is the normal load, A is the apparent surface area, n is the rotating speed, and r_{av} is the average diameter relative to the contacting surface. The PV limit is the maximum PV value that the material of a seal can sustain before it degrades by frictional heating. When a seal face operates beyond its PV limits, either temperature of the contacting surfaces will rise without reaching a steady state or the wear rate of the surfaces will increase substantially and become non-uniform. Some typical PV limits are list below:

Table 1.1 Typical PV limits of materials [Peterson and Winner, 1980]

Face materials Pair Rotating / Stationary	Face Material PV limits (kpsi. ft/min)
Carbon-graphite / Ni-resist	100 (3,540 kPa.m/s)
Carbon-graphite / Ceramic	100 (3,540 kPa.m/s)
Carbon-graphite / Tungsten carbide	500 (17,700 kPa.m/s)
Carbon-graphite / Silicon carbide	500 (17,700 kPa.m/s)
Carbon-graphite / Carbon-graphite	50 (1,770 kPa.m/s)
Ceramic / ceramic	10 (254,000 kPa.m/s)
Tungsten carbide/Tungsten Carbide	120 (4,248,000 kPa.m/s)
Silicon carbide / Silicon carbide	500 (17,700 kPa.m/s)

As mentioned before, the rotating sealing rings are pressed onto the stationary sealing rings by means of a pressing mechanism. Usually this mechanism is a spring or a bellows system. The standard spring load is normally set to be 30 psi (2×10^5 Pa) in industry. But this may not be the actual contact pressure on the rubbing surfaces if the seal is not hydraulically balanced. The hydraulic balance is the relation between seal faces contact pressure and pressure of the fluid. If the seal is unbalanced, besides the spring pressure, extra pressure from the fluid will also act on the seal. As a result, the contact pressure on the seal surfaces will be either greater than the desired pressure, causing extra heat and wear, or will be smaller than the pressure that is needed to close

the gap and avoid excessive leakage. A seal should be designed so that the hydraulic pressure on both sides of the seal rings counteract with each other so that very little (ideally zero) extra pressure would be transferred to the contacting surfaces. A seal designed in this fashion is called a balanced seal. With a balanced seal, the hydraulic pressure of the fluid will not affect the seal contacting pressure to make it more easily controlled. As a result, the seal wear is minimized, there is less heat generation at the surface, and the seal's life becomes longer. Table 1.2 shows the comparison of seals' *PV* duty limits (the maximum fluid pressure that a seal can sustain) of some typical materials with balanced and unbalanced structure. The operating *PV* limits are much greater for balanced seal than unbalanced ones.

Table 1.2 PV limits of material pairs [Warring, 1981]

Face materials Pair	Face Material PV limits $\cdot 10^5$ (Pa m/s)			
	Water and Aqueous solutions		Other Fluids	
	Unbalanced seals	Balanced seals	Unbalanced seals	Balanced seals
Stainless steel/Carbon	5.5	-	30	-
Lead bronze/Carbon	23	-	36	-
Stellite/Carbon	49	85	52	580
Chrome oxide/Carbon	70	440	-	-
Alumina ceramic/Carbon	36	250	88	420
Tungsten carbide/Tungsten Carbide	44	500	71	420
Tungsten carbide/Carbon	70	700	88	1225

Seals seldom run dry where operated properly. Unless specifically designed for dry operation, there should always be a lubricant film between seal surfaces. The lubrication regime can be categorized as mixed lubrication with both properties of

hydrodynamic/elastohydrodynamic (HD/EHD) and boundary lubrication. To maintain an adequate thickness of the lubricant film, the seal surface temperature should be carefully controlled to avoid lubricant to vaporization or boiling away. Also, if there is excessive heat generation between seal faces, some carbon seal faces may be damaged by either melting their fillers or causing the air pockets below the surface to expand. If hard coating is applied on the seal face, the heat-induced temperature changes may produce cracks due to different thermal expansion coefficient of the coating and the substrate. Heat may also cause large temperature gradients in the seal material, which can result in distorting the lapped seal surfaces. Consequently, the contact area will decrease and both seal surfaces will wear quickly. Therefore, heat control is a significant problem in seal design and application. The details of heat generation between seal surfaces will be discussed in chapter 5.

To acquire low friction between seal faces, good surface roughness and flatness should be ensured. Typically, the seal face is lapped to less than three helium light bands (slightly less than one micrometer) [Peterson and Winner, 1980]. When the surfaces are not well lubricated, because of the pressure and low surface roughness, the surfaces tend to “stick” to each other. Then upon applying torque on the shaft, the attached surface will make a sudden separation. This causes the actual rotating speed of the seal faces to fluctuate widely. In tribology, this phenomenon is called stick slip. It may result in very severe vibration, which will damage the seal faces and cause excessive seal leakage.

How to minimize the wear on seal faces is one of the central problems in seal design. Like many other mechanical components, the modes of wear for seal faces can be

categorized into four basic forms. They are: adhesion, abrasion, corrosion and surface fatigue.

Adhesive wear occurs when two seal surfaces rub in sliding contact. Since the two surfaces contact through small asperities, adhesion occurs between these asperities. When load is applied, there will be high shear stresses at the points of contact. Since the contact areas are very small, the local stresses can reach one or both of the materials' yield stress very rapidly causing plastic deformation. Hence, surface contaminant, if any exists, at the contact area will be removed and the contact area will be "cleaned." This "cleaning" action caused by plastic deformation, along with high contact stress, may result in "cold welding" junctions at the contact locations. The detachment of fragment from one of the bodies will occur in the welded junction. The detached particles will either attach themselves to the counterpart surface or become loose particles. As this process progresses, the particles may transfer back and forth between two materials or come out of the rubbing area [Merchant, 1940].

Usually, the adhesive wear is the prevalent mode of wear among all other wear modes. It can be expressed in the following equation known as Archard's equation [Bhushan, 1999]:

$$v = \frac{kWx}{H} \quad (1.2)$$

where v is the volumetric wear of one of material, W is the applied load, x is the relative sliding distance, H is the hardness of the material being worn away, and k is the adhesive wear coefficient. For mechanical seals we can rewrite equation (1.2) as:

$$v = \frac{kPVt}{H} A_0 \quad (1.3)$$

where P is the nominal pressure on the surfaces, V is the sliding velocity, t is the sliding time, and A_0 is the contacting surface area. Here, the PV value appears as a function of wear and is considered to be an important factor in the selection of seal materials.

Abrasive wear is a form of a damage caused by asperities of a hard surface or particles sliding on a softer surface and making a plastic deformation and fracture at the interface. Two situations may occur for abrasive wear [Bisson, 1969]: 1) the hard surface is the harder of the two rubbing surfaces or 2) the harder surface is a third body, which is usually a small particle of abrasive or grit caught between the two surfaces and is hard enough to abrade one or both of the surfaces. In the case of mechanical seal, both situations can occur. Because the materials are chosen so that one material is softer and the other is harder, the first situation may happen. During the operation, the adhesive wear will occur first and generate small particles, which may be trapped between the rubbing surfaces. Then, the second situation will happen. Wear volume from abrasive wear by deformation can be determined using similar equation as Archard's equation [Bhushan, 1999]:

$$v = \frac{k_{abr} Wx}{H} \quad (1.4)$$

where k_{abr} is the coefficient of abrasive wear. Abrasive wear by fracture can be determined using the following expression: [Evans and Marshall, 1981]

$$v = a_3 N \frac{(E/H)(W')^{9/8}}{K_c^{1/2} H^{5/8}} \quad (1.5)$$

where a_3 is a material dependent constant, N is the number of asperities contacting the surface been worn, W is the individual load carried by the asperities, E is the module of elasticity of the material, and K_c is material's fracture toughness.

Corrosive wear is a chemical process and occurs when seal surfaces contact with corrosive materials such as oxygen in the air, water and oil. Generally, corrosion takes place before sliding of the faces. In other words, the corrosive wear will occur before adhesive wear. However, the corrosive process will slow down after a thin layer of corrosion is formed. When the rubbing of the surfaces starts, the layer of corrosion will be removed by the physical processes of wear. The corrosive action will then be able to continue. Corrosion is heavily dependent on the environment and the nature of material. If a mechanical seal operates in open air, a thin film of lubricant can both reduce the severity of the rubbing process and act as a protective layer against corrosion [Bhushan, 1999; Bisson, 1969]. If operating in a corrosive environment, such as seals in pumps for precessing seawater or some chemical fluid, proper material should be selected to avoid corrosive wear.

The last type of wear, fatigue wear, is originated from sliding at the interface of the seal. The sliding can cause repeated loading and unloading cycles in certain areas of the seal material, which will induce the formation of cracks on the sliding surface or subsurface. When the number of cycles goes beyond the critical point, the material in the crack area will break up into particles leaving small pits on the seal faces. Therefore, fatigue wear is a function of number of loading cycles [Bhushan, 1999].

None of these types of wear can take place by itself. Most of the time, wear involves two or more wear modes. Fretting or fretting corrosion is an example of such wear

combination. It is a mixture of adhesive, corrosive, and abrasive wear. It occurs when there are small amplitudes of vibration in tangential direction between contacting surfaces. The normal load and vibration result in adhesion between asperities and abrasion of surfaces, producing wear debris. When, as in more common situations, corrosion is involved, the newly worn surfaces and the debris will corrode, causing corrosive wear. This process will probably occur when seals are at rest [Rabinowicz, 1965].

In general, the goal in design and manufacturing of a mechanical seal is to find a proper combination of seal structure, material, surface treatment and operation environment to achieve a low leakage, long life, reliable seal. For this purpose the friction between seal surfaces must be minimized and the removal of the heat generated from friction should be maximized.

1.3 Previous Work Directed to Improve the Mechanical Seal Performances

While the overall arrangement of mechanical seal systems has remained nearly the same for many years, a lot of improvements have been made by way of changing the individual components of the seals. For example, hydraulically balanced seal design have been widely implemented by changing the seal rings shape. Dual seals, which consist of two stationary and two rotating rings, have been used where no leakages is permitted. The focus of the research on seal performance improvement has been on seal rings improvement to reduce leakage and heat generation.

On the mechanical face seal surface properties improvement, Etsion et al. (1999) developed an analytical model to predict the relation between the opening force and operating conditions in a mechanical seal with laser textured micro surface structure in

the form of micro pores. The mode can be implemented in any shape of micro pores and was used for the optimization of spherical shape micro-pores evenly distributed on one of the mating rings face to maximize the opening force and fluid film stiffness.

Kelly et al. (2001) deposited polycrystalline diamond coating onto silicon carbide substrates (seal material) by microwave plasma-assisted CVD. Tribological performance of the coatings against a range of counterface materials in a thrust washer test rig was carried out using Taguchi experiment. The result confirms the excellent tribological performance of the coatings.

Heinrich et al. (1991) analyzed the influence of the microstructure of sliding surfaces on the tribological behavior of mechanical seals. Different topographies of seal faces made out of silicon-infiltrated silicon carbide were examined on their influences on the behavior of mechanical seals. A variable number of cavities were produced under the seal faces. With this structure, elastohydrodynamic effects could be achieved by creating circumferential convergent gaps that led to an increase in performance of the mechanical seals. Effects of carbon particles introduced into the sliding face material were also investigated. By optimizing the size, shape and amount of the particles increase in seal performance could also be achieved.

On the thermal analysis, Merati et al. (1999) presented a computational model to predict the flow field in the seal chamber and temperature distribution within the stator of a mechanical seal. Nusselt numbers on the wetted surfaces of the seal components were determined using this model for the calculation of seal temperature distribution.

Phillips et al. (1997) experimentally analyzed the impact of thermal distortion of mechanical seal faces has on seal performance. The seal face torque, thermal gradients,

and fluid flow patterns under the normal operating conditions of the seal were measured. Nusselt numbers and heat generations were calculated from the experiment data.

On microstructures and their applications, Marques (1997) introduced a microstructure-covered cylinder in his thesis. Both an analytical model and experimental work were conducted to evaluate the heat transfer ability of the structure. The results indicated that the microstructures enhanced the cylinder's heat transfer significantly and proved the possibility of building microstructures on machine element.

Kountouris (1999) and Stephens et al. (2001) fabricated seal prototypes with micro heat exchangers electro-deposited on their end surface. The prototypes were tested under the similar operating conditions to that for mechanical face seals. The results show a very good improvement in seal's heat transfer capacity.

1.4. Research Objectives

Ti-C:H coating has been successfully applied on substrates like Si wafers and 1045 steel. The properties of coatings themselves were studied [Meng, 2000]; [Cao, 2001]. For a seal assembly, usually this kind of hard coating is applied on one of the seal pairs so that there will be a hardness difference between the two materials. These reports have studied many of the properties of one of the mechanicals seal components. However, the effect of a seal component with coating on its counterpart is still in need of further investigation.

Based on the previous works on the coatings, a part of the current research concentrated on the effects of a coating on its frictional counterpart. A series of cylindrical rings were built and coated with different composition of Ti-C:H coatings

and tested for friction and wear properties through thrust washer tests (ring-on-disk). Thus, the frictional property —friction coefficient — of the coating materials against disk materials were determined. The relationship between the wear of disk material and coating material compositions were also derived.

As mentioned in the last section, Stephens et al. (2001) built a seal prototype with micro heat exchanger. The experimental results showed some good characteristics that improve the overall performance of a mechanical seal. However, the experiments did not reveal the details of thermal properties of the structure. Some theoretical analysis is needed to investigate the seal prototype in detail. Also, building a microstructure beneath the surface of stationary face can weaken the structural integrity of the whole seal structure. A stress analysis was performed to predict failure and optimize the design of the structure in terms of the number of microposts.

In the second part of the current research, a finite element model was developed using a commercially available software package called FLEXPDE to examine the transient heat transfer performances of microstructures. A simple but practical method was developed to calculate the stress distribution on each post in the microstructure. Using the model and method mentioned above, relations between the post density and seal strength and seal heat transfer performances were derived.

1.5 Thesis Outline

Chapter 2 focuses on describing the coating technique used on the end surfaces of a mechanical seal and the coating procedure in the present research. Chapter 3 focuses on the tribological tests of the coating and the analysis for the test result. Chapter 4 focuses on the manufacturing of seal prototype with micro heat exchanger. Chapter 5 presents a

finite element model for transient temperature distribution problem for the micro heat exchanger and the process of calculating the strength of the micro heat exchanger.

Chapter 6 gives the conclusions of the research and suggestions for further research.

CHAPTER 2

THIN FILM COATING ON THE END SURFACE OF A RING

2.1 Coating Methods

As mentioned in the first chapter, one method for changing the seal faces performance is by means of thin film hard coating such as diamond like carbon coating (DLC) by way of vapor deposition. In our case, Ti-C:H is the coating material and Inductively Coupled Plasma assisted hybrid CVD/PVD. Balanced magnetron sputtering is used for the coatings.

There are three main categories of vapor deposition: physical vapor deposition (PVD), chemical vapor deposition (CVD), physical-chemical vapor deposition (PCVD) or plasma-enhanced CVD (PECVD) [Bhushan, 1999]. PVD is the processes of condensing material vapors, which can be created by evaporation, sputtering or laser ablation, onto substrate to form a protective film. CVD is the process of depositing the product of chemical reactions of solid material vapor onto a heated substrate. Thus in CVD, the substrate should be able to withstand high temperature (usually $> 800^{\circ}\text{C}$). PECVD can avoid the high temperature problem by enabling the chemical reaction at or near the room temperature.

Vapor deposition normally includes three steps: first, material should be transferred to vapor phase by evaporation, sputtering or laser ablation, then the vapor phase materials are transported from the source to the substrate. In the last step, the vapor species are condensed onto the substrate and the film is formed by nucleation and growth processes [Bunshah, 2000].

Physical vapor depositions can be divided into two categories: sputtering and evaporation. More detailed classes can be separated from these two categories, such as

thermal evaporation, activated reactive evaporation, glow-discharge sputtering and ion beam sputtering etc. The evaporation is usually carried out in high vacuum (10^{-8} — 10^{-1} torr). The material to be deposited is heated to a temperature of 1000 — 2000°C to create vapor. The vapor pressure ($>10^{-2}$ torr) will then exceed the ambient pressure to make sufficient vapor for the deposition. The substrate can be either preheated to 200 — 1600°C or biased to the desired potential using a DC/RF power supply. Sometimes a proper gas such as argon is introduced to obtain a uniform thickness coating. Figure 2.1 shows the schematic of evaporation deposition process [Bunshah, 2000].

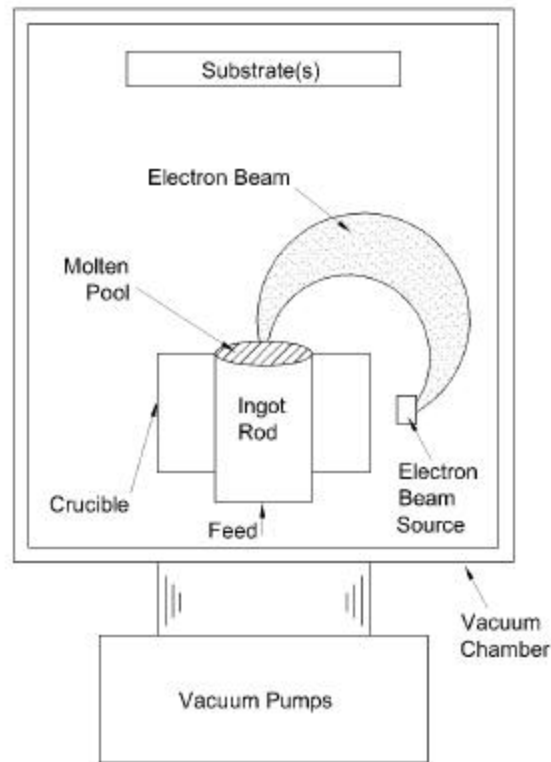


Figure 2.1 Evaporation deposition process schematic [Bunshah, 2000]

Sputtering process is more popular than evaporation. During the process, the atoms or molecules of material to be coated are ejected from the solid surface become vapor

through momentum transfer from energetic particles. A typical pressure of 10^{-4} — 10^{-7} torr is needed for the process. The energetic particles are usually positive ions from heavy inert gases or reactive gases or species for the coating materials. Figure 2.2 shows a simple sputtering system – planar diode sputtering system. The substrate and the sputtered material, which is called target, are positioned facing each other in the vacuum chamber with a distance of 5 to 10 cm. When the sputtered material is ejected, the substrate will intercept the flux of sputtered atoms and the atoms will then be deposited onto the substrate.

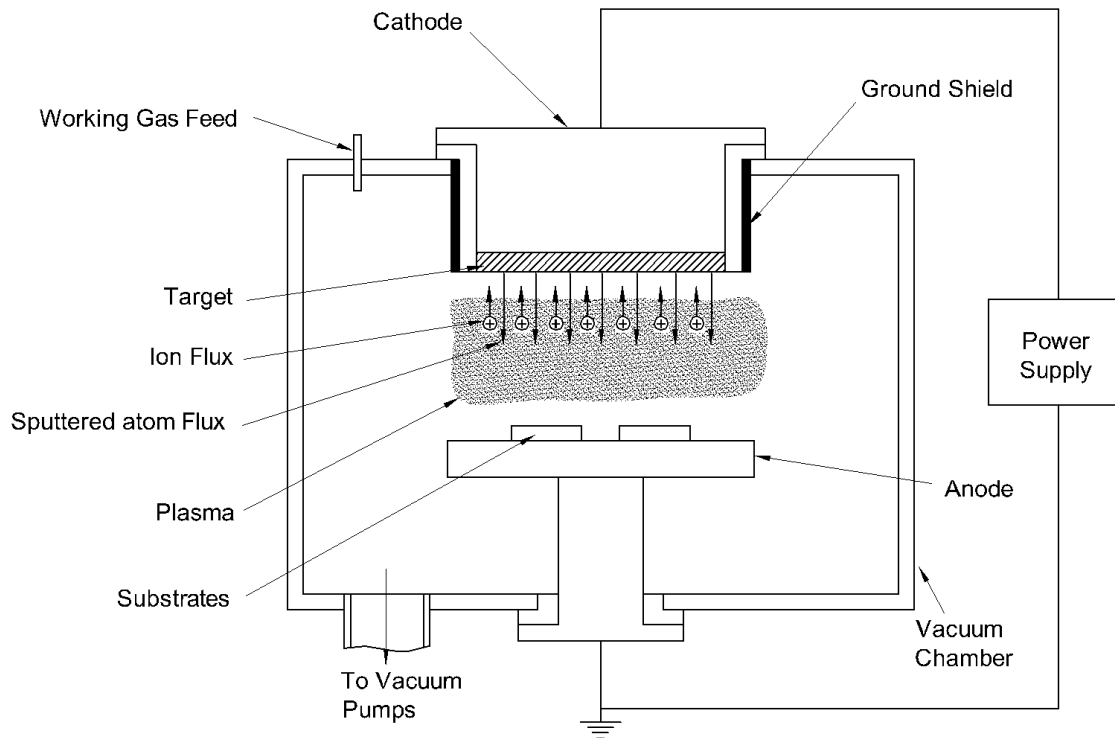


Figure 2.2 Typical sputter deposition system [Bunshah, 2000]

When a magnetic field is used (usually by putting a magnet behind the target) in the sputtering process, the magnetic field, which is not strong enough to effect ions, in front of the cathode and the electric field will trap the electrons. Therefore, the ionization

efficiency near the target can be greatly increased and more electrons will be created out of the surface material. As a result, the sputtering rates will be increased. This method is called magnetron sputtering.

In the chemical vapor deposition process, gaseous chemical reactants will be blown into the reaction chamber. These reactants will be activated to decompose or react on the substrate surfaces to form coatings. The conventional activation method is preheating substrate to reach a temperature of 150 — 2200 °C in order for the reaction to take place. Other activation methods include plasma assisted CVD (PACVD)/plasma enhanced CVD (PECVD) and laser induced CVD. In the current work PACVD/PECVD is used.

PECVD utilizes glow-discharge plasma to activate the CVD process. It is very similar to conventional CVD except that vapor phase reactants react under the assistance of glow-discharge plasma instead of the heating of substrate. Because the high-energy electrons in

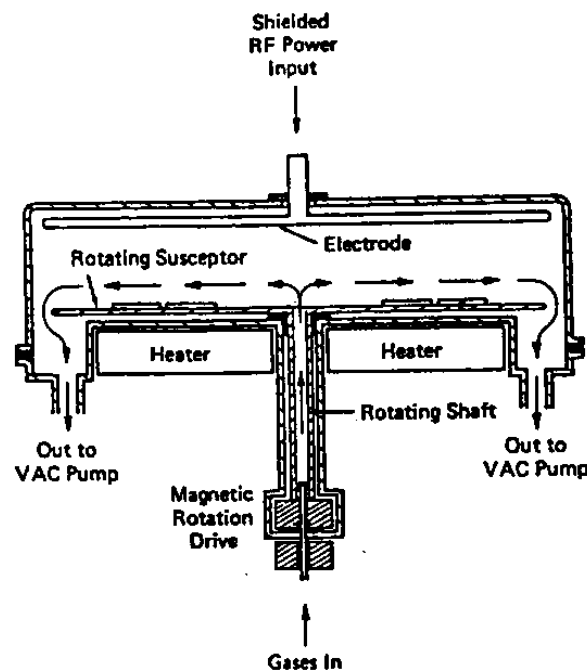


Figure 2.3 Radial-flow plasma enhanced CVD reactor [Bunshah, 2000]

the glow-discharge plasma can break the chemical bond of the reactant molecules and consequently enhanced the chemical reaction, PECVD allows the coating process to happen in very low temperature (usually $<300^{\circ}\text{C}$). Figure 2.3 shows a schematic of radial-flow plasma enhanced CVD reactor.

The coating process in the present research is reactive sputtering deposition, which is a combination of physical vapor deposition (PVD) from the sputtered metal flux and chemical vapor deposition (CVD) from the hydrocarbon ions and radicals in the gas phase [Feng, 2001]. In the deposition device system, inductively coupled plasma devices (ICP) and magnetron sputter deposition devices are used to enable a wide range of metal concentrations in the coatings.

2.2 Coating Procedure and Equipment

The deposition system used in the Ti-C:H coating of present research is an inductively

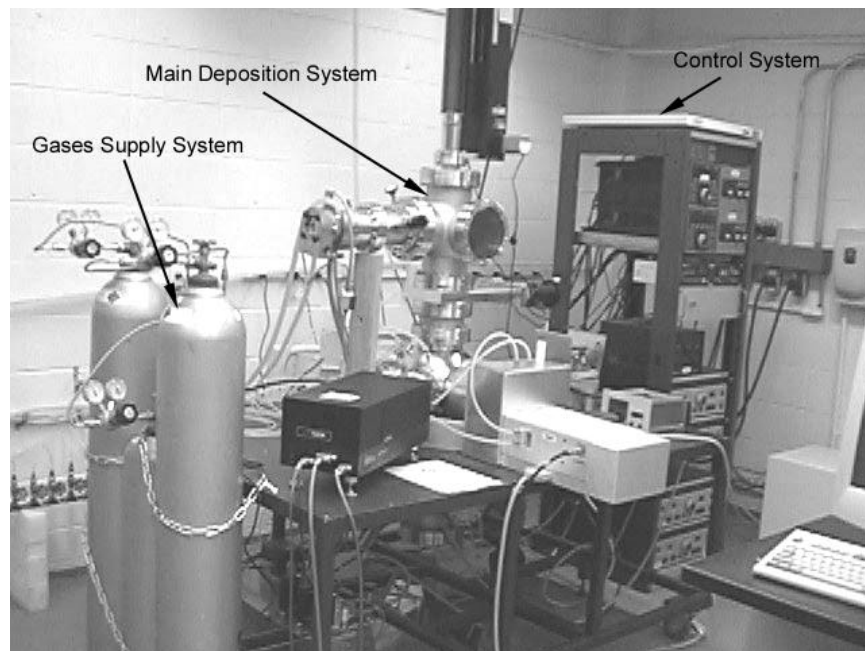


Figure 2.4 Deposition system used in present research

coupled plasma (ICP) assisted hybrid chemical vapor deposition (CVD)/physical

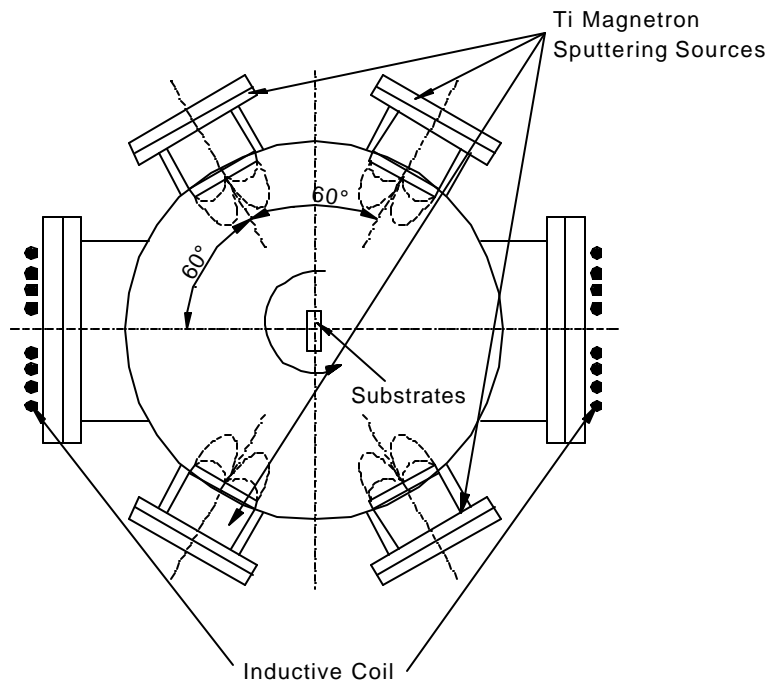


Figure 2.5 Deposition chamber layout [Feng, 2001]

deposition (PVD) tool, which is a combination of radio frequency (RF) ICP and balanced magnetron sputter sources. The ion energy, the flux to the substrate and plasma density can be independently controlled in the system. Figure 2.4 shows the overall image and general layout of the system. The whole system can be roughly separated into three systems: gases supply system, main deposition system and electric control system. The gases supply system stores Argon gas (Ar), acetylene gas (C_2H_2) and Nitride (N_2) which is not used in this experiment. When gases are needed, they are supplied through different gas pipes and controlled by MKS Mass-Flo gauges. The main deposition system is connected with two pump lines: the turbo molecular pump backed by a rotary vane pump is for pumping nitrogen; the cryogenic pump is used for Argon pumping. It is separated into two parts by an airtight gate (load lock). When loading samples, the gate is

closed to ensure high vacuum in the deposition chamber and quick recovering of the whole system. The schematic of deposition chamber layout can be seen in Figure 2.5. Four titanium magnetron-sputtering sources and two plasma induction coils, which are installed in opposite pairs respectively, scattered around the circumference of the chamber with 60° apart. All the above systems are control in the control system.

The coating samples used in this experiment were made of 1020 steel. They were cut into 0.25 in (~6 mm) thick rings from standard $14 \times 10 \times 2$ steel tube (O.D 14mm, I.D. 10mm) and were grinded on both sides to make them parallel to each other within 0.002 in (~0.05 mm). Then one side of the sample rings were polished to reach $Ra < 1 \mu\text{m}$. After that, the samples were cleaned in acetone and methanol with ultrasonic cleaner to get rid of the oil/grease and dirt. When necessary cleanness was reached, the samples were fixed in a special sample holder shown in Figure 2.6 and loaded into the deposition chamber.

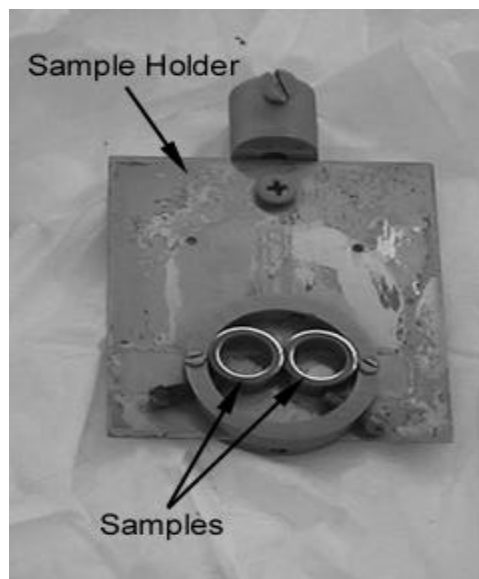


Figure 2.6 The sample holder

The deposition process could be started when the chamber pressure dropped to $<5 \times 10^{-8}$ torr. First, the substrates were argon ion etched for 10 minutes to obtain a cleaner surface. Then, a layer of Ti was deposited on the substrate surface for 10 minutes. This could increase the adhesion of Ti-C:H coating with the substrate in the following steps. The actual Ti-C:H coating process was carried out in Ar/ C₂H₂ gases mixture right after the Ti interlayer coating. By fixing Ar flow, C₂H₂ flow, sample bias and ICP power and changing Ti gun current, a series of eight groups of specimens were made, which correspond to eight different Ti volume fractions in the coatings. Table 2.1(a) and 2.1(b) shows the parameters for different coating steps.

Table 2.1(a) Parameters for different steps in Ti-C:H coating

Procedure	Ar flow (sccm)*	C₂H₂ flow (sccm)*	Sample bias (V)	ICP Power (W)	Ti gun current (Amp)	Duration (min)
Ion Etching	50	0	-100	1000	0	5
Interlayer Deposition	50	0	-50	1000	0.2	15
Coating Deposition	50	5	-50	1000	See Table 2.1(b)	25

Table 2.1(b) Ti gun current for coating samples

Specimen ID	Ti Gun Current (Amp)
W11401	0.2
W11501	0.4
W11601	0.6
W11701	0.8
W11901	1.0
W12001	1.2
W11001	1.4
W12201	1.6

* sccm : cubic centimeter per minute

CHAPTER 3 TRIBOLOGICAL TESTS OF Ti-C:H COATED RING ON DISK

3.1 Mechanical and Tribological Properties of Coatings

To characterize the performance of a coating, its mechanical and tribological properties should be evaluated. Mechanical properties of coatings include hardness, bending strength, Young's modulus of elasticity, adhesion of the coating to the substrate and fracture toughness. Coating's tribological properties refer to its friction and wear characteristics. Wear characteristics include adhesive, abrasive, erosive, and fatigue wear.

Many testing techniques can be used to evaluate the mechanical and tribological properties of coatings. Hardness and elastic modulus can be measured by means of a nanoindentation testing apparatus. With this test instrument, an indenter is pressed normally to the coated surface and the load and displacement are monitored continuously. The hardness and modulus of elasticity can be calculated from the projected contact area and corresponding load.

Four-point-bending test is often used to estimate the bending strength of a coating. The test sample is a rectangular beam and the coating is on the surface subject to the maximum tensile stress. In a four point bending test, the sample is simply supported at the either ends and two loads are placed symmetrically over the center span. The load is increased until fracture is observed. The bending strength can then be estimated as [Jones and Berard, 1972]:

$$s_{bend} = \frac{3P_f(L-a)}{2bd^2} \quad (3.1)$$

where P_f is the load when fracture occurs, L and a are beam span and distant between two inner loads, respectively, the parameters b and d are width and depth of the beam, respectively.

The adhesion force between coating and substrate arises from the intermolecular interaction between two materials. It must be high enough to sustain the shear from friction force and the residual stresses from the coating process. Many methods are implemented to estimate the adhesion strength of a coating. They include tension, shear, peel scratch indentation, ultrasonic, blister, electron beam and pulsed laser. Of all the testing methods, indentation test, scratch test and pull test are more commonly used [Bunshah, 1982]. The indentation test is similar to that for hardness and elastic modulus. The normal load and the average size of the area around the indentation from which the film has peeled are recorded and plotted. By observing the plot of the load versus the indentation area, the adhesion strength can be obtained. The scratch test uses a diamond indenter to plow the coating over a straight distance under certain load. The depth of the scratch produced in this fashion is then measured and the load under which the coating is peeled from the substrate is estimated. The pull test is carried out by bonding a stud on the coating with epoxy glue and then pulling the stud. The load at which the failure takes place is measured. If the failure takes place at the bonding between the coating and substrate and nowhere else, the adhesion strength can be estimated [Bunshah, 1982].

Friction coefficient and wear are key parameters in tribological tests. They can be measured in sliding tests, usually by fixing one body and sliding another body on it. Typical sliding tests geometries are shown in Figure 3.1. Among these geometries, pin-on-disk test (or ball-on-disk) (Figure 3.1a) and thrust washers test (or ring-on-disk test)

are often used for coating material evaluation. In current research, a ring-on-disk test configuration is used in a universal tribometer for all the experiments.

The coefficient of friction f can be calculated from the ratio of friction force F to the applied normal load N ratio as in equation 3.2 below.

$$f = \frac{F}{N} \quad (3.2)$$

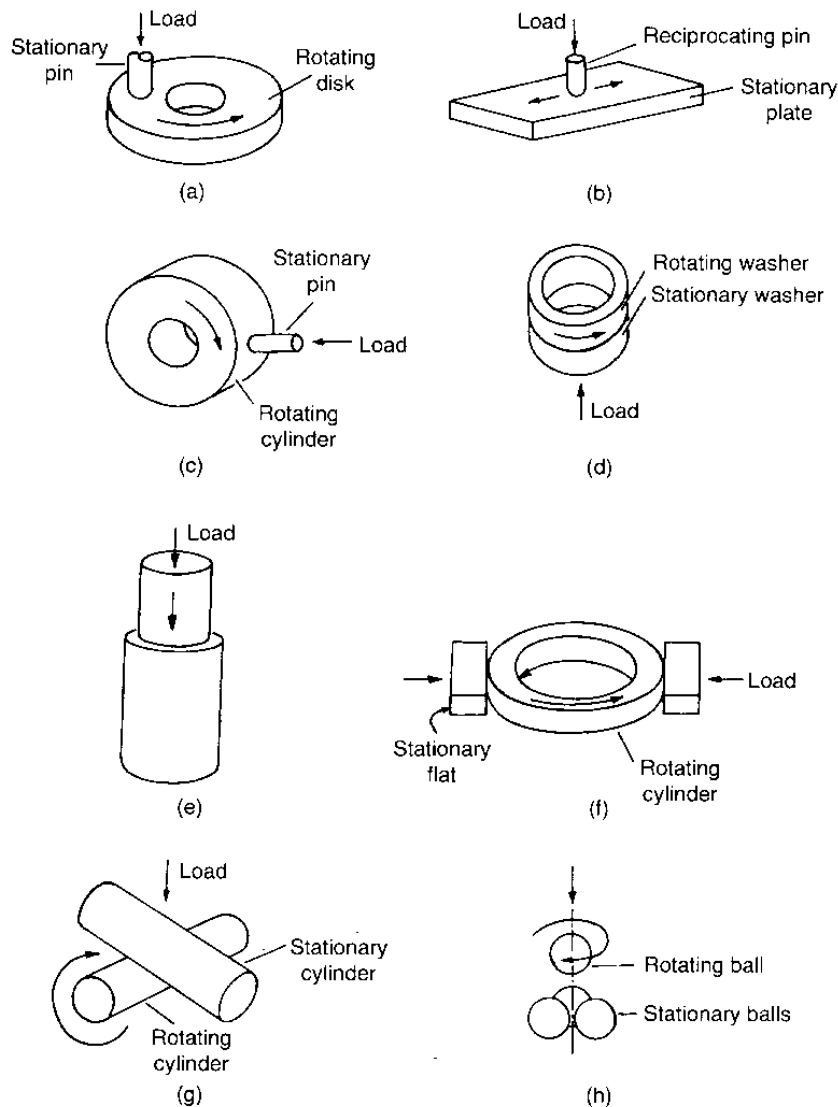


Figure 3.1 Typical sliding tests geometries [Bhushan, 1999]

The friction force is measured by means of strain gages, displacement gages or piezoelectric force transducer. The constant applied load can be achieved by using a dead weight or close loop control system.

Wear can be obtained from many techniques such as weight loss, volume loss or wear scar width or depth. Scanning electron microscope (SEM) and scanning tunneling microscope (STM)/atomic force microscope (AFM) are often used for determining the geometry of the worn surfaces. All these methods have their own advantages and disadvantages. Table 3.1 shows the resolution of some of the commonly used wear measurement techniques [Bhushan, 1999]. In the present research, both weight loss and stylus profiler are used for the wear measurement.

Table 3.1 Resolutions of several wear measurement techniques [Bhushan, 1999]

Measurement Technique	Resolution
Weight loss	10-100 μ g
Radioactive decay	\sim 1 pg
Stylus and optical profilers	0.5-10 nm
Microhardness indentation	25-50 nm
Nanoscratch technique	1-10 nm
SEM	0.1 nm
STM/ATM	0.05-0.1 nm

Wear performance of a coating material is often represented by the wear coefficient k , which can be calculated from Archard's equation (equation 1.2). Sometimes, instead of calculating the wear coefficient, a wear rate is calculated to evaluate the film's wear performance. Wear rate can be calculated in different fashions depending on the specific experimental setup and analysis requirement. The common wear rate calculation methods are: 1) the volume of material loss per unit distance of sliding, 2) the volume of material loss per unit period of time, 3) the volume of material loss per unit distant of sliding per unit normal load. In this research, we use method 3, which is shown in equation 3.3.

$$r_w = \frac{\Delta v}{PVt} \quad (3.3)$$

Where r_w represents wear rate, Δv is the volume loss, P , V and t are normal load, sliding speed and sliding time, respectively. Here $V.t$ represents the total sliding distant.

3.2 Testing Equipment and Procedure



Figure 3.2 Micro tribometer

The experimental tests were carried out using a commercial Micro Tribometer manufactured by CERT. This apparatus enables testing material's tribological properties such as the friction force and coefficient of friction. Figure 3.2 shows the image of the tribometer. It consists of a base system, several load or driving blocks and a computer control system. The base system includes a heavy cast iron frame to avoid vibration and a set of vertical and lateral positioning system. Position encoders are installed on the positioning motors so that the location of the upper cartridge can be precisely controlled and detected. A 6-axis torque/force sensors system is mounted on the upper cartridge

enables the tribometer to measure torques and forces in x , y and z axis. All control data and sensors signal data are manipulated in a PC and interfaced with special software.

Figure 3.3 shows the test setup. A ring with coating is fixed on the upper cartridge of the tribometer. A metal disk (1040 steel in this case) is positioned on the lower testing platform and is allowed to spin with respect to the ring axis. Normal load is added on the ring and passed to the contacting surface by means of a screw system.

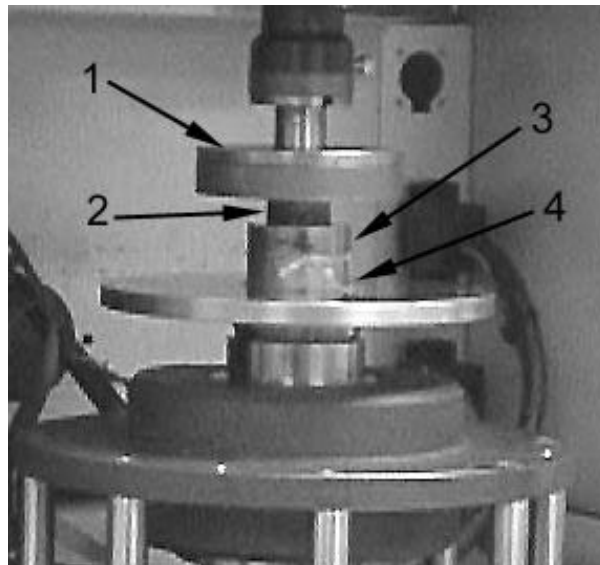


Figure 3.3 The experiment setup (1) sample adapter (2) upper test sample (ring with coating, stationary) (3) lower test sample (disk without coating) (4) lower testing platform (rotating body)

Two sets of experiments were carried out in the tribometer with different duration, various combinations of load and speed (PV). All tests were made in room temperature ($75 \pm 5^\circ F$) in air; the relative humidity was $55 \pm 5\%$. The experimental procedure is described below:

- 1) The test samples including a set of rings and disks were thoroughly cleaned using methanol and stored in clean petri dishes to prevent them from dust contamination.

- 2) The machine is switched on and the control software is open.
- 3) The ring is placed on the sample loader and installed along with the upper suspension onto the upper cartridge.
- 4) The sample disk is fixed to the lower rotating platform with double-sided scotch type.
- 5) All the screws are fastened tightly and button in the control software is pressed to start the test sequence.

The test is made to run with a constant rate of rotation and a constant vertical load. When the specified time is reached, the upper cartridge moves up and the driving motor for lower platform stops within 60 seconds. All the data, which include friction force F_x , F_y , F_z in x , y , z direction and friction torque T_x , T_y , T_z in x , y , z direction, are written to a data file and saved in the computer hard drive for later use. The coefficient of friction is then calculated from T_z .

Before and after each test, both the sample ring and disk were weighed using an electrical scale, which has a resolution of 0.0001 gram. Although the scale is not precise enough for the wear test, it is a good reference to estimate the weight loss scope. This was used to verify the results of wear estimation obtained using a profilometer described next.

A TENCOR ALFA-STEP surface profiler was used for measuring the wear grooves in the disks with horizontal resolution $2\mu\text{m}$ and vertical resolution $1\mu\text{m}$. Four different grooves were measured with 90 degree apart for each of the sample and mean groove cross section areas were calculated from the measurement data. Wear rates were then obtained.

3.3 Test Result and Discussion

3.3.1 Long Duration Dry Test

Total of eight experiments representing eight different Ti compositions in the coating materials were carried out using the same test settings shown in Table 3.2. The main purpose of this test was to determine the coating's wear resistant property as a function of the Ti composition of the whole coating structure. The coating structure consist of the coating material, the bond between coating and substrate and the substrate material. In other words, we need to find how long it will take for the coating to wear out. For this purpose, a relatively long duration time was selected for the tests.

Table 3.2 Test settings for long duration dry test

Setting	Value
Rotating Speed (RPM)	100
Normal Load (N)	30
Duration (s)	~7200
Lubrication	No

Figure 3.4(a) – 3.4(h) shows the friction torque in vertical direction T_z during the test and time for test samples with different coatings. Figure 3.4(a) is for the coating that was deposited under Ti cathode current of 0.2 Amp, which corresponds to <10% Ti composition. Figure 3.4(h) is for 1.6Amp Ti cathode current, which corresponds to ~50% Ti composition. Ti compositions of the samples for other figures are in between the above two. The relations between Ti cathode current and atomic fraction of Ti, C and hydrogen composition will be shown later in this chapter.

As can be observed from the figures, except for Figure 3.4(b), there are abrupt increases in friction torques during the tests for all the tests. These torque variations reflect sharp changes in the contact conditions on friction surfaces. Obviously, it is

because of a critical amount of coating film being removed from the substrate. The corresponding time-span from the start of the experiment to the time when the sharp torque-changes occurred was indicative of the period before the coating worn out. These results do not show any obvious trend between the worn out period and Ti composition. Since all torque transition points appeared after 1000 seconds, the friction coefficient calculated from the data before 1000 seconds may represent that between the coating and the disk. If the coatings are worn out, the substrate material of the ring would become involved in the rubbing process and thus the coefficient of friction cannot represent the rubbing between coating and disk. The coefficients of friction corresponding to the data before this torque transition, the weight loss, volume loss and wear rate are listed in Table 3.3.

Note that the test for the sample corresponding to coating current 1.6 Amp was intentionally stopped shortly after the torque magnitude transition occurred. The weight loss was not measured. The purpose of this was to find out what the wear types of the coating would be in an unlubricated situation, as will be described in section 3.3.3.

It should be mentioned that the wear rates obtained here are from both the friction of coatings on disks and that of the ring substrates on disks. At the beginning, the wear was caused by the friction between coating and the disk material. However, with the experiments continuing, the coatings would gradually wear out, the substrate material of rings would join the wear process, and result in most of the wear. Therefore, the wear rates values in Table 3.3 cannot purely represent the effect of the coatings on the disks. However, these results provide us with a reference for checking the correctness of the data in the next experiment because the wear rate values from coatings will be much less than these values.

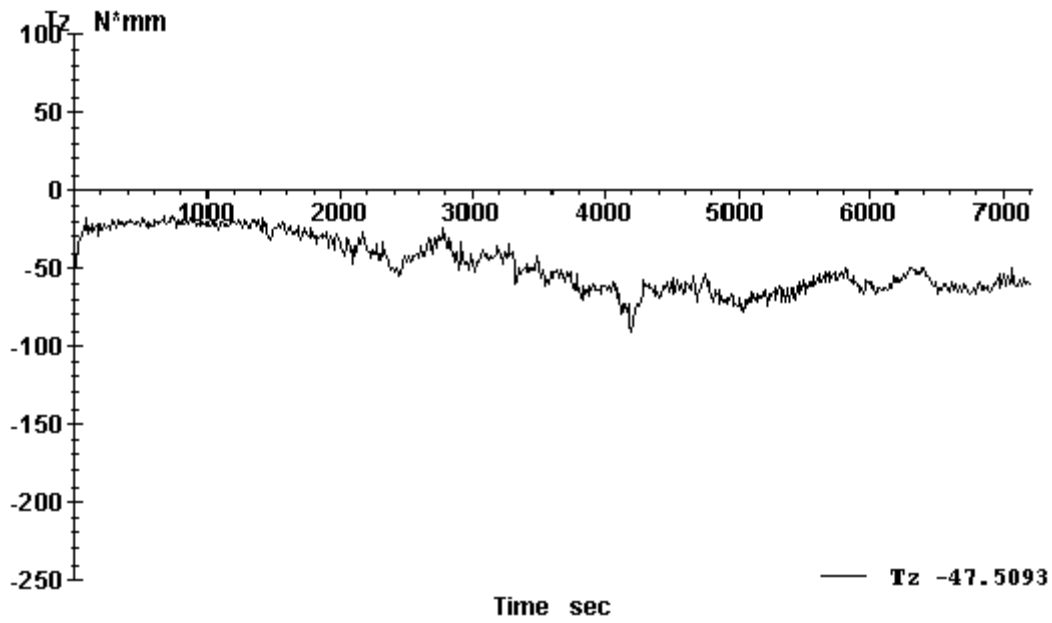


Figure 3.4 (a) Friction torque vs. time for coating produced under 0.2 amp Ti cathode current

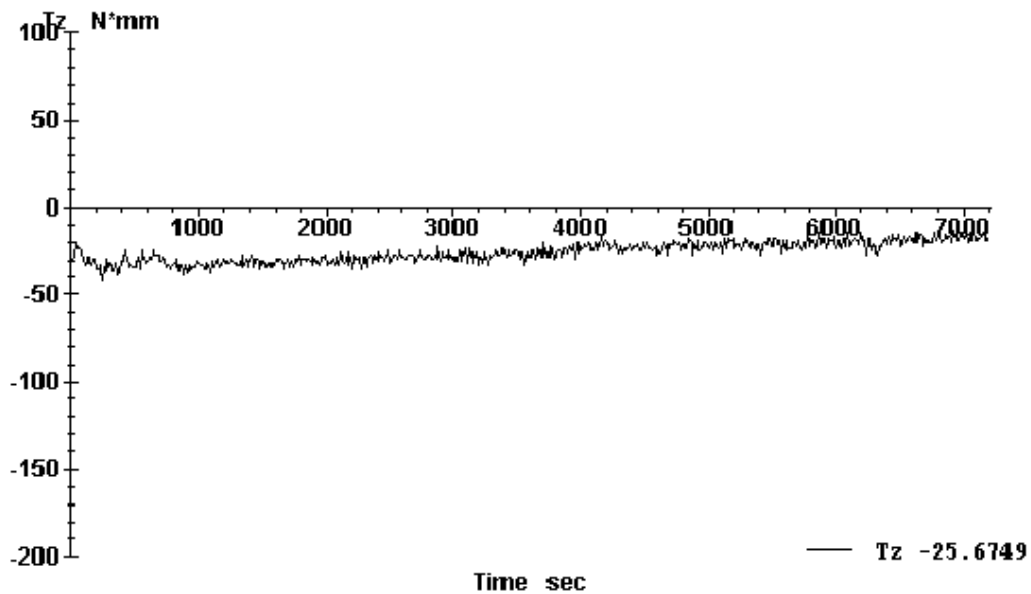


Figure 3.4 (b) friction torque vs. time for coating produced under 0.4 amp Ti cathode current

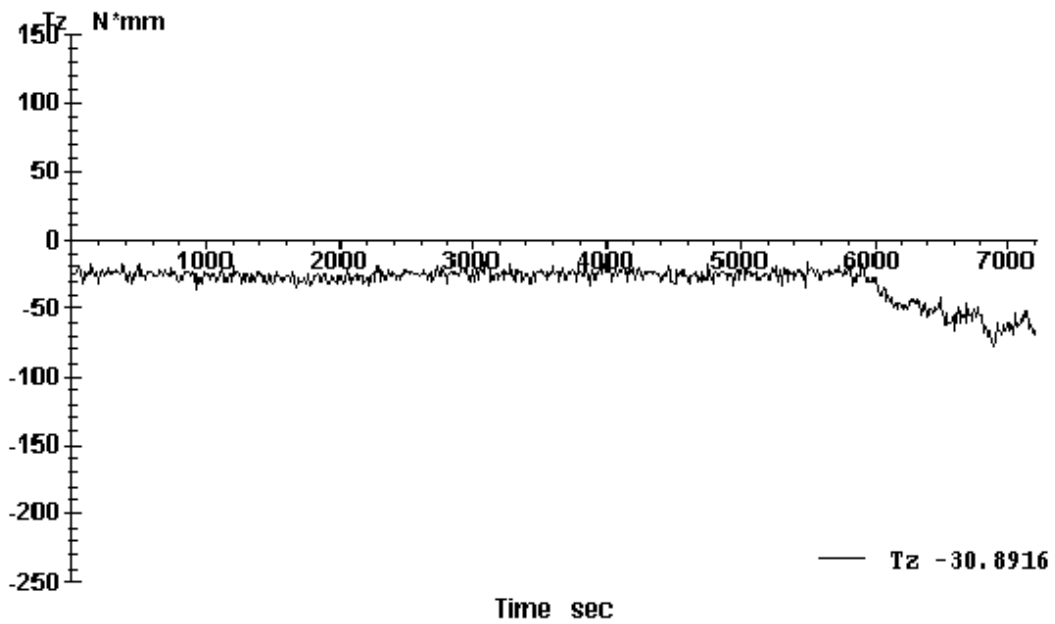


Figure 3.4 (c) Friction torque vs. time for coating produced under 0.6 amp Ti cathode current

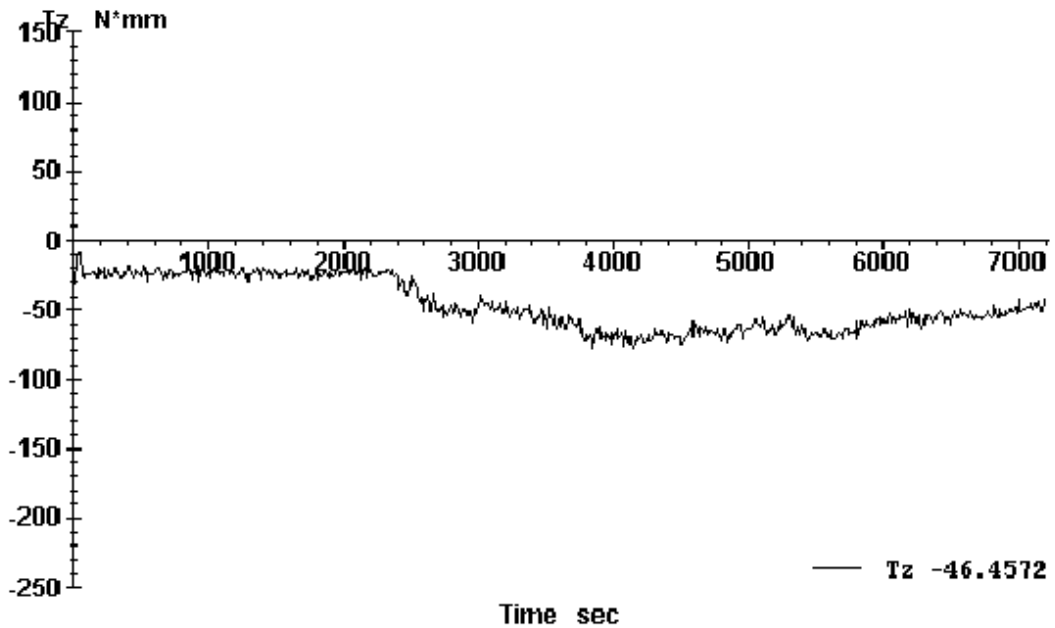


Figure 3.4 (d) Friction torque vs. time for coating produced under 0.8 amp Ti cathode current

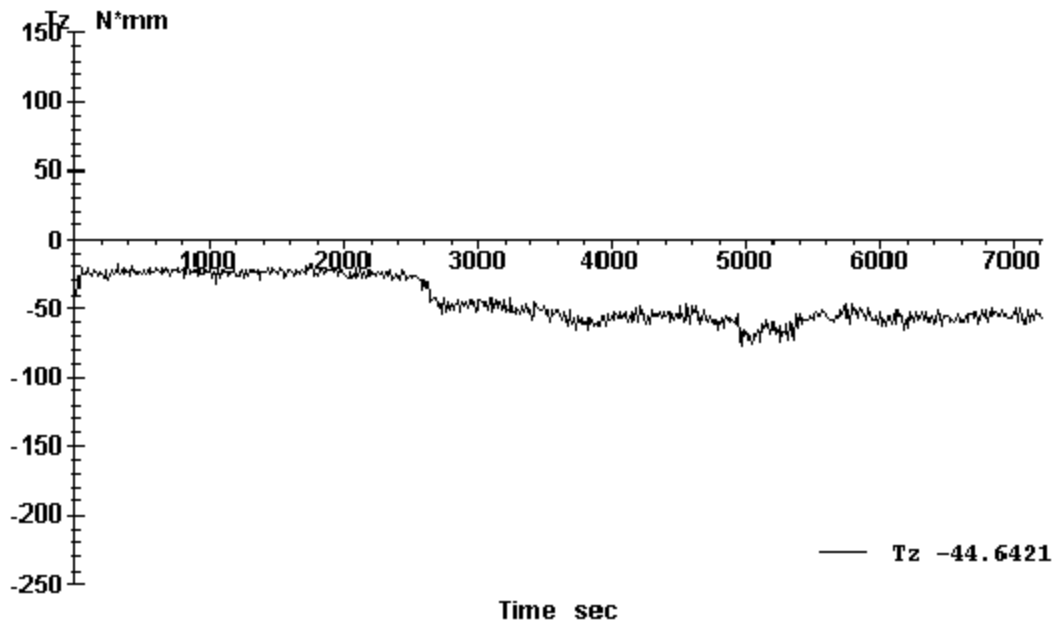


Figure 3.4 (e) Friction torque vs. time for coating produced under 1.0 amp Ti cathode current

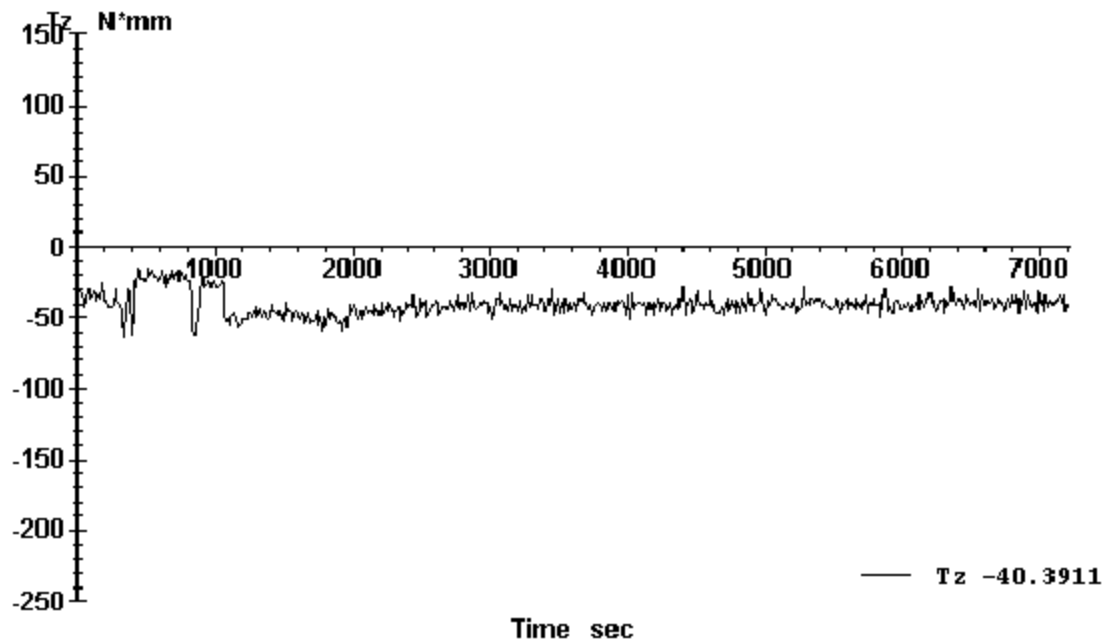


Figure 3.4 (f) Friction torque vs. time for coating produced under 1.2 amp Ti cathode current

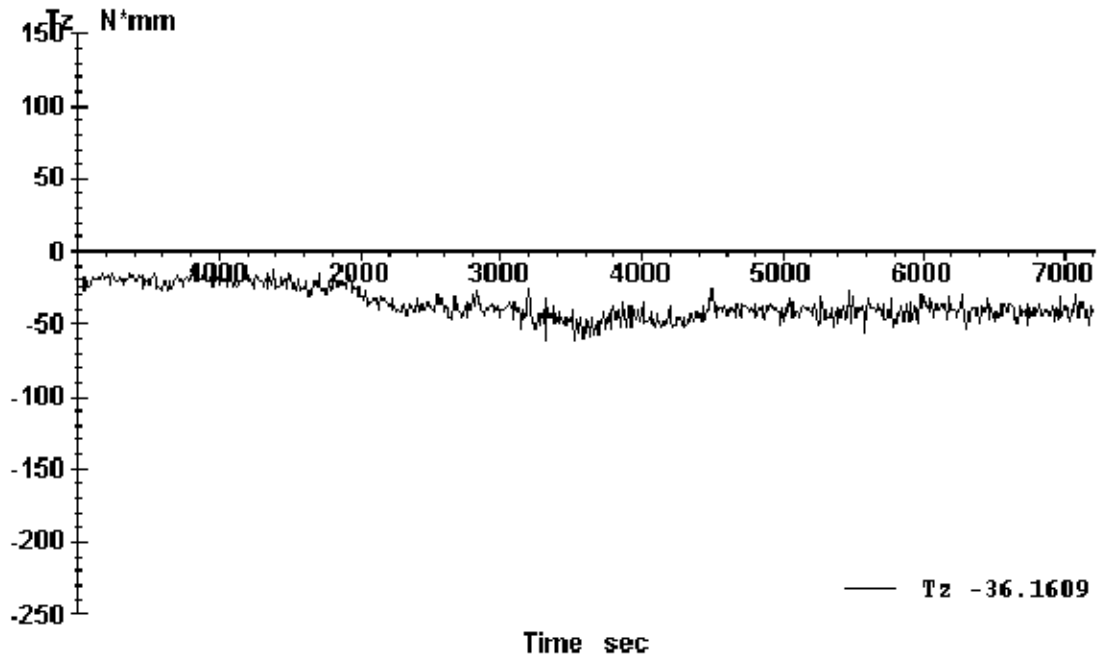


Figure 3.4 (g) Friction torque vs. time for coating produced under 1.4 amp Ti cathode current

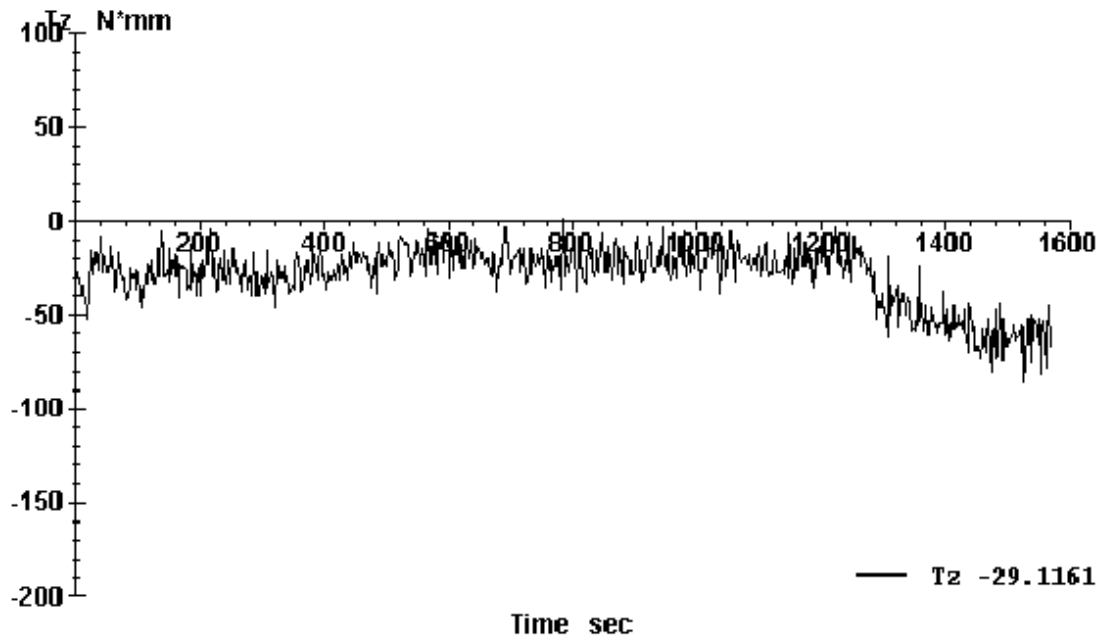


Figure 3.4 (h) Friction torque vs. time for coating produced under 1.6 amp Ti cathode current

Table 3.3 Result of long duration dry tests

Ti Current (Amp)	Coeff. Of Friction Before 1000s	Weight Loss of Sample Disk (g)	Volume loss of Sample Disks From Profiler Data (mm ³)	Wear Rate (mm ³ /Nm)
0.2	0.137	0.0085	5.87261E -1	3.70055E -5
0.4	0.1539	0.0003	1.78344E -2	1.12381E -6
0.6	0.192	0.0025	9.55414E -2	6.02042E -6
0.8	0.168	0.0068	6.76433E -1	4.26246E -5
1.0	0.161	0.0058	6.33121E -1	3.98953E -5
1.2	0.22	0.0042	4.8535E -1	3.05837E -5
1.4	0.163	0.003	2.81529E -1	1.77402E -5
1.6	0.156	N/A	7.26115E -2	2.09084E -5

3.3.2 Short Duration Dry Test

The basic settings and test procedures for the experiments presented in this section are the same as those of long-duration, dry tests except that the testing period was set to 1000 seconds, i.e. the time when the friction was uniform for all coatings in accordance to the findings in the long duration tests. Since the duration of this set of tests is short, the coating will not wear out before the end of the tests, thus the measured wear is thought to be a good representation of the friction from the sample disks material and the coating material. The friction torque and time plots are shown in Figure 3.5 (a) – Figure 3.5 (h).

The coefficient of friction, the weight loss, the volume of the material removed with the corresponding wear rate are listed in Table 3.4.

Table 3.4 Result of short duration dry tests

Ti Current (Amp)	Coeff. Of Friction	Weight Loss of Sample Disk (g)	Volume loss of Sample Disks From Profiler Data (mm ³)	Wear Rate (mm ³ /N.m)
0.2	0.1125	0.0006	4.8069E -3	2.1441E -06
0.4	0.1697	0.0008	1.4455E -2	6.4475E -06
0.6	0.1692	-1E -04	5.06631E -3	2.2598E -06
0.8	0.117	-1E -04	1.83446E -3	8.1824E -07
1.0	0.138	1E -04	3.23691E -3	1.4438E -06
1.2	0.1832	0.0003	1.65728E -2	7.3921E -06
1.4	0.1629	1E -04	1.82707E -2	8.1494E -06
1.6	0.1332	-0.0002	7.48588E -3	3.339E -06

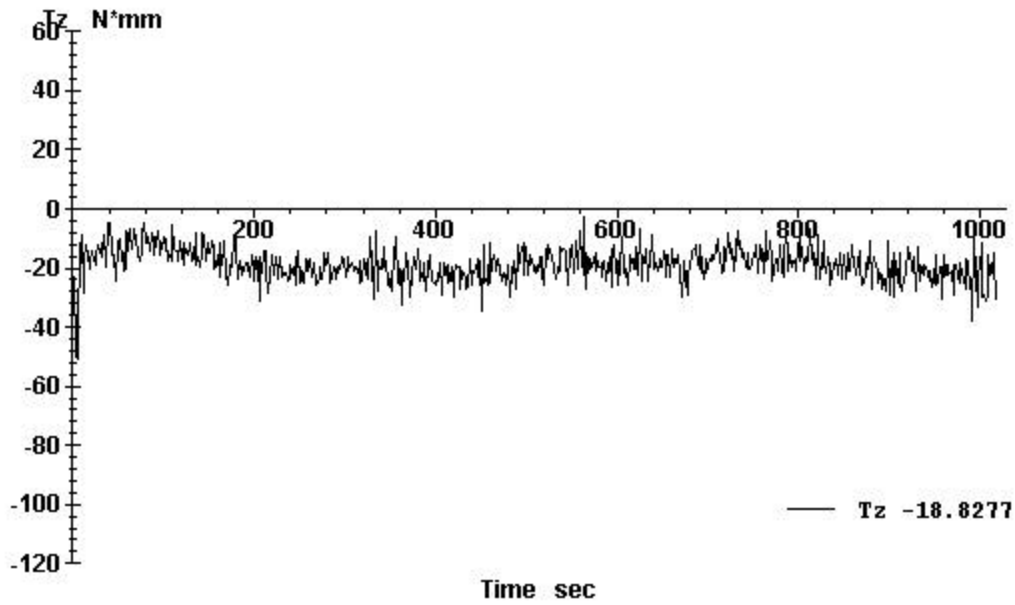


Figure 3.5 (a) Friction torque vs. time for coating produced under 0.2 amp Ti cathode current in short duration test

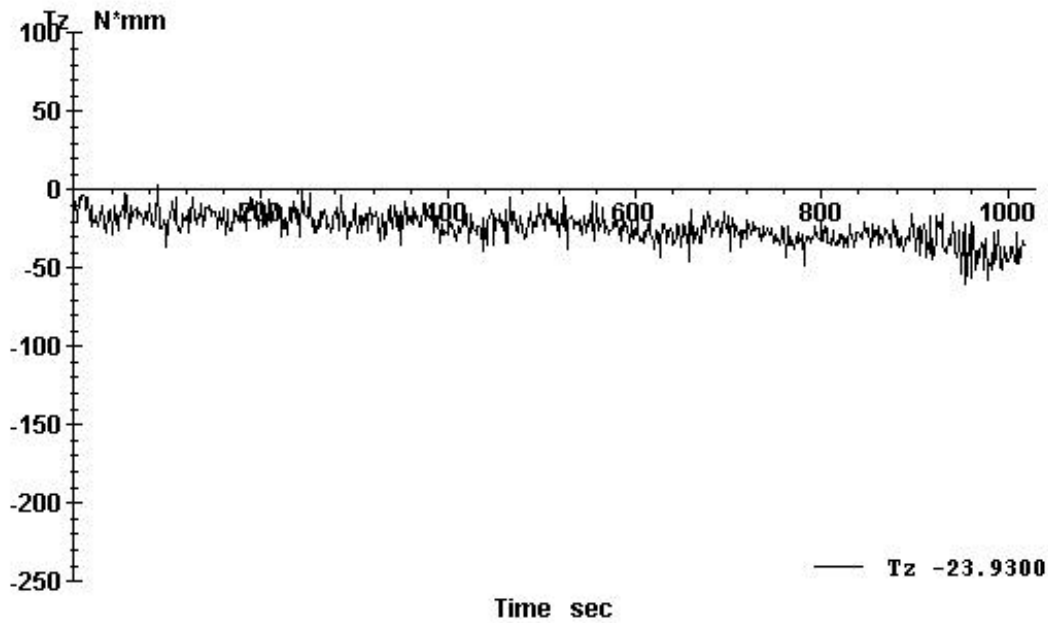


Figure 3.5 (b) Friction torque vs. time for coating produced under 0.4 amp Ti cathode current in short duration test

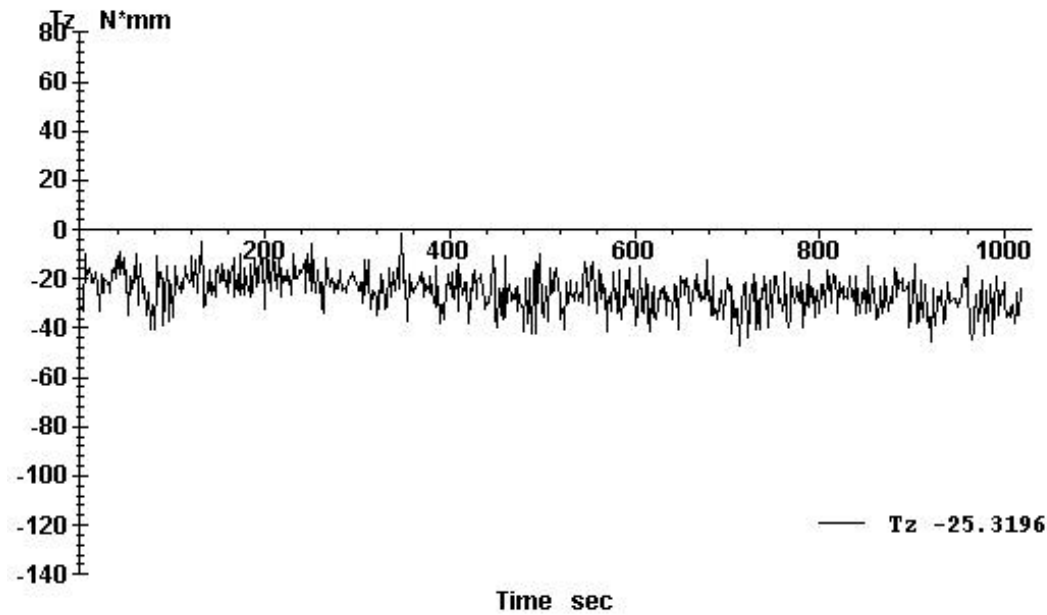


Figure 3.5 (c) Friction torque vs. time for coating produced under 0.6 amp Ti cathode current in short duration test

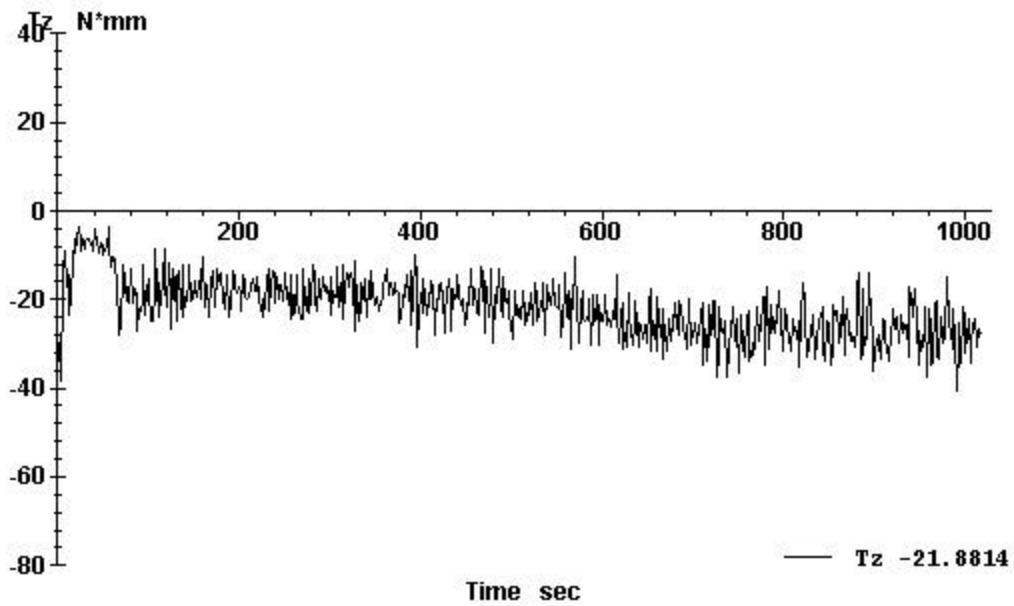


Figure 3.5 (d) Friction torque vs. time for coating produced under 0.8 amp Ti cathode current in short duration test

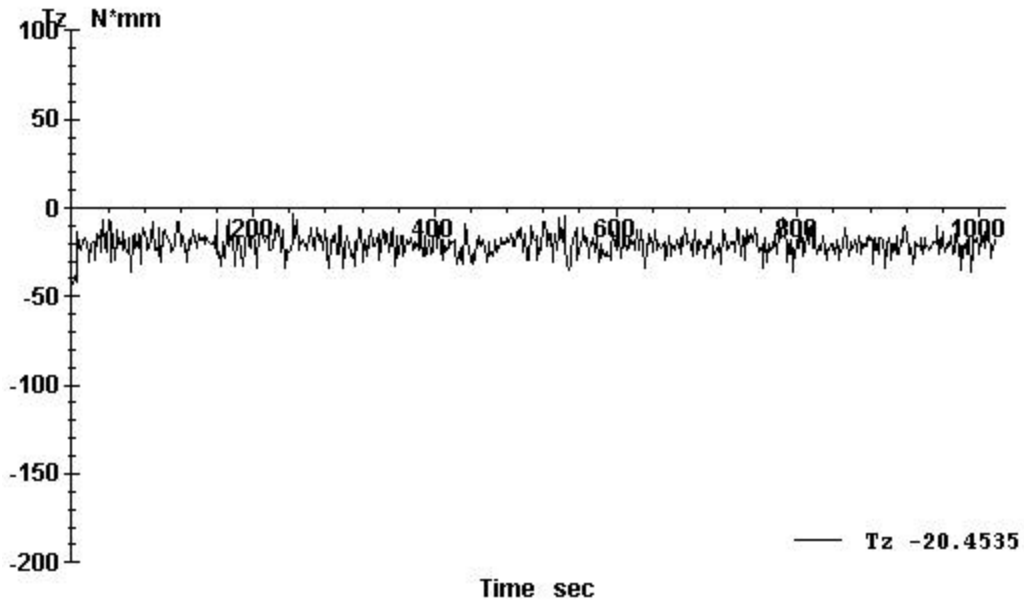


Figure 3.5 (e) Friction torque vs. time for coating produced under 1.0 amp Ti cathode current in short duration test

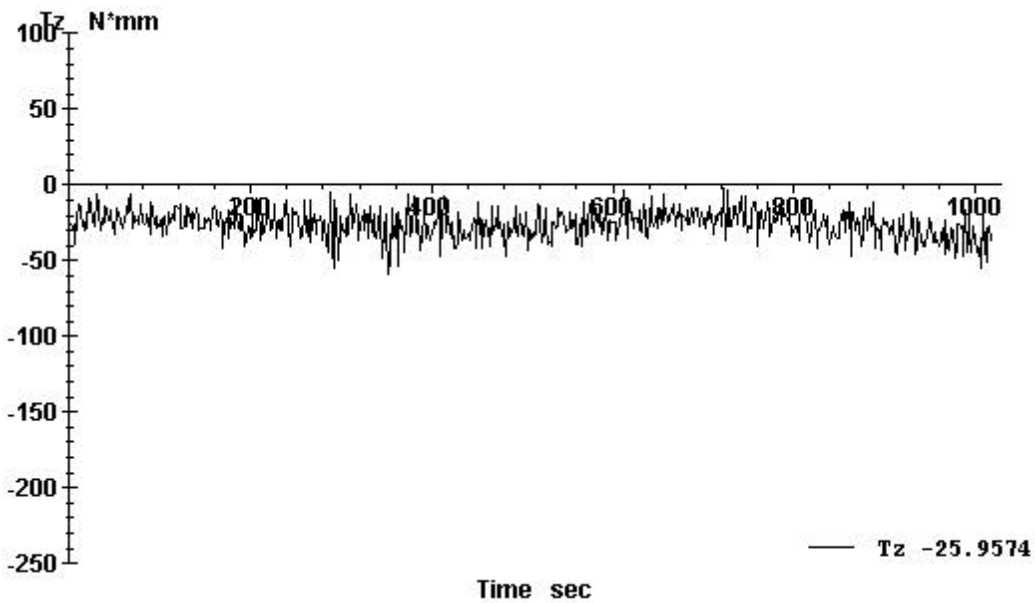


Figure 3.5 (f) Friction torque vs. time for coating produced under 1.2 amp Ti cathode current in short duration test

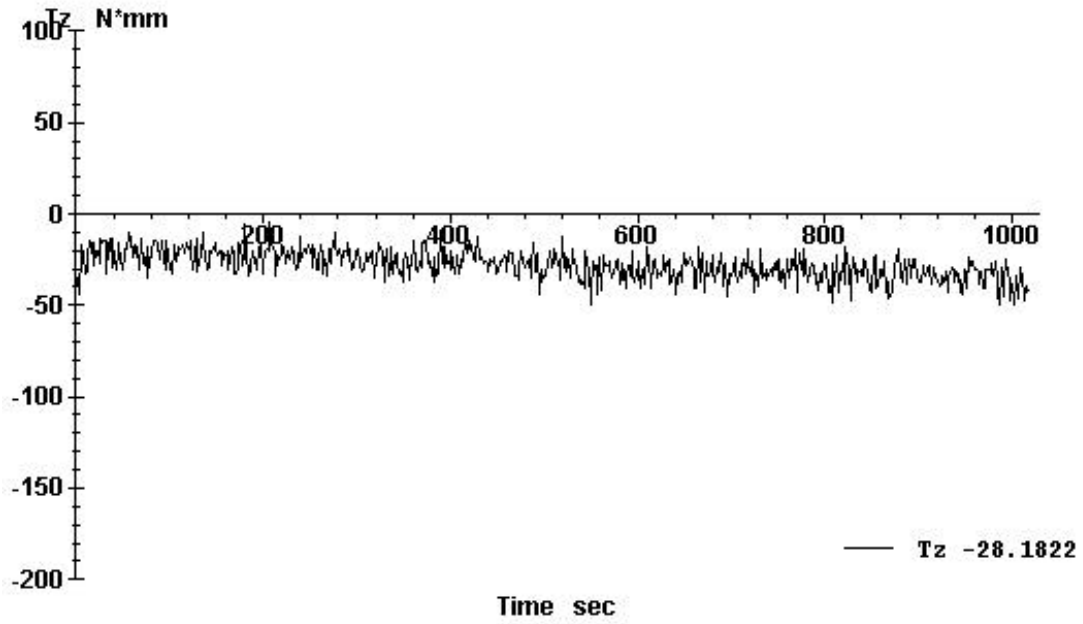


Figure 3.5 (f) Friction torque vs. time for coating produced under 1.4 amp Ti cathode current in short duration test

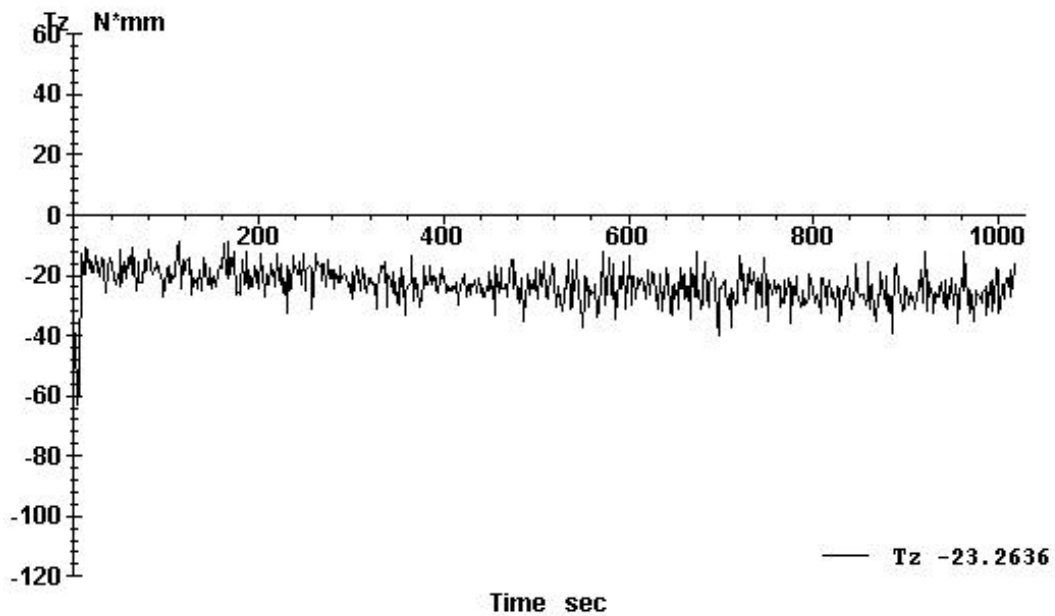


Figure 3.5 (h) Friction torque vs. time for coating produced under 1.6 amp Ti cathode current in short duration test

Since the test duration was short, the wear on the sample disks were very small. The weight loss results shown in Table 3.4 were of the same order of magnitude with the resolution of the equipment (electric scale). This means that the errors in the weight loss results would be very large, thus they cannot reflect the true wear on the disk. On the other hand, since the profiler had higher resolution (0.25 μm in our case), the volume loss results would be convincing. Further discussions of the results are presented in the next section.

3.3.3 Discussion

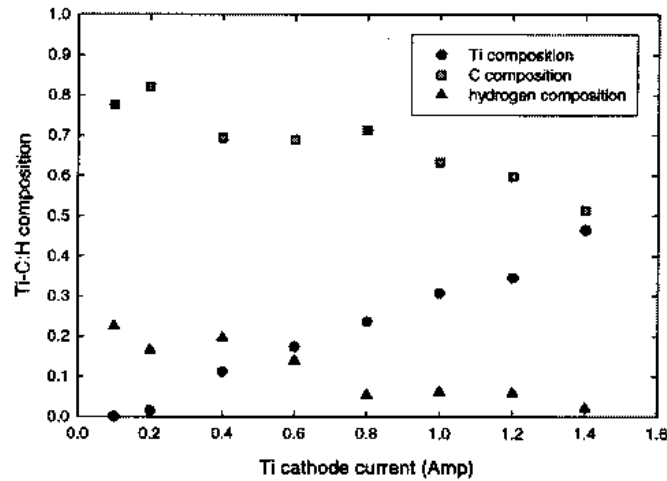


Figure 3.6 Composition of a series of Ti-C:H coatings in atomic fraction as a function of Ti cathode current [Cao, 2001]

In a previous experiment conducted by Cao et al. [Cao, 2001], the relations between Ti-C:H composition for the coating material and Ti cathode current during coating process was found. The relation is shown in Figure 3.6. As the Ti cathode current goes from 0.2 Amp to 1.4 Amp, the Ti atomic fraction increase almost linearly from close to zero to ~50 %. Since the coating equipment and procedures used in the experiments of Cao et al. and in current research are the same, Figure 3.6 can also be used to relate our results to the Ti composition. Cao et al. also carried out a series of ball-on-disk tests, in

which the coatings were deposited on the Si wafers or steel coupons. The coefficient of friction measured in their test was in the range of 0.1 to 0.35. The wear rates of the coatings were in the range of $10^{-7} \sim 10^{-5} \text{ mm}^3/\text{Nm}$.

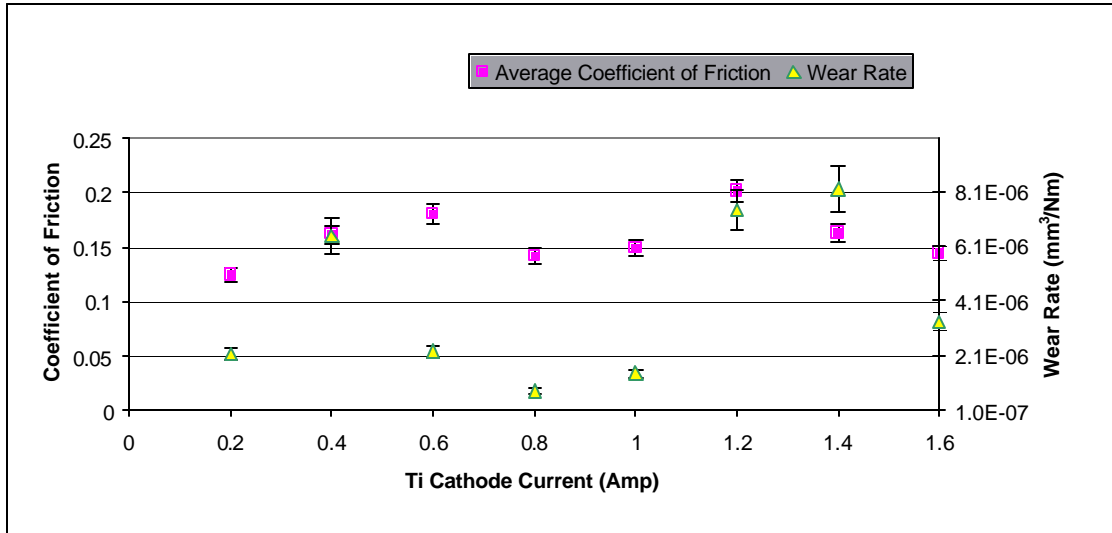


Figure 3.7 Average friction coefficients of the coating materials, wear rate of the mating material vs. Ti cathode current

Figure 3.7 shows the friction coefficient of the coating in the current research, wear rate of the mating disks material and Ti cathode current relationship. The coefficient of friction is the average of those in Table 3.3 and Table 3.4. As can be seen in the figures, the coefficients of friction are in the range of 0.1 to 0.25. It is within the same range with the coefficient of friction that is obtained by Cao et al. [Cao, 2001]. The typical friction coefficient value of mild steel on mild steel in unlubricated condition at room temperature is 0.7~0.8 [Bhushan, 1999]. Compared with the typical value of friction coefficient, the values obtained in the current research indicate that under unlubricated plane-on-plane contact condition (as in our case), Ti-C:H coating can significantly decrease the friction. The wear rates in our experiments are within the range of $1 \times 10^{-7} \sim 1 \times 10^{-5} \text{ mm}^3/\text{Nm}$. This wear rate was obtained from the wear of steel disks. It is not

comparable to the values of Cao et al. because their results pertained to the wear rates of the coating material. But the fact that the two wear rates are of the same order of magnitude indicates that before the coating wears out the difference between the wear in the coatings and those in the mating material (the disks) were small. Comparing the wear rates in short-duration tests with those in long-duration tests, we can find that the former are roughly 1/10 of the latter. This indicates that most of the wears in long-duration test occurred after the coatings wore out and that the coating significantly reduced the wear rate.

As mentioned in the last section, one test (with coating produced under Ti cathode current 1.6 Amp) was intentionally stopped a short time after the sharp friction torque change occurred. A picture of the test piece would present us with its wear state right after the coating begins to wear out. Figure 3.8 shows the magnified wear scars on the coating side of the ring in this experiment. Two kinds of scars can be found in this figure. The large white area in the center indicates that the coating material in this area was peeled off from the substrate. It was supposed to be the result from adhesive wear. The small pits and grooves were supposed to be caused by abrasive wear. The process is thought to be as follows: First, since all surfaces were very clean and smooth, the adhesive wear dominated and some fractions of the coating were peeled off from the substrates. Then as the adhesive wear continues, the debris interacted with the rubbing surfaces causing adhesive wear. As the process continued, more wear debris was created and the surface roughness of both surfaces increased. As a result, the adhesive wear became less important and abrasive wear tended to dominate. Since the wear process started from adhesive wear, the coating's operational life can be enhanced by minimizing the adhesive wear. Further research should be devoted to reducing the adhesive wear.

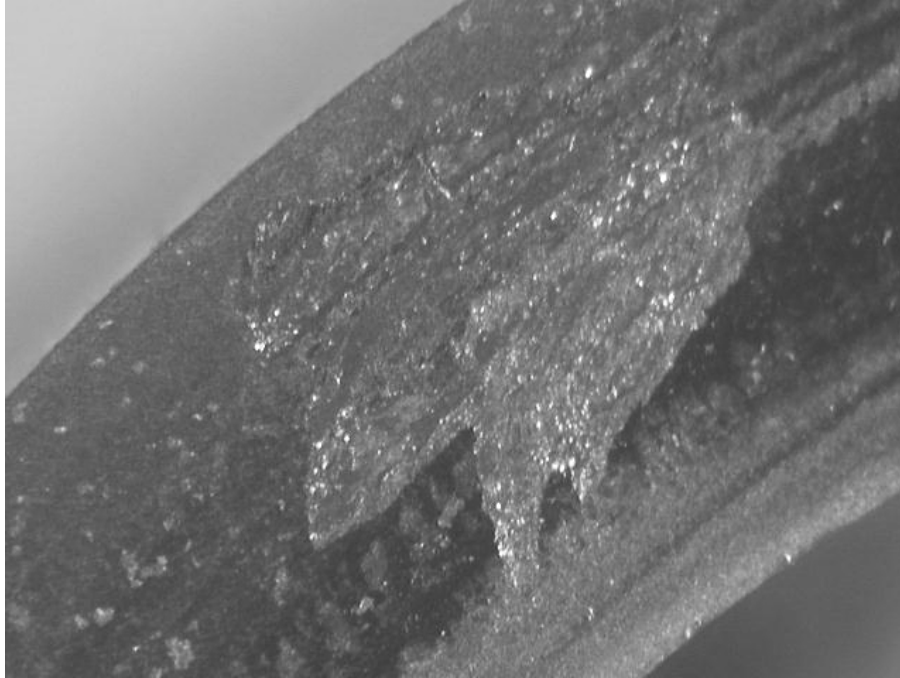


Figure 3.8 Wear scars of the coating produced under 1.6 amp Ti cathode current after 1600s of unlubricated ring-on-disk test

CHAPTER 4 MANUFACTURING OF MICRO HEAT EXCHANGER

4.1 Purpose

Implanting an array of tall micro posts ($\sim 500\ \mu\text{m}$) beneath the surface of a mechanical seal can enhance the performance of a seal. When cooling fluid paths are arranged properly, the posts can act like small pin fins, which will remove large amount of heat from seal faces by way of heat conduction/convection. The advantages of the seals with micro posts structure are as follows [Kountouris, 1999]:

- a. Because the cooling effect occurs inside seal's ring, the effective cooling area is increased. A micro heat exchanger so designed directly extracts heat generating at the surface. This provides a significantly greater heat transfer mechanism than in conventional seals where only the outside surface of the seal ring is cooled.
- b. Since a substantial amount of heat is carried away by the implanted microstructure rather than the seal's outside surface, more heat flows axially. Therefore, the radial thermal gradients near the seal surface are reduced. Thus, distortion and thermal stress from thermal gradients are minimized.
- c. The heat removed by the microstructure is independent of the seal's operating speed and is only a function of the PV value. Therefore, many combinations of pressure P and velocity V values can be implemented without adversely affecting the seal's thermal field.
- d. The seal ring with the micro posts will be used as the stationary seal ring. More heat removal from the stationary seal means higher thermal conductivity, which is a favorable property for a seal.

A seal prototype with the above mentioned micro posts was built successfully by Kountouris (1999). Tribological experiments on the prototype have proved its potential [Kountouris, 1999].

Structurally, since the solid material is replaced by hundreds to thousands of posts, it is expected that the mechanical strength of the seal ring will decrease. Research is needed to predict the structural integrity of the seal, in the event of a malfunction such as interruption in the supply of lubricant, sudden changes of the shaft speed or local damage by particulate contamination. Thus, a structural failure prediction methodology is needed. In addition, although the experimental results showed good improvement in seal's heat transfer properties when micro posts were implemented, it did not reveal much detail of the prototype's thermal characteristics. Therefore, a comprehensive thermal analysis is necessary to gain further insight into the overall thermal aspects of these seals. The next chapter is devoted to exploring the heat transfer and structural integrity of seal with micro heat exchanger.

The implementation of microstructures on seals is a new branch of research, and more work have to be done to further explore its promising properties and overcome and potential problems that may arise.

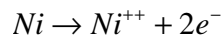
4.2 LIGA and Electroplating

The technique used in fabricating micro heat exchanger is LIGA, which comes from German words X-ray lithographie, galvanofomug and abformtechnik. Strictly speaking, only a part of the LIGA process is used. As its name indicated, the process includes three steps: X-ray lithography, electrodeposition and molding [Madou, 1997]. It was developed for the mass production of structures hundreds of micrometers in dimension in a quick

and inexpensive way. The technique enables the manufacturing of high aspect ratio product, which is a property needed in the fabrication of micro heat exchanger in the current research.

The detailed steps of LIGA are shown in Figure 4.1. First, an X-ray mask is built with the necessary thickness of an absorber, which are metals such as gold, tungsten, and tantalum. Then, a sheet of resist is prepared and attached to a conductive substrate. Poly(methyl-methacrylate) (PMMA) is often selected as the resist for its high sensitivity to X-ray, good process stability and excellent contrast. The PMMA laminate is then aligned behind the mask and exposed to synchrotron radiation. After exposing to enough radiation doses (3 kJ/cm^3 in our case), it is immersed in a developer, which is a chemical solution and can dissolve the exposed PMMA in a selective way producing the pattern desired. After development, the PMMA is rinsed in deionized water and dried in vacuum.

The next step is electroplating. In this step, the PMMA sheet with conductive substrate and the metal to be deposited are arranged in an aqueous solution to form an electroplating cell. An electric circuit is formed by adding DC current on the cathode (the conductive substrate attached on the PMMA sheet) and anode (metal to be dissolved and deposited). Nickel is a typical choice for use as a deposition material. At the beginning of the process, on the anode, a nickel atom loses two electrons to become nickel ion.



On the cathode, nickel ion receives two electrons to change back to nickel atom and be deposited on the cathode. Nickel ions are primarily supplied from Nickel salt dissolved in water and are replenished by the reaction on the anode. At the same time, hydrogen evolution reaction occurs on the same cathode.

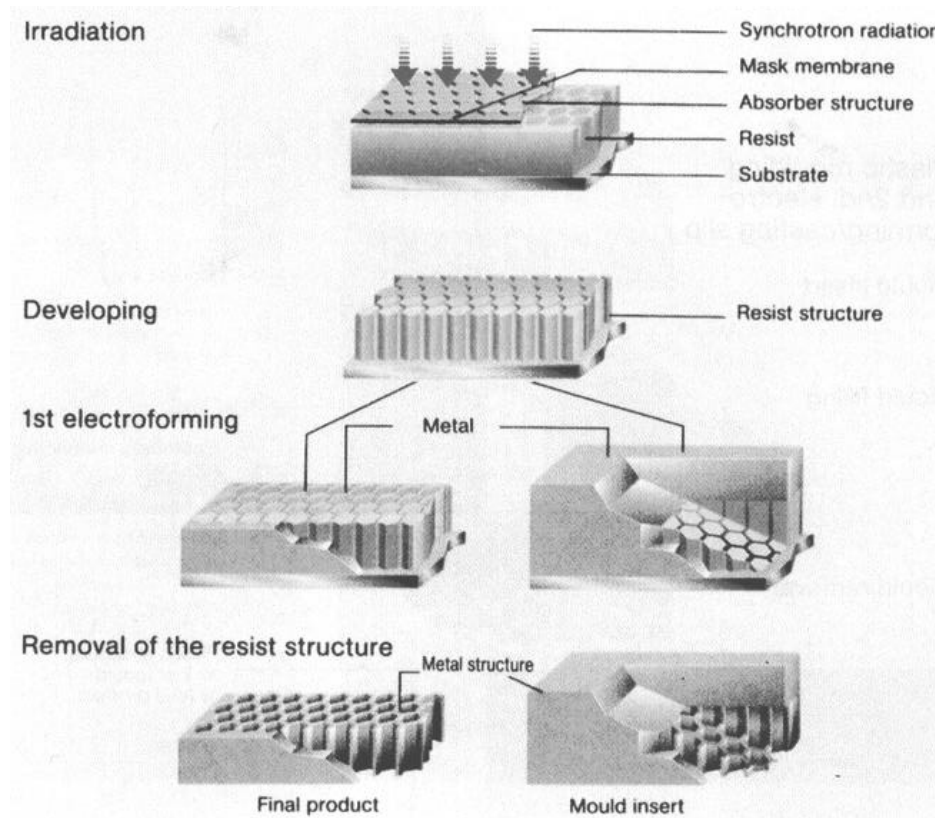
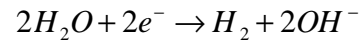
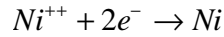


Figure 4.1 Typical LIGA process [Madou, 1997]

The reactions will continue as long as there is electric current. The nickel atoms will be deposited onto the voids in the PMMA sheet pattern until proposed thickness is reached. After the electric deposition process, the PMMA is removed, leaving the final product or a mold for the mass production process. Since the micro posts implanted seal structures were only prototypes, the quantity needed was small. The fabrication process of the seal prototype will finish here. If, in the future, mass product of these seal structures is necessary, the following steps should be used.

The last steps, as seen in Figure 4.2, involves mould filling, mould removal, secondary electroforming and secondary resist removal. These steps provide the method for mass production. They will dramatically decrease the manufacturing cost of the seal structures.

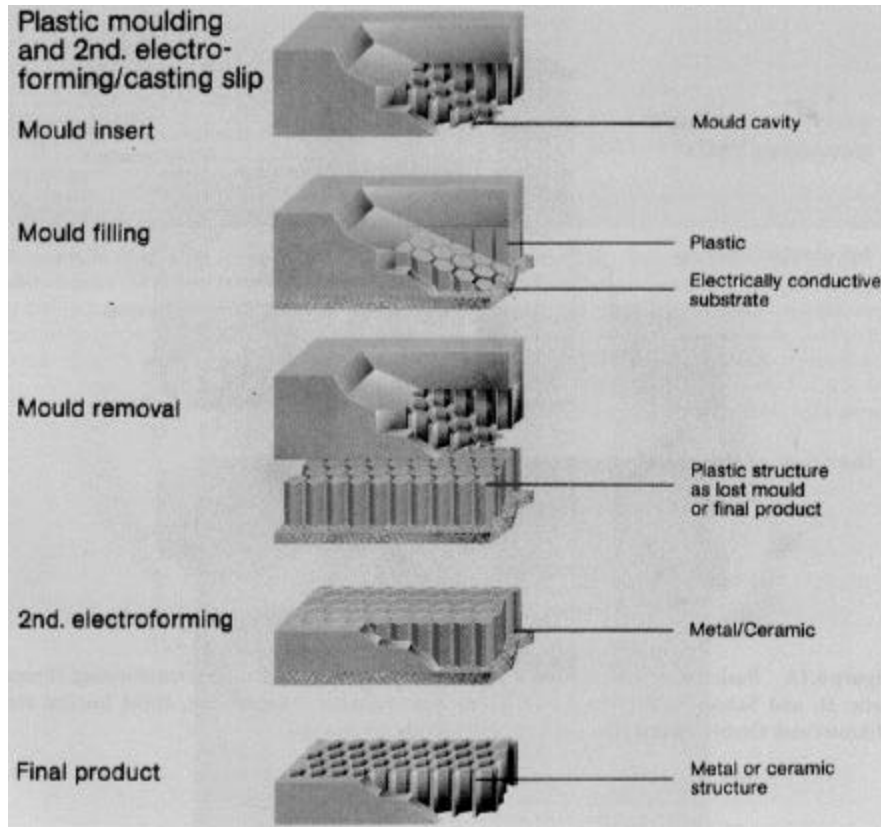


Figure 4.2 Last steps of LIGA process [Madou, 1997]

4.3 Manufacturing Of a Micro posts Implanted Seal Prototype

Two different types of prototypes of seals with micro heat exchanger were constructed by Stephens et al [Stephens, 2001] at the Louisiana State University by means of LIGA. The processes are introduced below [Kountouris, 1999].

4.3.1 Dimensions and Materials

Two versions of seal prototypes with different post density and posts geometry shape were designed by Kountouris for the sake of comparison. Table 4.1 and Table 4.2 show

their design parameters. Besides seal structures themselves, aluminum sleeves and O-rings are built and assembled onto the prototypes to form paths for the cooling fluid.

Figure 4.3 shows the assembly drawing of the seal prototype.

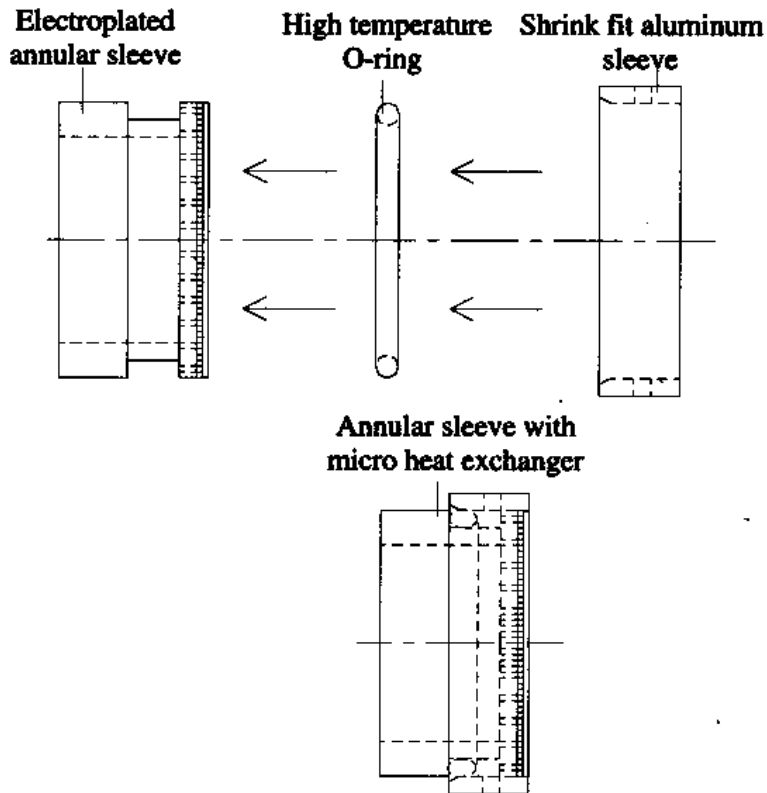


Figure 4.3 Seal prototype assembly drawing [Kountouris, 1999]

4.3.2 LIGA Process

The seal prototypes were built at the Center for Advanced Microstructures and Devices (CAMD) at Louisiana State University. The X-ray masks were first fabricated with square of around patterns by way of UV exposure and electroplating. Gold was chosen as the main absorber. These masks along with proper filters were positioned and aligned with a sheet of 500 micrometers thick PMMA in front of an X-ray beam line for exposure.

Table 4.1 Design parameters of seal prototype (design #1: high post density) [Kountouris, 1999]

Geometry/Property	Value
Aluminum shrink fit sleeve outside diameter (in)	1.065
Micro heat exchanger outside diameter (in)	1.4
Micro heat exchanger inside diameter (in)	1.043
Post height (μm)	500
Post side length (μm)	175
Overplated thickness (μm)	300
Space between posts (μm)	110
Approximate number of posts	5540
Number of holes connecting the annulus to the micro heat exchanger	32
Density of posts (posts/ mm^2)	12.33
Percent filled	37.7
Heat exchanger overplated material	Nickel
Hardness of overplated material (BHN)	500
Substrate material	Stainless Steel

Table 4.2 Design parameters of seal prototype (design #2: low post density) [Kountouris, 1999]

Geometry/Property	Value
Aluminum shrink fit sleeve outside diameter (in)	1.065
Micro heat exchanger outside diameter (in)	1.4
Micro heat exchanger inside diameter (in)	1.043
Post height (μm)	500
Post diameter (μm)	200
Overplated thickness (μm)	1000
Space between posts (μm)	800
Approximate number of posts	440
Number of holes connecting the annulus to the micro heat exchanger	32
Density of posts (posts/ mm^2)	1
Percent filled	3.14
Heat exchanger overplated material	Nickel
Hardness of overplated material (BHN)	500
Substrate material	Stainless Steel

Two criteria were satisfied in order to achieve a successful exposure:

- a. A minimum dose of 3 kJ/cm^3 should be absorbed throughout the thickness of PMMA.

b. Dose at the upper surface of the PMMA sheet should not exceed 20 kJ/cm^3 .

Next, the exposed PMMA sheet is developed and rinsed to form patterns of perforated through holes in them.

The lithographically patterned PMMA sheet from the last step was then fixed onto the surface of the substrate metal by means of a special fixture. Figure 4.4 shows a sketch of the fixture. Two polymer cases were shrink fitted to the inner and outer radii of the substrate to avoid fluid penetrating in the electroplating step, leaving only one end of the substrate exposes to the outside. The patterned PMMA was then clamped by polymer clamps using screws. Then, the whole gadget was immersed in electroplating bath. The void through holes were filled by deposited material. The whole process is controlled so that after all of the voids are filled, the electroplating continues to form an overplate on top of the PMMA sheet to certain height listed in Table 3.1 and Table 3.2.

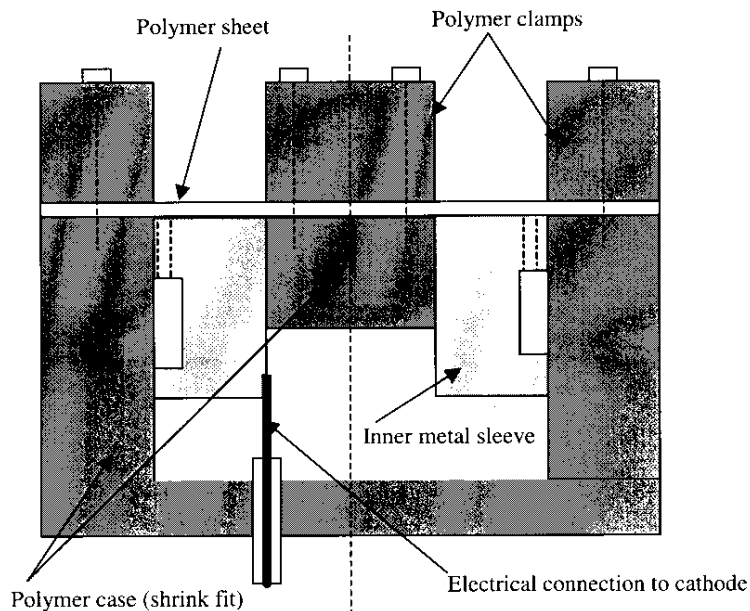


Figure 4.4 Fixture used in electroplating the micro heat exchanger structure [Kountouris, 1999]

When electrodepositing is completed, the structure is disassembled from the fixture and the polymer is dissolved leaving the seal ring with microstructures on.

4.3.3 Seal Assembly

At the same time the seal ring is built, an O-ring and an aluminum sleeve were prepared. The three components were then assembled according to the assembly drawing Figure 4.3 to finish the fabrication.

CHAPTER 5 STRUCTURAL AND THERMAL ANALYSIS OF MICRO HEAT EXCHANGER

5.1 Previous Experiment Introduction

5.1.1 Testing Devices

The wear test on the seal with micro heat exchanger was one of a series of heat transfer and tribology tests completed by Kountouris [Kountouris, 1999]. It aimed at evaluating the effectiveness of the seal structure under the conditions similar to that for a mechanical face seal. As can be seen from Figure 5.1, the tests were carried out in a thrust washer tribometer with add-on measurement devices for temperature, load, wear, moment and speed testing. This tribometer is different from what is mentioned in Chapter II.

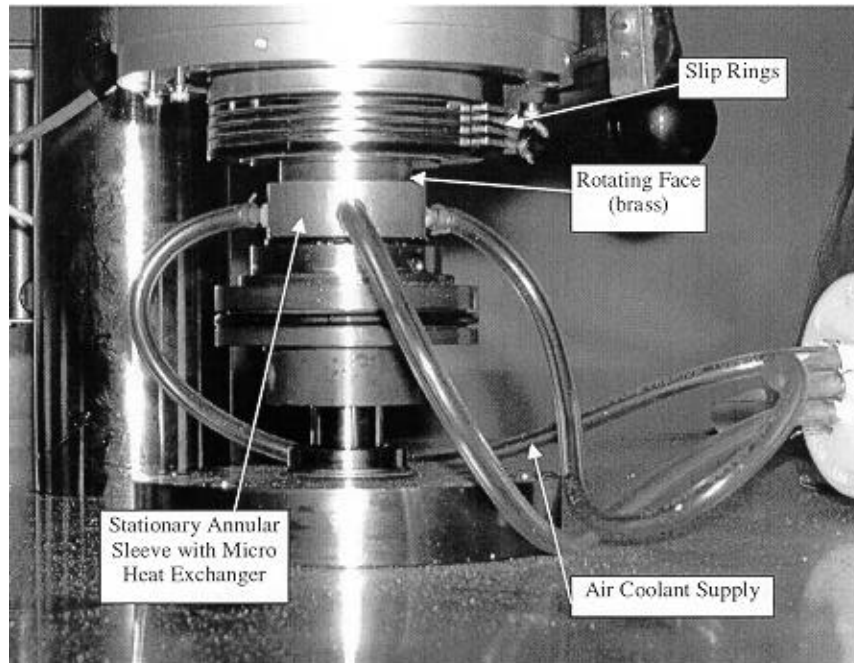


Figure 5.1 Wear test equipment [Kountouris, 1999]

A rotating mating ring is positioned on the rotating shaft through a spring-loaded upper portion of the tribometer. Some properties of the mating ring are shown in Table 5.1. Two small holes were drilled along the mating rings sidewall until their ends were 1 in away from the other end face of the ring. Thermistors were inserted inside these holes to

measure the interface temperature between seal ring and rotating mating ring and were connected to the data acquisition devices through a set of slip rings.

Table 5.1 Properties of rotating mating rings [Kountouris, 1999]

Geometry/Property	Stainless Steel
Outside Diameter (in)	1.375
Outside Diameter (in)	1.07
Height (in)	0.6
Hardness (BHN)	121

The seal prototype was installed on the lower portion of the tribometer and stayed stationary during the tests. Coolant was pumped into the seal structure through holes in the aluminum sleeve. Two kinds of thermocouples were attached on the inside diameter to test the seal ring temperatures of different height. A third kind of thermocouple was placed in front of coolant outlet to test the coolant outlet temperature [Kountouris, 1999].

All the outside surfaces except for the contacting interface for the rotating mating ring and seal prototype inner surface were covered with insulative materials.

All the signals from thermocouples/thermistors, load, speed, torque and distant sensors were sent to an A/D converting board and processed with PC software. Additional details are available in Kountouris' thesis (1999).

5.1.2 Testing Input and Output

Kountouris reported 23 wear tests with input parameters list in Table 5.2. Stainless steel was used as rotating ring material and lubricant was selected to be engine oil (10W30). The total experiment time was two hours for each different set of input. During each tests, the device was first turned on without coolant for 15 minutes, then the cooling system was turned on and the system was operated for the remainder of the time.

Table 5.2 Wear tests input parameters [Kountouris, 1999]

Test Name	Load (lb)	Speed (RPM)	PV (psi ft/min*)	Cooling type	\dot{V} (scfm**)	P_{in} (psig***)	Coolant Flow Rate (Kg/s)
10-2500	10 (4.5N)	2500	13661	Micro Heat Exchanger	1	5	6.5E-4
10-3000	10 (4.5N)	3000	16393		1.5	15	1.2E-3
10-3600	10 (4.5N)	3600	19672		2	30	2E-3
15-1800	15 (6.8N)	1800	14754	External	3.1	4.5	2E-3
				No Cooling	-	-	-

* 1 Psi.ft/min = ~35 Pa.m/s

** scfm: cubic centimeter per minute

*** psig: pounds force per square inch – guage pressure

5.2. Transient Temperature Distribution Calculation

The main purpose of the following calculation is to find a method to simulate the heat transfer process in the micro posts implanted seal structures. Thus, the transient and steady state temperature distribution in the seal prototype was determined and the relationship between the post density and seal's steady state temperature was found.

5.2.1 Abstraction of the Problem

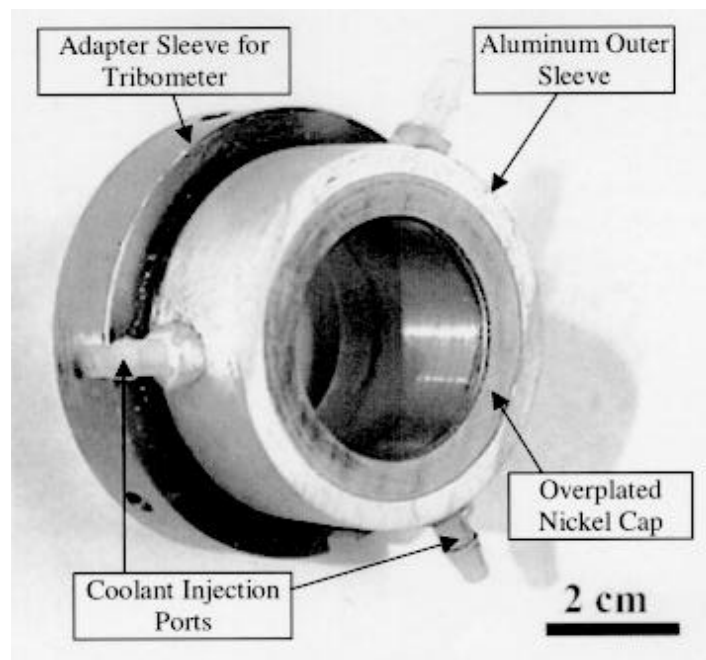


Figure 5.2 Seal prototype [Kountouris, 1999]

According to the original experiment device assembly, as can be seen in Figure 5.2, the system consists of several domains, namely: seal structure with micro heat exchanger, base block, aluminum sleeve and copper mating piece on top.

As shown in Figure 5.3, we can abstract these domains into two cylinders representing copper mating piece and aluminum sleeve respectively, one nickel cylinder with small posts inside for the seal structure and one big cylinder of steel with a hole in one side representing the base block.

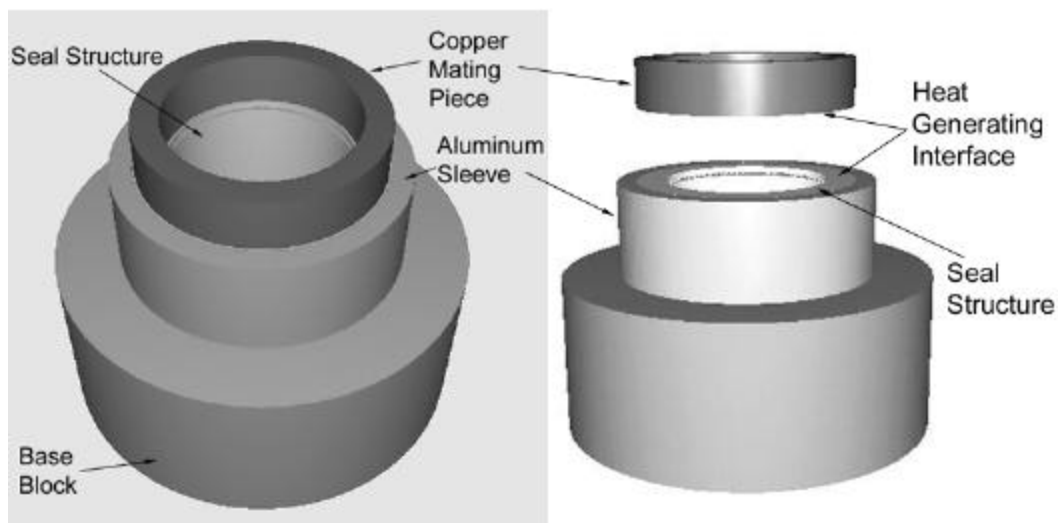


Figure 5.3 Domain of the system

The upper part of the seal structure is composed of an array of small posts, which are assumed to be a group of cylinders. When operating, the coolant will flow across these cylinders from the seal's outside diameter to the inside diameter. This can be treated as a heat transfer problem involving a bundle of smooth tubes in crossflow, which had been examined extensively by Zukauskas [Zukauskas, 1972]. In order to formulate the problem, the system was modeled by making the following assumptions:

- a) The aluminum sleeve has an high thermal conductivity k and its volume is relatively small. More importantly, there is a void space between the aluminum sleeve and the seal structure that is used for coolant flow passage. When coolant flows through this passage, heat will be carried away from surfaces around the passage. On the other hand, in the presence of the aluminum sleeve, the heat transfer capacity of the seal's outer surface is lowered. Considering these two factors, we can assume that if we ignore the aluminum sleeve, the result will not change much.
- b) The heat generated by friction between seal ring and copper mating piece is assumed to be the only source of heat generation. This heat source is assumed to be constant and uniformly distributed on the interface (see Figure 5.3).
- c) Contact resistant at the heat generating interface is assumed to be negligible.
- d) The coolant (air) temperature inside the microstructure is assumed to be uniform and equal to the ambient temperature.
- e) Coefficient of convection heat transfer (h) is uniform around micro posts' outer surface and can be represented using an average value shown later.

5.2.2 Heat Generation

Heat is generated between the copper mating ring and the seal ring when they are rubbing against each other. Usually it is composed of two parts, one is the heat generated on the surface by friction and the other is from viscous shear of the lubricant film between rubbing surface. If the fluid's viscosity is low, the heat from rubbing will be the dominant component. In this situation, the heat can be calculated from:

$$H_m = P_m V A_f f \quad (5.1)$$

where P_m is the pressure on the rubbing surface, V is the relative linear velocity between the two surface, A_f is the contact area, and f is the friction coefficient [Buck, 1999]. When P_m, A_f, V are fixed, as in our situation, friction coefficient f becomes the most important factor for the heat generation. Here, the surfaces are assumed to be in intimate contact. To decrease the coefficient of friction and thus the heat generation, different material pairs should be used for the two mating seal rings. A good material pair usually includes one soft material and a relatively harder material, such as metal carbide and carbon pair or copper and steel pair. Changing the surface properties of the rubbing interfaces, for example by adding hard coating to one the surfaces of the mating pair, can also reach the same result.

If the surfaces are separated by a viscous fluid, then the viscous shear will become the main source of the heat generation. The viscous heat is proportional to viscous shear force, which can be represented as:

$$F = \mathbf{m} \frac{du}{dh} A \quad (5.2)$$

where \mathbf{m} is the absolute/dynamic viscosity, $\frac{du}{dh}$ is the velocity gradient or shear rate of the fluid film, A is the interfacial area. Here, the fluid's viscosity is the primary factor in determining the heat generation.

In our problem, the lubrication condition can be classified as mixed lubrication. In the mixed lubrication regime, the lubrication status is between hydrodynamic/elastohydrodynamic and boundary lubrication. Therefore, most of the contact area is solid contact at the asperity level and only a small portion of the surface is supported by a hydrodynamic film. In other words, the viscous shear will not affect much on the heat

generation and thus can be neglected. Also, since the viscous shear increases as solid contact increases and vice versa, the overall heat generation will not change much if we model the heat generation interface as a dry contact and use equation 5.1 to estimate heat.

The mean pressure P_m is calculated using:

$$P_m = \frac{W}{\mathbf{p}(r_o^2 - r_i^2)} \quad (5.3)$$

where W is the normal load applied to the contact surface, r_o and r_i are the inner and outer radiuses of the upper mating piece.

The linear velocity is computed at the mean radius. Therefore, the average velocity V_{avg} is calculated by:

$$V_{avg} = \frac{\mathbf{p} n(r_o + r_i)}{2} \quad (5.4)$$

where n is the rotating speed in RPM of the driving shaft.

5.2.3 Convection Heat Transfer Coefficient

The convection heat transfer coefficient is not constant between the posts of the seal structure; thus, an average value H_{eff} is used for the calculation. H_{eff} can be determined by average Nusselt number Nu_{av} of the coolant fluid, which is :

$$Nu_{av} = \frac{H_{eff} d_p}{k_f} \quad (5.5)$$

where d_p is the hydraulic diameter associated with the posts and k_f is the thermal conductivity of the coolant.

The average Nusselt number is a function of Reynolds number Re and Prandtl number Pr and varies with different tubes arrangement. Usually, the tubes arrangement is categorized as either in-line or staggered as shown in Figure 5.4. If all rows in a tubes

bundle are aligned, it is said to be arranged in an in-line fashion, Figure 4.5 (a). If alternating rows are offset by some distant, it is arranged in an staggered fashion, Figure 4.5 (b).

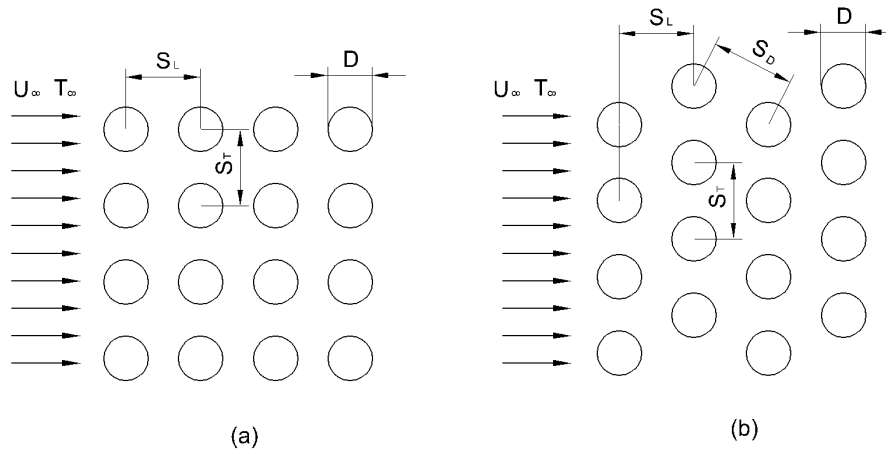


Figure 5.4 Tubes arrangement (a) in-line (b) staggered [Hagen, 1999]

An experimental result for Nusselt number of a bank of tube is given by Zukauskas [Zukauskas, 1972]:

$$Nu_{av} = C_z C Re^m Pr^n \left(\frac{Pr}{Pr_w}\right)^{0.25} \quad (5.6)$$

where Pr_w is Prandtl number evaluated at the wall temperature. The coefficients of the above equation is given by the following table.

Table 5.3 Coefficients in equation 5.6 [Zukauskas, 1972]

	Re	C	m	N
In line tubes bundles	$10^0 - 10^2$	0.9	0.4	0.36
	$10^2 - 10^3$	0.52	0.5	0.36
	$10^3 - 2 \times 10^5$	0.27	0.63	0.36
	$2 \times 10^5 - 2 \times 10^6$	0.033	0.8	0.4
Staggered tube bundles	$10^0 - 5 \times 10^2$	1.04	0.4	0.36
	$5 \times 10^2 - 10^3$	0.71	0.5	0.36
	$10^3 - 2 \times 10^5$	$0.35(a/b)^{0.2}$	0.6	0.36
	$2 \times 10^5 - 2 \times 10^6$	$0.031(a/b)^{0.2}$	0.8	0.36

Where $a = \frac{S_T}{D}$ and $b = \frac{S_L}{D}$.

Since equation 5.6 is for number of tube rows equal to or more than 16. An extra coefficient C_z is needed as the correction factor for tube banks consisting of less than 16 rows. C_z is determined by Figure 5.5 below where z represent number of tube rows.

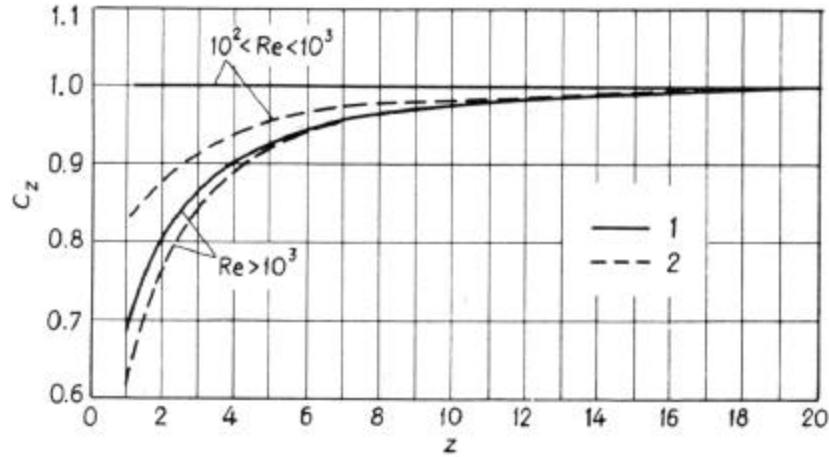


Figure 5.5 Correction factor for tube banks consisting 16-20 rows [Zukauskas, 1972]

The Reynolds number in the equation is defined as

$$Re = \frac{uD}{\nu} \quad (5.7)$$

where ν is fluid's kinematic viscosity, u is the reference velocity. u is obtained from maximum velocity of the fluid U_{\max} in the tube bank, which occurs in the transverse plane.

$$U_{\max} = \frac{S_T U_{\infty}}{S_T - D} \quad (5.8)$$

Or

$$U_{\max} = \frac{S_T U_{\infty}}{2(S_D - D)} \quad (5.9)$$

in staggered tube distribution whenever $S_D < \frac{S_T + D}{2}$. S_D is calculated from the

following relation [Hagen, 1999]: $S_D = \sqrt{S_L^2 + \left(\frac{S_T}{2}\right)^2}$.

In our case, we that assume the posts distribution is staggered and $S_D > \frac{S_T + D}{2}$, therefore equation 5.8 is used. However, the distant between the posts are different from inner ring to outer ring of the seal structure. We take the average distant to estimate maximum fluid velocity. Thus the velocity equation becomes:

$$U_{\max} = \frac{\dot{m} p_d}{\mathbf{p}(r_o + r_i) p_h (p_d - D)} \quad (5.10)$$

where \dot{m} is the mass flow rate of the coolant, p_d is the space between centers of posts, p_h is the height of the post, and D is the characteristic diameter of the posts. If the posts are not cylindrical, hydraulic diameter D_h should be used for the characteristic diameter, which is calculated by the formula:

$$D_h = \frac{4A_{cross}}{P_p} \quad (5.11)$$

where A_{cross} is the post cross section area, P_p is the post perimeter.

In equation 2.6, Prandtl number Pr is defined as:

$$Pr = \frac{\mathbf{m}c_p}{k_f} \quad (5.12)$$

where c_p is the specific heat of the fluid and k_f is the thermal conductivity of the fluid.

For the fluid of air (as in our case), Pr is constant and around 0.7. So the term $\frac{Pr}{Pr_w}$ in

equation 2.6 is cancelled.

5.2.4 Formulation of the Problem

Because there is no internal source in each domain and the thermal properties are constant in each of the components. The governing equation in this problem is that of heat conduction for homogeneous isotropic solid, viz.

$$\nabla^2 T = \frac{\partial^2 T}{\partial x^2} + \frac{\partial^2 T}{\partial y^2} + \frac{\partial^2 T}{\partial z^2} = \frac{r c_p}{k} \frac{\partial T}{\partial t} \quad (5.13)$$

where T is the temperature and r , c_p , and k are mass density, specific heat and thermal conductivity of the components, respectively. Figure 5.6 shows the diagram of the system to be cut in the middle. As can be seen in the figure, since the aluminum sleeve is ignored, there are totally 11 surfaces (boundaries).

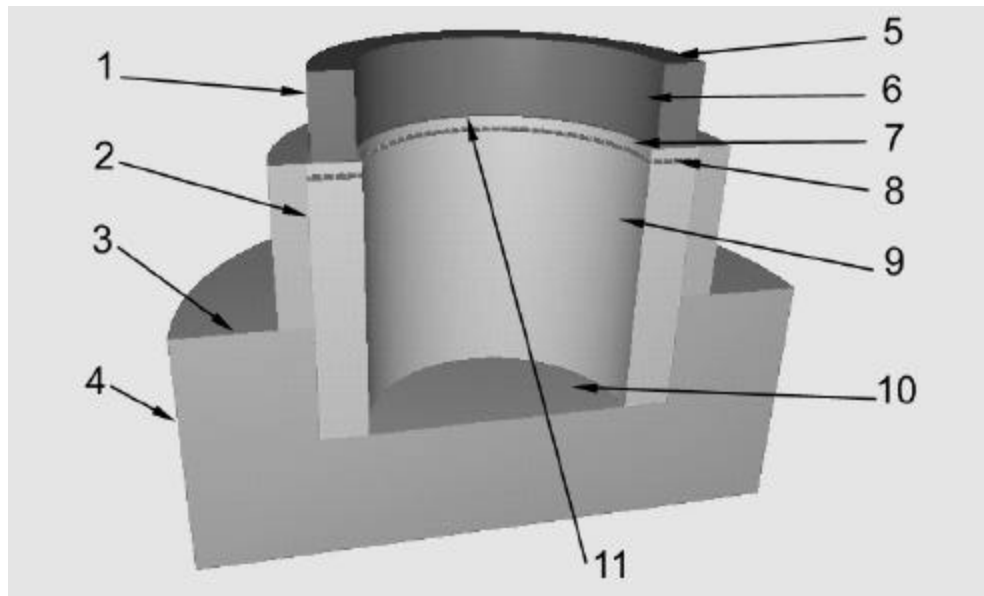


Figure 5.6 Boundaries of the system. Surface 1,5,6,7,9,10 are insulated boundaries; 2,3,4 boundaries are exposed to air; 11 is the heat generating boundary; 8 is the boundary exposed to coolant.

According to Kountouris' experimental setup [Kountouris,1999], the copper mating piece is insulated from the environment. Therefore, there is no heat transfer through surfaces 1, 5 and 6. The boundary condition on these surfaces are as follows.

$$\text{On } \mathfrak{R}_1, \mathfrak{R}_5, \mathfrak{R}_6 : \quad q_{conv} = 0 \quad (5.14)$$

The driver adapter on top, the copper mating piece, the seal structure and base block are attached to form a chamber inside the whole system during the experiment. In this chamber, especially in the lower part of it, the airflow rate is low and therefore heat flux from surfaces 7, 9 and 10 to the air in the chamber is low. We can assume that those surfaces are adiabatic. Thus, equation 5.14 can also serve as the boundary condition for surfaces 7, 9 and 10. Thus,

$$\text{On } \mathfrak{R}_7, \mathfrak{R}_9, \mathfrak{R}_{10} : \quad q_{conv} = 0$$

Ignoring the aluminum sleeve, surfaces 2, 3 and 4 are all exposed to the ambient and lose heat by convection. Their boundary condition is:

$$\text{On } \mathfrak{R}_2, \mathfrak{R}_3, \mathfrak{R}_4 : \quad q_{conv} = h(T - T_\infty) \quad (5.15)$$

where h is the convection heat transfer coefficient of air, T_∞ is the ambient temperature. Boundary 8 is actually a series of surfaces, which represent the posts' outer surfaces, upper surface of the seal substrate, and lower surface of the overplate. These surfaces are subject to the convection cooling process by the coolant flow. Therefore, they have the boundary condition of

$$\text{On } \mathfrak{R}_8 : \quad q_{conv} = H_{eff}(T - T_\infty) \quad (5.16)$$

where H_{eff} is the average heat transfer coefficient obtained from section 5.2.3.

Heat generation occurs on boundary 11. It consists of two surfaces: lower surface of copper mating piece and upper surface of the seal structure. Because the area difference of these two surfaces is small, we can assume they have the same area. The boundary condition for 11 is,

$$\begin{aligned} \text{On } \mathfrak{R}_{11} : \quad k \frac{dT}{dz} &= -q_1 \\ k \frac{dT}{dz} &= q_2 \end{aligned} \tag{5.17}$$

where q_1 is the heat flux to the copper mating ring and q_2 is the heat flux flowing to the heat exchanger.

On boundary 11, since neither of the contacting surfaces is insulated, the frictional heat H_m , which can be calculated from equation 5.11, will be partitioned between these two surfaces. We then have the relationship,

$$\text{On } \mathfrak{R}_{11} : \quad q_1 + q_2 = H_m \tag{5.18}$$

To determine q_1 and q_2 , we need another equation. We assume the two surface have the same temperature. That is,

$$\text{On } \mathfrak{R}_{11} : \quad T_1 = T_2 = T \tag{5.19}$$

The initial condition at time $t = 0$ is:

$$\text{At } t=0 \quad T = T_\infty \tag{5.20}$$

The above set of equations and related boundary conditions are solved using the Finite Element Method. For this purpose, software FLEXPDE, which is a general-purpose finite element model builder and numerical solver, is used. The program script and description are listed in Appendix I. Some calculation result will be shown in section 5.4.

5.2.5 Geometric Modeling

The size of the posts is so small (~0.2mm in diameter and ~0.5mm in height in our case) that in each of the seal structure there will be hundreds to thousands of posts (600 to 6000 in our case.) Therefore, if calculating as a whole in the FEA program, after

meshing, there will be hundreds of thousands of elements. This will be beyond the capability of the most powerful computer we can access.

By observing the shape of the modeling, we would find that the seal structure system is composed of many identical segments arranged periodically around an axis. Therefore, by taking a common pattern from the whole system and add periodicity boundary conditions to it, we can solve the problem and avoid a large amount of redundant computational load. Thus the calculation work could become quick and simple. The sector shown in Figure 5.7 is the image of this common pattern.

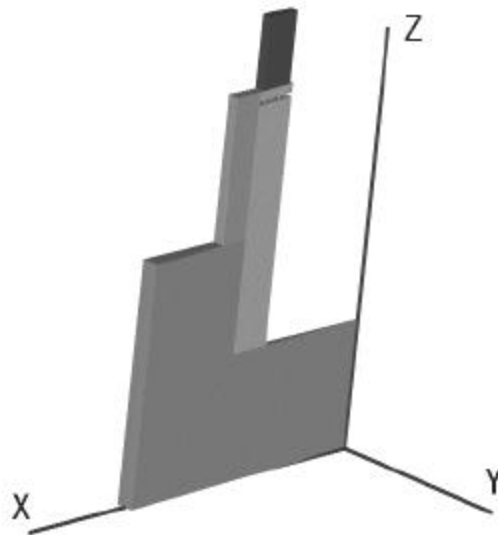


Figure 5.7 Geometry model of the problem

Except for the posts, all the geometric components of the modeling are circular. They are periodic whenever an evenly divided sector is taken. To make posts' distribution suitable for the calculation, we suppose that the posts are distributed in a series of concentric circles, the distant between adjacent circles are the same and equal to the spacing in the original posts distribution, and on each circle the posts number are assumed to be the same. The number of posts N_m on each circle is equal to that on the

circle with mean diameter of the structure. See Figure 5.8 for detail. The common pattern is shown in Figure 5.8(c). It is $\frac{1}{N_m}$ of the system.

Suppose the angle of the pattern sector is $\mathbf{q} = \frac{2\mathbf{p}}{N_m}$. Then, in Cartesian coordinate, the periodic relation of the pattern will be:

$$\begin{aligned} x' &= x \cos(\mathbf{q}) + y \sin(\mathbf{q}) \\ y' &= -x \sin(\mathbf{q}) + y \cos(\mathbf{q}) \end{aligned} \quad (5.21)$$

where x, y are the original coordinates, x' and y' are coordinates of pattern next to the original one.

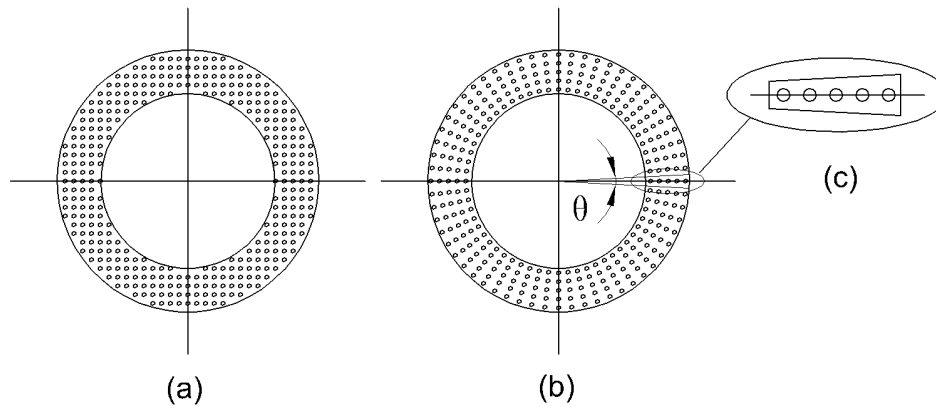


Figure 5.8 Schematic of posts distribution. (a) original distribution (b) distribution used in calculation (c) a common pattern

5.3 Posts Structural Analysis

5.3.1 Introduction

The seal prototype is composed of three layers shown in Figure 5.9: a top layer which is a solid ring of 500~1000 microns thick, a bottom layer which is a cylinder of 20~30 millimeters in height and the micro posts layer which is made up of hundreds to thousands of small cylindrical posts uniformly distributed between the top and bottom layer.

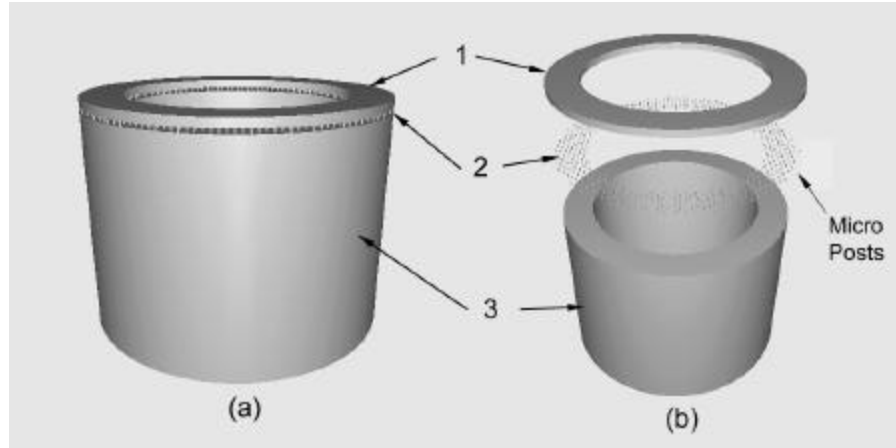


Figure 5.9 Seal prototype and its three layer of components: (1) top layer (2) micro post layer (3) bottom layer

The micro posts are typically 200 microns in diameter or 180 microns in side length and 500 micron in height. These micro posts act as small pin fins inside the seal and are capable of increasing the heat transfer capability of the entire seal structure. This has been proved by aforementioned experiments [Kountouris, 1999]. However, adding a layer of posts underneath the surface of a mechanical seal can potentially weaken its overall strength. The smaller the post density, the smaller the overall strength of the seal will be. Thus, a method to calculate the maximum stress of the posts and to find out the relation between post density and maximum torque the seal can sustain is necessary for the design and optimization of the seal structure.

In the calculations reported below, fundamental theories and methods in mechanical of material are implemented to analyze stress distribution of the micro posts under the condition similar to that of mechanical seals.

5.3.2 Method For Calculating Stress From Friction Torque

5.3.2.1 Friction Torque

We starts from the basic law of friction, known as Amontons' law:

$$F_f = f.N \tag{5.22}$$

where f is the coefficient of kinetic friction and N is the normal force acting on the area of contact.

Therefore, friction torque can be presented as

$$T = F_f . r = f . N . r \quad (5.23)$$

where r is the distant between friction force and the center of rotation. Here we assume that the normal force is uniformly distributed over the area of contact. Since the value of r varies along the ring radius, the total torque is evaluated by integration of (5.23) from the inner to the outer radius.

$$T = \int_{r_i}^{r_o} \frac{f . N}{\mathbf{p} . (r_o^2 - r_i^2)} 2\mathbf{p} r^2 dr = \frac{2f . N}{3(r_o^2 - r_i^2)} (r_o^3 - r_i^3) \quad (5.24)$$

If $r_i=0$, which implies that the ring becomes a solid cylinder, the friction torque becomes:

$$T = \frac{2f . N}{3} r_o \quad (5.25)$$

5.3.2.2 Stress in the Seal Structure

We consider that the seal runs under normal operating condition, which means that the mating parts of the seal run in a constant speed and that normal force between mating surfaces is constant. Under this circumstance, the seal structure is in a static equilibrium state.

We now examine the seal according to different layers.

a) Top Layer

Four types of loads act on the top layer: normal force on top of the layer N , friction force F_f , shear forces from the micro posts, and forces upward from the posts.

Because of static equilibrium, in vertical direction we have:

$$N = n . f_p \quad (5.26)$$

where N is the normal force, n is the total number of posts, f_p is the force that each posts gives to the top layer. Thus

$$f_p = \frac{N}{n} \quad (5.27)$$

Another relationship we can obtain from equilibrium is as follow:

$$T = \sum T_i \quad (5.28)$$

where T is the friction torque, T_i is the torque caused by the shear force of one post with respect to seal center .

Let us suppose that the posts are arranged in concentric circles whose center is coincident with that of the top ring. Denote the radius of these circles by r_1, r_2, \dots, r_n and assume that there are n circles of posts. Thus

$$T_i = F_i \cdot r_i = \mathbf{t}_i \cdot A \cdot r_i \quad (5.29)$$

where F_i is the shear force on the posts located in the circle with radius of r_i , A is the cross section area of one post, and \mathbf{t}_i is the shear stress on the post.

Below the material's yield stress, the shear stress for a given post varies linearly with the radius of the post location. Therefore, for the ensemble of posts we have the following relationship:

$$\frac{\mathbf{t}_1}{r_1} = \frac{\mathbf{t}_2}{r_2} \dots = \frac{\mathbf{t}_i}{r_i} = \frac{\mathbf{t}_{i+1}}{r_{i+1}} \dots = \frac{\mathbf{t}_k}{r_k} \quad (5.30)$$

The torque then can be written as:

$$T = \sum_{i=1}^k T_i = \sum_{i=1}^k n_i r_i \cdot \mathbf{t}_i \cdot A \quad (5.31)$$

where n_i is the number of posts distributed on the circle with radius of r_i . Using equation 5.30 we can get $k-1$ sets of equations:

$$\mathbf{t}_i \cdot r_{i+1} = \mathbf{t}_{i+1} \cdot r_i \quad i = 1, 2, \dots, k-1 \quad (5.32)$$

Combining equation 5.31 and 5.32, we will have k equations and k unknowns, The above set of equations can be put into a matrix form as shown below:

$$\begin{bmatrix} r_2 & -r_1 & 0 & \dots & 0 \\ 0 & r_3 & -r_2 & \dots & 0 \\ 0 & 0 & r_4 & \dots & 0 \\ \dots & \dots & \dots & \dots & \dots \\ n_1 r_1 A & n_2 r_2 A & \dots & \dots & n_k r_k A \end{bmatrix} \cdot \begin{bmatrix} \mathbf{t}_1 \\ \mathbf{t}_2 \\ \dots \\ \dots \\ \mathbf{t}_k \end{bmatrix} = \begin{bmatrix} 0 \\ 0 \\ \dots \\ 0 \\ T \end{bmatrix} \quad (5.33)$$

b) Micro Posts Layer

Using equation 5.33, the shear stress acting on the top surface of each posts circle can be found. Thus, the total shear force exerted on a single post is:

$$F_s = \mathbf{t}_i A \quad (5.34)$$

where A is the cross section area of the post.

Since the maximum stress on the posts is desired, only those posts that receive the largest shear force, need to be considered. They are the posts located in the outermost circle with a shear stress of \mathbf{t}_k .

To simplify the problem, we assume that the post is a cantilever beam as shown in Figure 5.10. The cantilever beam is fixed on the bottom layer and has two loads on its upper surface: one is the normal force F_i , which is from the normal load acting on the seal, and the other is the shear force which is originated from the friction force.

. The normal load will cause a compressive stress in the post given by:

$$\mathbf{s}_p = \frac{N}{n \cdot A} \quad (5.35)$$

The shear force F_s will act as a bending force on the post. It will cause bending moment and shear stress. The bending moment is

$$M = F_s h \quad (5.36)$$

where h is the height of the post.

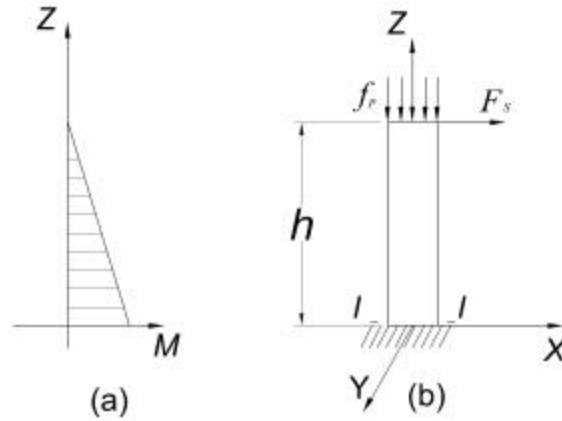


Figure 5.10 Force and moment on a single post (a) bending moment diagram (b) force diagram

As can be seen from the bending moment diagram in Figure 5.10(a), the most dangerous cross section in the post is section $I-I$. The bending stress in this cross section can be calculated from:

$$s_{I-I} = \frac{My}{I_z} \quad (5.37)$$

where I_z is the moment of inertia for the cross section, for a circular cross section

$$I_z = \frac{\mathbf{p}.d^4}{64}, \text{ where } d \text{ is the diameter of the post cross section.}$$

Because of the existence of the normal load, the total tension/compression stress in any point of section $I-I$ is

$$s_{I-I} = \frac{N}{n.A} + \frac{M}{W} = \frac{N}{n.A} + \frac{M.64y}{\mathbf{p}.d^4} \quad (5.38)$$

Using equation 5.38, we can determine the maximum tensile stress and maximum compressive stress on the post. Then after comparing the tensile stress with material's yield stress, it can be determined whether the posts will deform plastically. In this

fashion, whether structural integrity of the seal can be determined. A commercial finite element analysis software (ANSYS) is also used for obtaining a more precise result. The results are presented in section 5.4.1.

5.3.2.3 Changing Posts Rectangle Distribution To Concentric Distribution

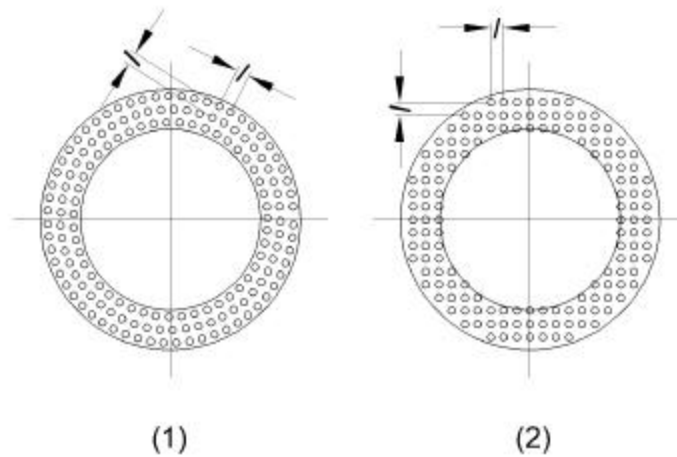


Figure 5.11 Post distribution transformation. (1) concentric distribution (2) rectangle distribution

Usually the posts are evenly distributed in rectangle form for the ease of manufacturing with a distant l between each post. In order to use the method mentioned in the last section, we must transform this kind of posts distribution to a concentric distribution. We assume that all posts are located in concentric circles, the radius difference between each adjacent circle is l and around each circle, the space between each posts is l as show in Figure 5.11. After this transformation, the post density and distant between each post will not change much. For example, when space between of posts is 0.285 and the outer diameter and inner diameter of the seal ring are 35.56mm and 26.49mm respectively, the actual total posts number is 5440 [Kountouris, 1999], the calculation result is 5123. Thus, the transformation will not affect much on the final result.

5.3.2.4. Method For The Calculation of Maximum Friction Torque

Using the method above in the reverse order, we can calculate the maximum friction torque that a seal structure can sustain before it begins to deform plastically. We assume that under the maximum friction torque the material reaches its tensile strength \mathbf{s}_s . Because normal force is a compression force, we have the equation:

$$\mathbf{s}_s = \mathbf{s}_{1T} = -\frac{N}{n.A} + \frac{M.32}{\mathbf{p}.d^3} \quad (5.39)$$

where

$$M = \mathbf{t}_k . h . A \quad (5.40)$$

Using equation 5.30, we have

$$\mathbf{t}_i = \mathbf{t}_k . \frac{r_i}{r_k} \quad (5.41)$$

Therefore,

$$T = \sum_{i=1}^k A . n_i . r_i^2 . \frac{\mathbf{t}_k}{r_k} \quad (5.42)$$

Using equations 5.24, 5.39, 5.40 and 5.42, we arrive at the following relationship:

$$\mathbf{s}_s = -\frac{N}{n.A} + \frac{64.N.m(r_o^3 - r_m^3)r_k h}{2.\mathbf{p}.d^3(r_o^2 - r_m^2).\sum_{i=1}^k n_i r_i^2} \quad (5.43)$$

The index k , which indicates the maximum circle number of the posts distribution and can be calculated from

$$k = \text{floor}((r_o - r_m)/l) \quad (5.44)$$

where l is the distant between each posts. The function *floor* is used to calculated the largest integer that is less than or equal to $(r_o - r_m)/l$.

Using equation 5.43, maximum normal force N can be derived. Thus, the maximum friction torque T that a seal can sustain can also be obtained.

5.3.3 Matlab Code for Calculation of Stress Distribution of the Seal Structure

The calculation method introduced in section 5.3.2 can be implemented using MATLAB scripts. The codes are listed in Appendices II and III.

5.4 Results and Discussion

5.4.1 Post Stress Calculation

5.4.1.1 Maximum post stress under friction torque

The geometry of the seal structure used in this calculation are the same as that in the experiments on the seal prototype. The input parameters are list in Table 5.4. A series of post-to-post distance values are selected to simulate different post density so that the relation between post density and maximum post top shear stress can be found.

Table 5.4 Input parameter for stress calculation

Parameter	Value
Normal Force (N)	10
Friction Coefficient	0.1
Outside Dia. of Seal (m)	0.03556
Inside Dia. of Seal (m)	0.02649
Post Dia. (mm)	0.180
Post Height (mm)	0.50
Post Material	Ni

Table 5.5 shows the different post distributions used in the calculation. The post distributions with the largest and the smallest post densities were selected from the real seal prototype design (see Table 3.1 and 3.2). The post-to-post distant in the rest distributions are evenly selected in between the above two.

The maximum shear stress on the top of posts for different post densities were calculated using equation 5.33. The maximum compression stresses for posts were also

computed for the purpose of comparison. This was achieved by using equation 5.38 and setting the variable y to $d/2$.

Table 5.5 Different post distributions

Distant Between Posts (mm)	Post Density (post/mm²)	Percent Filled (%)	Total Post Number
0.285	12.31	31.31	5123
0.428	5.46	13.88	2273
0.571	3.07	7.80	1191
0.714	1.96	4.99	816
0.857	1.36	3.46	567
1.0	1.00	2.54	388

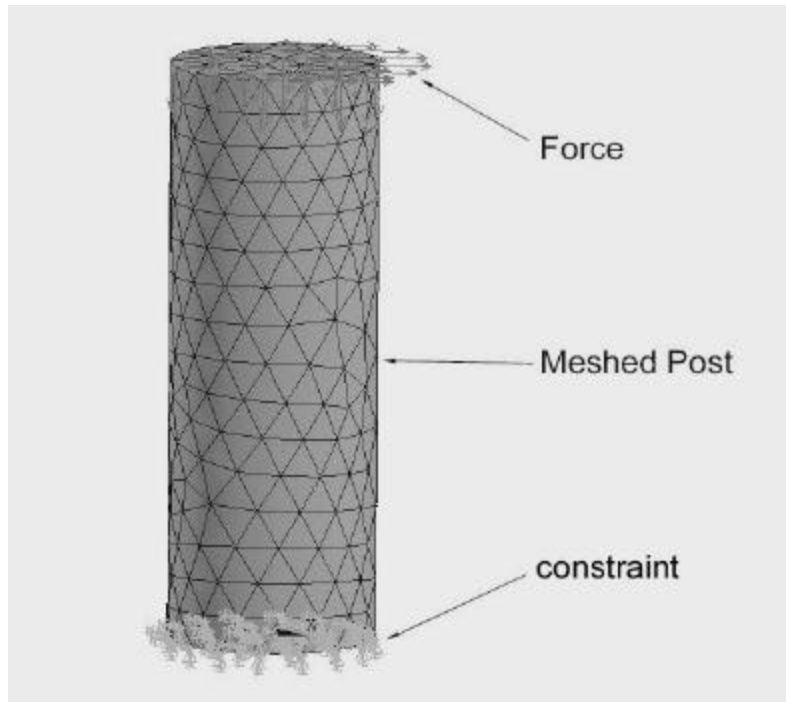


Figure 5.12 Post model meshed and loaded

To determine a more accurate prediction of the maximum stress in the posts, the FEA method was used. We selected software ANSYS for this purpose. A post is modeled as a cylinder. Since the bottom of each post has very little displacement, we assume it is fixed with zero displacement. All the forces are loaded on the top surface of each post. These

forces include a face load and a compression force. The face load comes from the shear stress obtained in the last step. It is perpendicular to post's axis. The compression force is from the normal load, which evenly distributed on the surface pointing downward. The post modeling after meshing and loading is shown in Figure 5.12. Three-D element SOLID185 is selected as element type, which has eight nodes, each with three degree of freedom UX, UY and UZ.

The problem was solved as a static FEM problem. A typical stress contour is shown in Figure 5.13. As expected intuitively, the maximum stress occurred at the lower front part of the post with respect to the shear force direction. The results of a series of calculations are shown in Table 5.6. The values of maximum compression stress are seen to be close to their corresponding maximum stress computed from ANSYS. Since the compression or tensile stress is the dominant source of stress for the posts in our situation, these results prove that the ANSYS predictions are reliable.

Table 5.6 Calculation results for posts' stresses

Post Density (post/mm²)	Maximum Shear Stress on Posts' Top (MPa)	Maximum Compression Stress (Pa)	ANSYS Result of Maximum Stress (Pa)
12.31	0.008560	266922	219625
5.46	0.019168	598843	492817
3.07	0.036288	1136348	935480
1.96	0.052715	1653030	1.36E+06
1.36	0.075398	2368599	1.95E+06
1.00	0.109113	3437547	2.83E+06

The maximum Von Mises Stress vs. post density plot is shown in Figure 5.14. By analyzing this plot, it is found that the maximum Von Mises stress decreases drastically with increasing the post density below 3 posts/mm². For post densities greater than 6 posts/mm², the maximum stress is remains relatively constant. A relatively high post

density is not necessarily advantageous because of the difficulties that may arise in passing the cooling medium around the posts. That is to say, the functionality of the heat exchanger may be compromised. Therefore, post densities in the range of 3 ~ 6 posts/mm² should be chosen for optimum performance both in terms of the structural integrity and the heat transfer viewpoint.

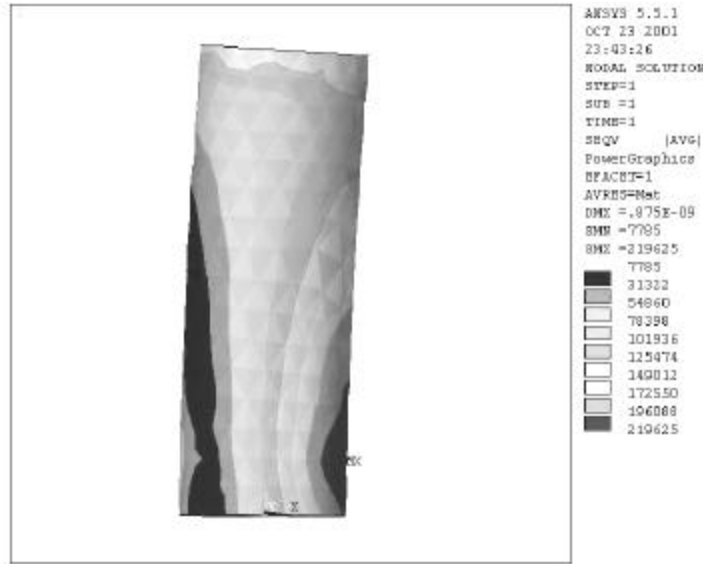


Figure 5.13 Contour plot of Von Mises stress distribution of a post

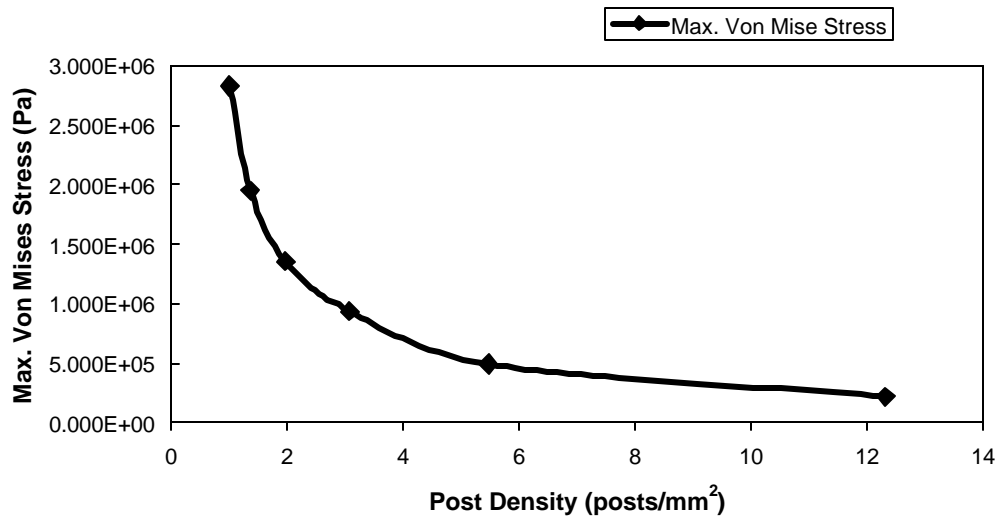


Figure 5.14 Von Mises stress vs. post density

The calculation results can be used to predict post failure if the proper critical strength is known. We should point out that the critical strength should not be the material's tensile strength, because the strength of the bonding between the post and strength will be much lower than pure material's tensile strength. The bonding strength may be a function of many factors such as electro-plating methods, the material of substrates surface condition. Experiments should be carried out to find out bonding strength under different manufacturing conditions. This is beyond the scope of current work.

5.4.1.2 Maximum Normal force for Seal structures with posts

Using the equations derived in section 5.3 and geometry parameters the same as section 5.4.1.1, maximum normal force and friction torque can be calculated for Nickel posts. As pointed out the Ni-substrate bonding strength should be used for this purpose. In the absence of available data on this type of bonding strength, we take the tensile strength of pure Ni (59×10^6 Pa) as the critical strength and compute the maximum load capacity. The results are summarized in Table 5.7.

Table 5.7 Post density and maximum load capacity

Post Density (posts/mm²)	Max. Normal Force (N)	Max. Friction Torque (N.m)
12.31	2828.20	4.400
5.46	1265.97	1.965
3.07	670.73	1.038
1.96	462.54	0.715
1.36	324.14	0.500
1.0	224.83	0.346

The results show a roughly linear relationship between the post density and the maximum normal force or friction torque. Therefore, the greater the post density, the higher the seal structure's strength will be. This data should be examined in conjunction with the heat transfer capability of the seal to determine the optimum post density. It is

important to point out the data presented in Table 5.7 does not take stress concentration into account. The existence of stress concentration at the post-substrate junction may reduce the maximum load capacity of the structure.

5.4.2 Transient Heat Transfer Calculation

5.4.2.1 Comparison between Calculation and Experimental results

The aim of the transient heat transfer calculation is to develop a mathematical model to simulate the actual process in the experiment. Thus, the best test for verifying the simulation results is to compare with the experiments, which were introduced in section 5.2. We select Test 10-3000 shown in Table 5.2, of which some parameters for the experiment are listed in Table 5.5. In our case, the seal structure is stationary during the test and the mating pieces is spinning at a speed of 3000 rpm, therefore the coefficient of convection heat transfer around the seal structure is no longer that of natural heat convection. Simple convective heat transfer analysis reveals that when a shaft with diameter the same as the seal structure ($D = 1$ in) rotates at 3000 rpm, the convection heat transfer coefficient h on its outer surface is around $60 \text{ W}/(\text{m}^2\text{K})$. If the shaft is stationary, the h value outside its surface is $5\sim 12 \text{ W}/(\text{m}^2\text{K})$, corresponding to free convection. Our situation will be between these two limits. So, we choose a value $40 \text{ W}/(\text{m}^2\text{K})$ in our calculations.

In Kountouris' experiment, the coolant was not supplied in the first 15 minutes. According to the experimental result, the seal temperature reached $\sim 332 \text{ K}$ before the coolant was supplied. Since in the current calculations, we did not consider the stage without coolant, in order to make the simulation result more comparable to the empirical result, the initial temperature 332 K was selected in the calculation.

The empirical and calculation results are shown in Figure 5.15 (a) – 5.15 (d). In each figure, the simulation result of time-temperature curve for certain coolant flow rate is plotted together with its corresponding experimental curve for the sake of comparison.

Table 5.8 Parameters in heat transfer calculation

Parameter	Value
Normal Force (N)	4.54
Friction Coefficient	0.1
Ambient Temperature (K)	298
Initial Temperature (K)	332
Convection Heat Transfer Coefficient h (W/m ² K)	40

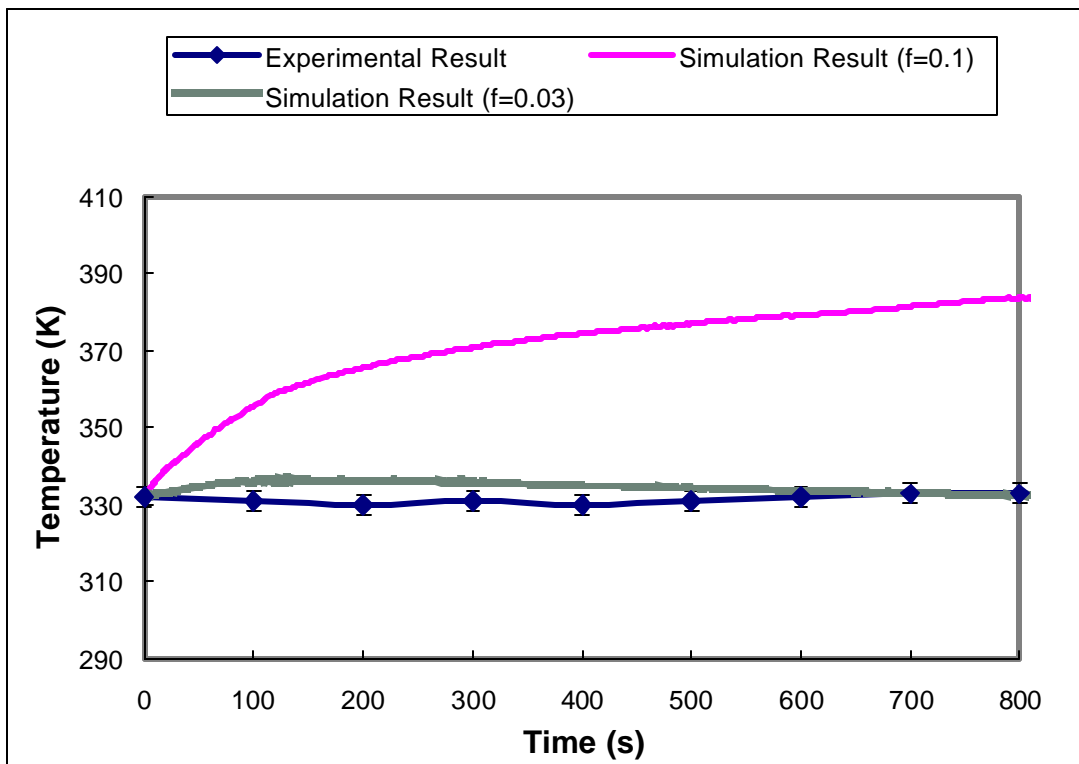


Figure 5.15 (a) Temperature variation with time for no coolant situation

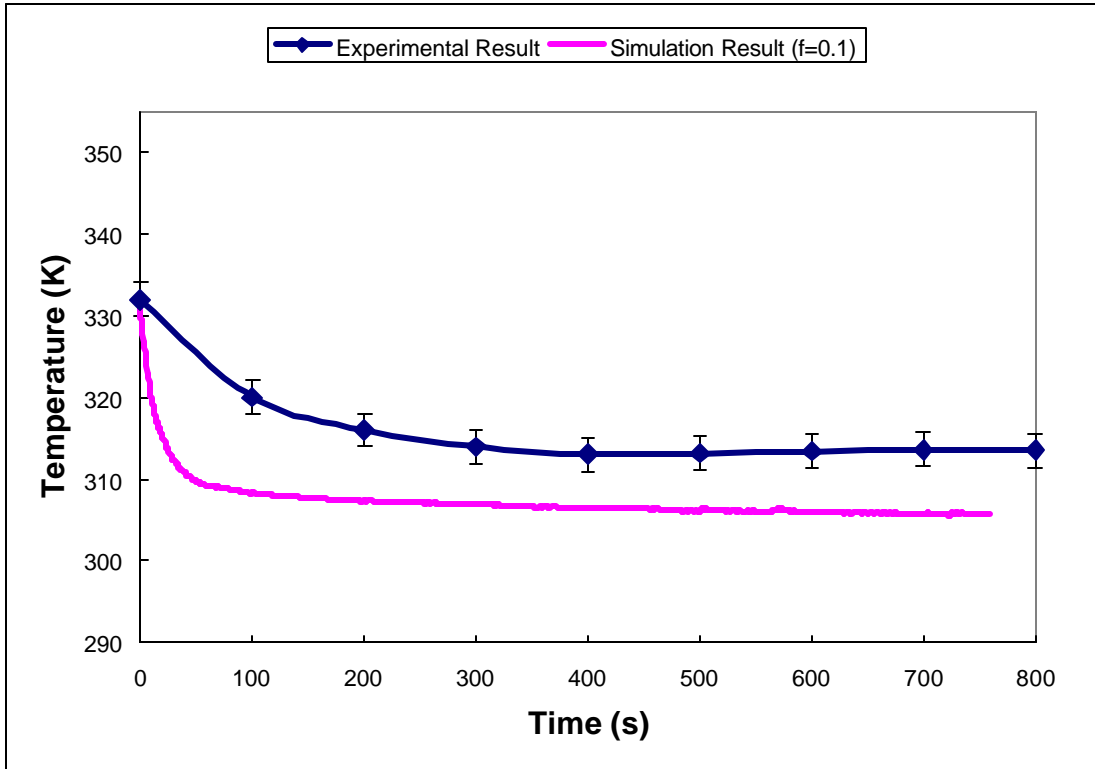


Figure 5.15 (b) Temperature variation with time for coolant flow rate of $6.7E-4$ kg/s

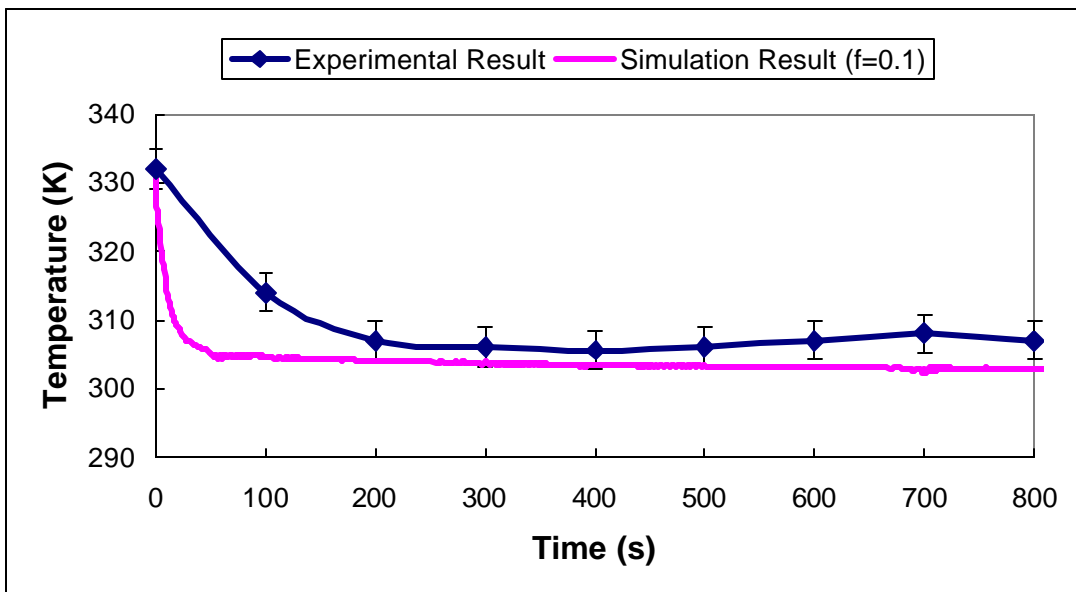


Figure 5.15 (c) Temperature variation with time for coolant flow rate of $1.19E-3$ kg/s

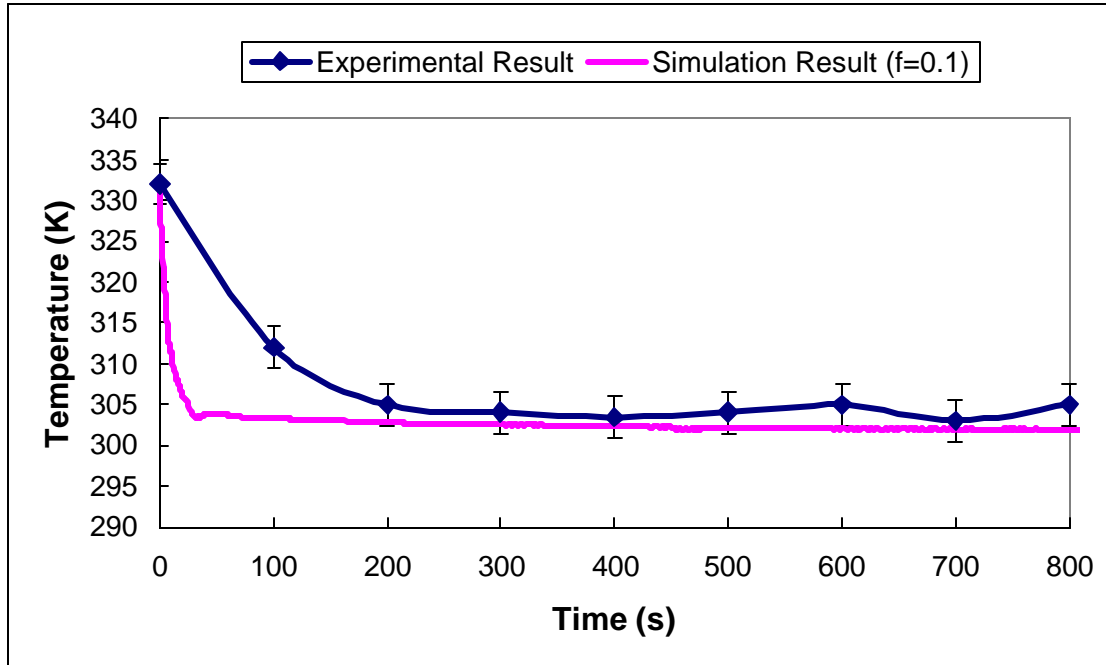


Figure 5.15 (d) Temperature variation with time for coolant flow rate of 2E-3 kg/s.

As can be seen from Figure 5.15, the duration in which steady states were reached in the simulations are close to that from the empirical results. The simulation results for all with coolant cases have a $\pm 5^{\circ}\text{C}$ difference from the empirical results. This indicates a good agreement between the simulation and the experimental results when a coolant is supplied to the heat exchanger.

The biggest difference in steady state temperature occurred in the no coolant case, in which the empirical result was around 330 K while the simulation result reached ~ 390 K and the temperature was still increasing as shown in Figure 5.15(a). One important reason for this difference is that we did not take seals' wears into account. When no coolant was presented in the micro heat exchanger in the experiment, the seal face temperature was very high. Therefore, an appreciable amount of wear in the contact area took place. It is likely that after a short period of running, a wear track would form in the contact area on the seal structure's contacting surface. Since all the tests by Kountouris (1999) were

lubricated with a liquid lubricant (engine oil), the lubricant would then flow into the wear track, thus altering the contact condition between the surface of the seal structure and its mating part. Under these circumstances, the lubrication regime can easily shift from mixed / boundary lubrication to the elastohydrodynamic lubrication where the friction coefficient would drop and the heat generation would decrease. In the simulations, we assumed that the heat generation remains the same throughout the entire process. This is thought to be the main reason that causes the temperature difference in “no coolant” case. To illustrate this, another simulation was done with decreased coefficient of friction (0.03). The result is also shown in Figure 5.15 (a). The result curve with decreased coefficient of friction is very close to the experiment result.

Other factors that may contribute to the temperature difference for all cases are:

- 1) The coolant temperature was assumed to be constant and equal to ambient temperature. In reality, the coolant will absorb heat and thus its temperature will rise when passing the passage between posts. Therefore, the heat removed from the seal prototype will be less than that in the simulation.
- 2) The post distribution is much more complicated than that assumed in the simulation;
- 3) The chamber enclosed by the seal was assumed to be perfectly insulated. In reality, there is a small amount of coolant flow inside.

Results obtained experimentally or by simulations all show that the micro posts have a pronounced ability to remove a significant amount of heat from the seal structures to the coolant and thus cool down the seal structures in operation. In the next section, we will try to determine a relationship between post density and the steady state temperature seal structure.

5.4.2.2 Relationship between Post Density and Steady State Temperature

Using the model described in section 5.2, a series of steady state simulations were performed to examine the relationship between the post density and the steady state temperature on the contacting interface. This was achieved by keeping the input parameters the same as those described in section 4.5.2.1 and changing the post density. The coolant flow rate for all the calculations was set to 1.2E-3 kg/s and the initial temperature was 332 K.

Table 5.9 Post density and steady state temperature

Post Density (posts/mm²)	Total Post Number	Number of Posts in the Model	Nusselt Number Nu	Convection Coefficient Between Posts(W/m²K)	Steady State Temperature (K)
12.31	5123	15	15.91	2324	303
5.46	2273	10	10.07	1472	317
3.07	1191	7	9.13	1335	336
1.96	816	6	8.82	1289	354
1.36	567	5	8.54	1248	360
1.0	388	4	7.88	1151	376

Temperature time responses for each of the above post densities are shown in Figure 5.16.

As shown in figure 5.16, all the curves tend to converge to a steady state temperature. Based on the initial temperature (332 K), only two of the seals (with post densities of 5.46 and 12.31) actually cooled down. The predicted steady state temperatures as a function of the post density are shown in Table 5.9 and Figure 5.16. The plot clearly shows that within post density 1~12.31 posts/mm², the seal steady state temperature decreases as post density increases. The more the post number, the better the seal thermal performance.

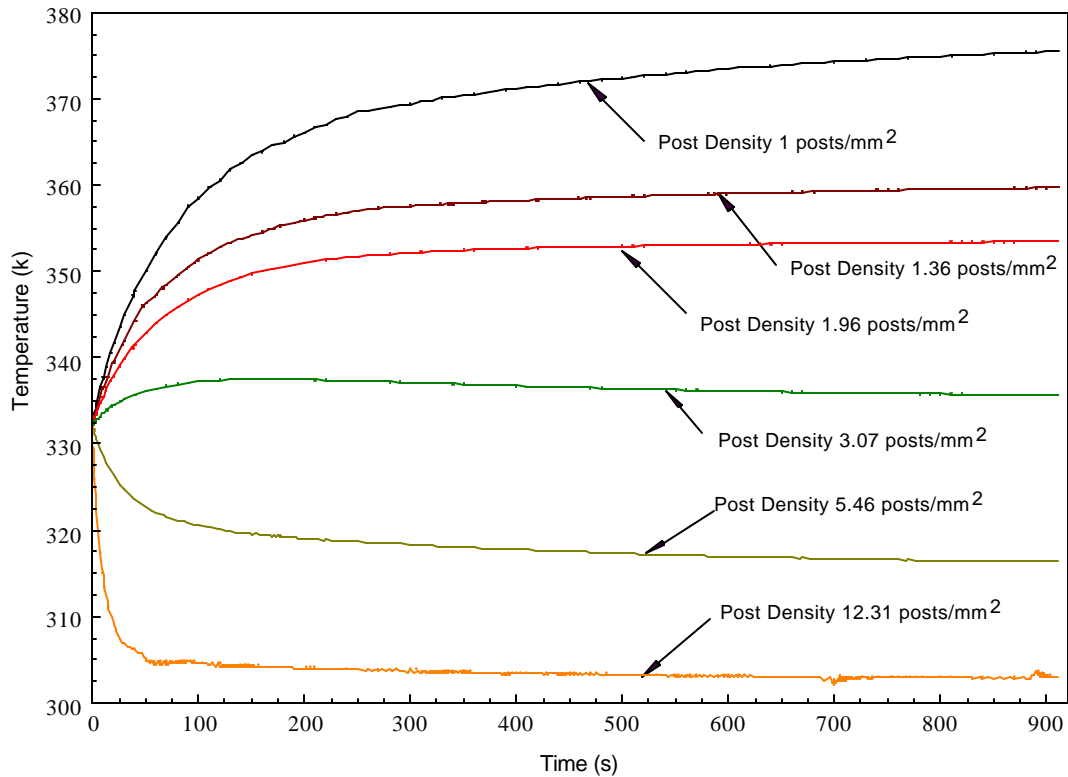


Figure 5.16 Temperature time responses for post density from 1 to 12.31 posts/mm²

In this simulation, we select post density range from 1 to 12.31 posts/mm² because the seal structures with post density of 1 posts/mm² and 12.31 posts/mm² had been successfully manufactured. The computations show, as seen in Figure 5.17, that a higher post density is always favorable from removing heat point of view in a seal prototype design. However, one must keep in mind the air flow requirement to keep the posts cool. In the limiting case when the post density approaches infinity, i.e. when the seal is simply a solid structure, the seal ring becomes a solid and there is no micro heat exchanger. The heat transfer calculation results for this situation are shown in figure 5.18. It shows that the steady state temperature will be much higher than that of post density of 12.31 posts/mm². Therefore, there must exist a maximum post density beyond which the coolant flow rate requirement is not satisfied. This post density is important in seals

structure design because the post distribution corresponds to this point has the highest heat transfer capability. Therefore this is an optimized post density from the heat transfer point of view.

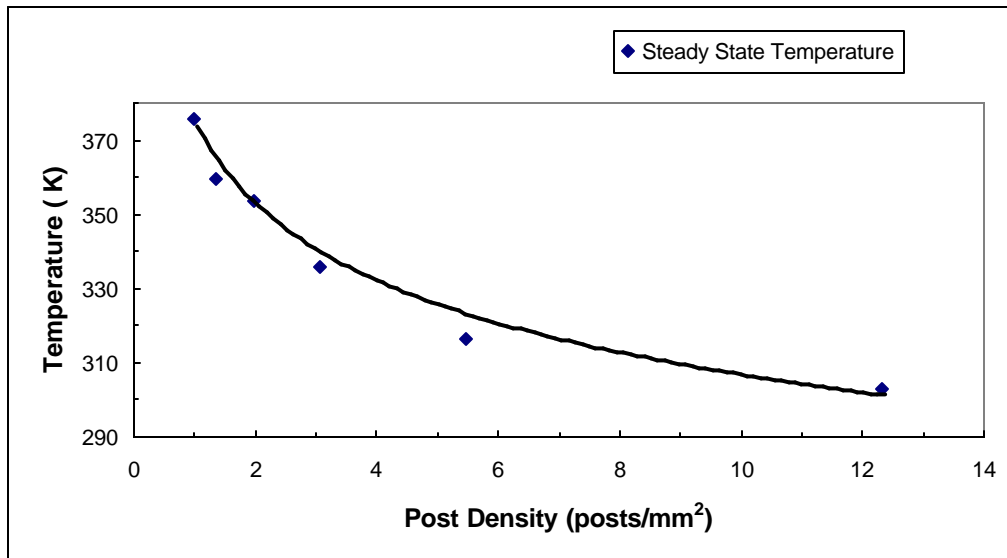


Figure 5.17 Post density and seal steady state temperature

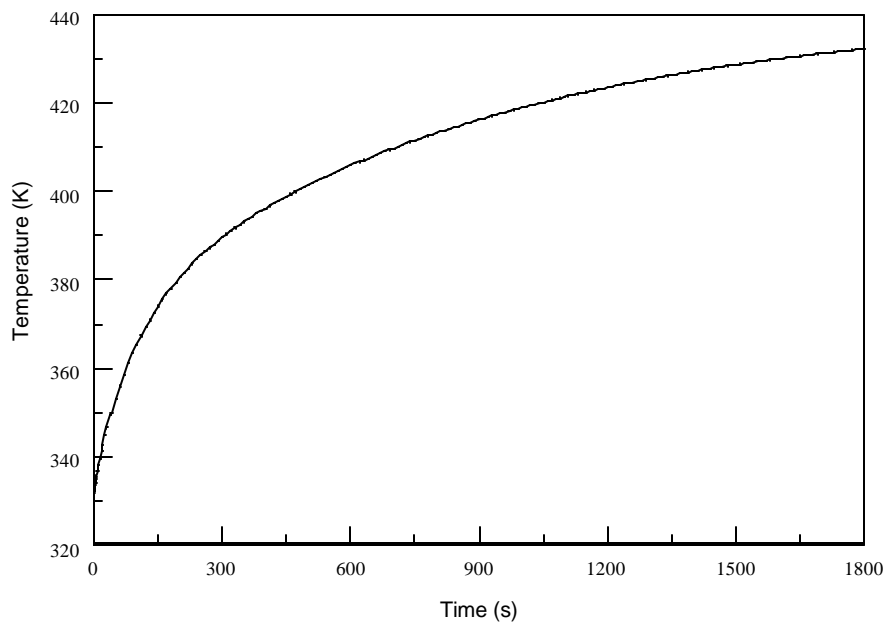


Figure 5.18 Temperature-Time curve of seal without micro heat exchanger

Since a greater post density is always favorable from the structure integrity point of view, the optimized post density for heat transfer mentioned in the last paragraph will be an overall optimal post density. The seal structures made according to this optimized post density will have a better performance than the current design. Future work is necessary to find out this optimal post density and the possibility of making such seal structures.

5.4.2.3 Nondimensionalization of The Heat Transfer Problem

In order to generalize the result for later use, the heat transfer equations were nondimensionalized according to the following method.

1. Nondimensionalization of the equations:

The nondimensionalization can be done on the basis of the formulation introduced in section 5.2.4. The governing equation of this problem is equation 5.13:

$$\frac{\partial^2 T}{\partial x^2} + \frac{\partial^2 T}{\partial y^2} + \frac{\partial^2 T}{\partial z^2} = \frac{r c_p}{k} \frac{\partial T}{\partial t} = \frac{1}{\mathbf{a}} \frac{\partial T}{\partial t}$$

Take r_o as reference length and $t_{ref} = \frac{r_o^2}{\mathbf{a}_s}$ as reference time, where $\mathbf{a}_s = \frac{k_s}{r_s c_{p_s}}$, let

$$\bar{x} = \frac{x}{r_o}, \bar{y} = \frac{y}{r_o}, \bar{z} = \frac{z}{r_o}, \bar{t} = \frac{t}{t_{ref}} \quad (5.45)$$

Let $\bar{T} = \frac{T_{ref} - T}{T_{ref} - T_i}$ where T_{ref} is reference temperature, in this case we select $T_{ref} = 0K$.

Therefore, nondimensionalized temperature becomes

$$\bar{T} = \frac{T}{T_i} \quad (5.46)$$

Substitute the above nondimensionalized factors into the governing equation yields:

$$\left(\frac{\partial^2 \bar{T}}{\partial \bar{x}^2} + \frac{\partial^2 \bar{T}}{\partial \bar{y}^2} + \frac{\partial^2 \bar{T}}{\partial \bar{z}^2}\right) = \frac{\mathbf{a}_s}{\mathbf{a}} \frac{\partial \bar{T}}{\partial \bar{t}} \quad (5.47)$$

This is the nondimensionalized governing equation.

According to section 5.2.4, four kinds of boundary conditions apply:

a). At boundaries 2,3,4 in Figure 5.6, the boundary condition is:

$$q_{conv} = -h(T - T_i)$$

After substituting nondimensional terms, the boundary condition becomes:

$$\bar{q}_{conv} = -\frac{r_o \cdot h}{k} (\bar{T} - 1) \quad (5.48)$$

where h is the convection heat transfer coefficient of air.

b). At boundary 8 in Figure 5.6, where the coolant flows across the micro posts, the nondimensionalized boundary condition becomes:

$$\bar{q}_{conv} = -\frac{r_o \cdot H_{eff}}{k} (\bar{T} - 1) \quad (5.49)$$

where H_{eff} can be obtained from section 5.2.3.

c). At boundaries 1,5,6,7,9 and 10 in Figure 5.6, where the surfaces are insulated from the environment, the nondimensionalized boundary condition becomes:

$$\bar{q} = 0 \quad (5.50)$$

d). At frictional interface 11 in Figure 5.6, the original boundary condition is:

$$k \frac{dT}{dz} = -q_1$$

$$k \frac{dT}{dz} = q_2$$

thus, the nondimensionalized boundary condition becomes

$$\frac{d\bar{T}}{d\bar{z}} = -\frac{r_o \cdot q_1}{k} \quad (5.51)$$

$$\frac{d\bar{T}}{d\bar{z}} = \frac{r_o \cdot q_2}{k}$$

The initial condition at $\bar{t} = 0$ becomes:

$$\bar{T} = 1 \quad (5.52)$$

By changing all the dimension terms and equations in the FLEXPDE code according to equation 5.45-5.52, the nondimensional solution for the heat transfer problem can be obtained.

2. Results:

The problem in section 5.4.2.1 is calculated using nondimensionalized modeling and the resulted time-temperature curves are plotted in Figure 5.19. The same conditions as in section 5.4.2.1 - rotating speed 3000 rpm and coolant mass flow rate 1.2 g/s - are used in this calculation for the purpose of comparison. Figure 2.10 shows the dimensional composite plot of time-temperature relationship obtained in section 5.4.2.1.

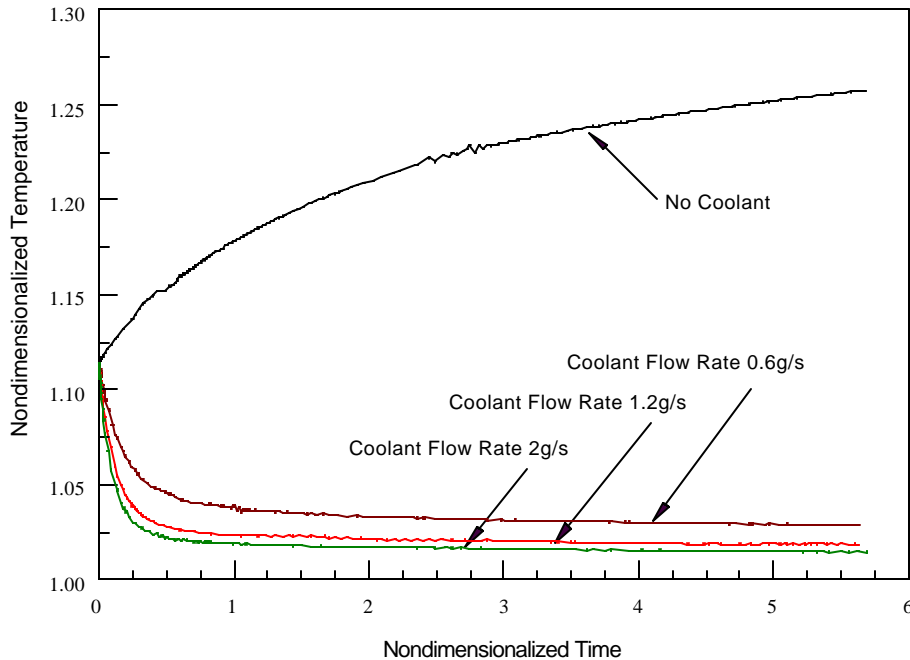


Figure 5.19 Non-dimensionalized temperature variation with time for different coolant flow rate

In the above case, the nondimensional factors for temperature and time can be obtained from equations 5.45 and 5.46. They are: 298 K and 76.4 seconds respectively. By multiplying these factors to the results in Figure 5.19 and comparing with Figure 5.20, we can see that the two results show a very good agreement.

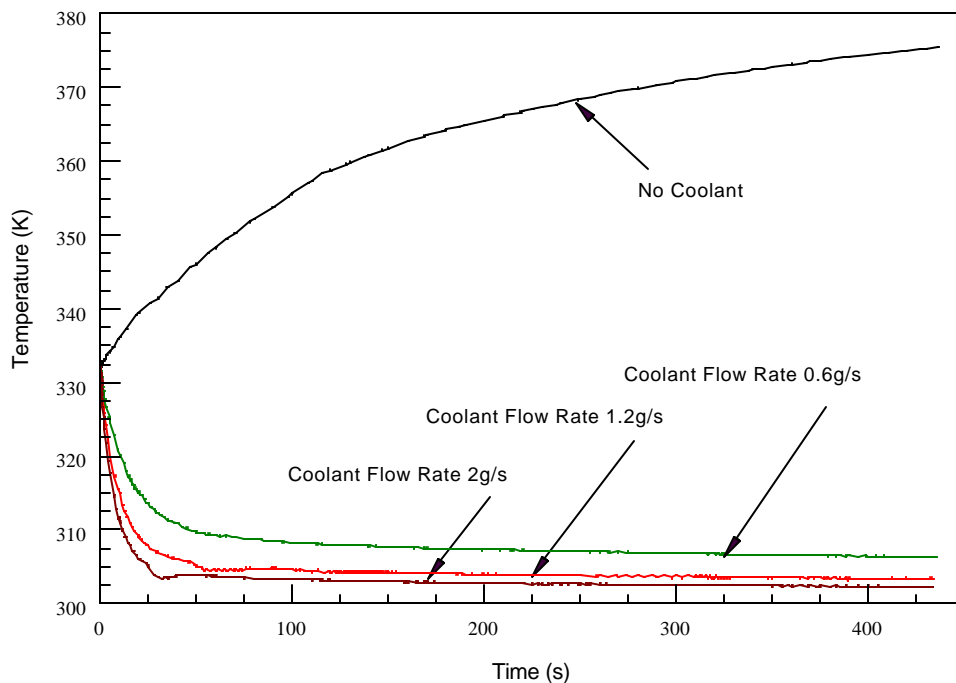


Figure 5.20 Dimensional temperature variation with time for different coolant flow rate

The nondimensionalization process can be applied to other rotating speed and coolant flow rate to create a series of time-temperature curves for use in seal structures design.

3. Implementation example

The nondimensionalized calculations can be used for predicting the operating temperature for micro heat transfer implanted seals of different dimensions. For instance, we assume the size of the seal changes in two situations: 1) enlarge to two times of its

original size and 2) shrink to $\frac{1}{2}$ of its original size. All other conditions such as heat generation, coolant flow rate (1.2g/s) remains the same. Since, according to equation 5.45, \bar{t} is proportional to $1/r_o^2$, in situation 1 above,

$$\bar{t}' = \bar{t} / 4 \quad (5.53)$$

in situation 2,

$$\bar{t}'' = 4 \cdot \bar{t} \quad (5.54)$$

By applying equations 5.53 and 5.54 to the nondimensional results and multiply them by the nondimensional factors, Figure 5.21 can be obtained.

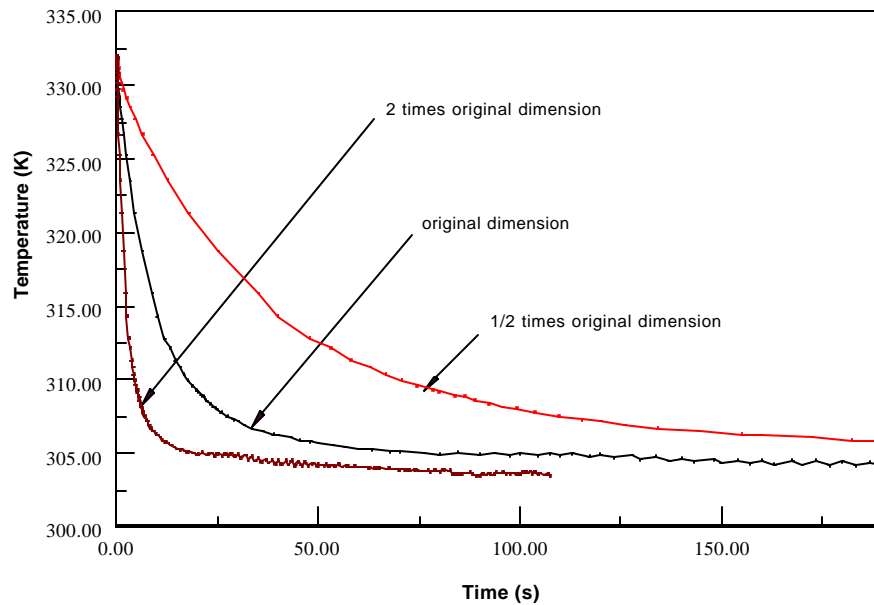


Figure 5.21 Dimensional temperature variation with time for different seal dimensions

In this way, time temperature curve of any seal dimensions can be derived from the original result as long as the other conditions and the relative dimension between all seal components remain the same.

In general, the nondimensionalization of the problem can provide us a quick and easy way to solve the similar problems using the data obtained in this thesis.

CHAPTER 6 SUMMARY AND CONCLUSION

6.1 Summary

In this thesis, the tribological properties of thin film coating Ti-C:H were tested in a universal tribometer. Instead of typical pin/ball on disk tests, ring on disk tests were carried out for testing the effect of coatings. A series of coatings with different metal Ti components were tested on disks of same material (1040 steel) under unlubricated condition. Both the coefficient of friction and wear were calculated from measured data. The result shows the following conclusions:

1. The coatings showed very good tribological properties with coefficient of friction in the range between 0.1 and 0.25 and wear rate of the counterparts of the coatings between 1×10^{-7} and 1×10^{-5} mm³/Nm. The coefficient of friction is much lower than 0.7, which is a typical value for mild steel on mild steel under unlubricated condition.
2. The coating worn out quickly in a typical of 1000 seconds under unlubricated condition because of the weakness in the coating-substrate bonding.
3. The wear mode of the coatings is thought to be a combination of adhesive wear and abrasive wear. The adhesive wear is the starting wear mode. It will tear the coating off its substrates where the coating-substrate bonding is the weakest.

Another subject of this work was the study of thermal performance and structural integrity of a seal structure with micro heat exchangers implanted underneath the surface. A three-dimensional finite element model was developed using a software package FLEXPDE to examine the transient heat transfer performance of the seal structure. A calculation method was developed for the calculation of maximum stress on micro posts. This method can be used for the failure prediction of the seal structure and seal structure

optimization. Finally, the effect of post density on both thermal performance and strength of the seal structure were studied. The following conclusion can be drawn:

1. By comparison with experimental results obtained by testing the first seal prototypes carried out by Kountouris (1999), the heat transfer model result closely matched the empirical result with an error of $\pm 5^{\circ}\text{C}$ for cases with coolant passing across the posts.
2. Both the empirical result and calculation result shows that the heat transfer capacity of the mechanical seal was greatly enhanced with implanted micro posts.
3. Simulations show that for the post density from 1~12.3 posts/mm², increasing post density enhanced the structural strength and thermal performance of the seal.
4. Simulations show that the strength of a seal structure will increase with the increase of post density.

6.2 Recommendations of Future Work

The following works are thought to be necessary in the future:

1. The bonding strength between the coating and the substrate should be examined both experimentally and analytically. The coating method should be modified to enhance this bonding strength to make the coatings more realistic in the practice.
2. The heat transfer model for micro heat exchanger needs to be improved to include the consideration for wear of the interface. Optimized post density from structural and heat transfer point of view needs to be found.
3. The bonding strength between the posts and their substrates should be studied so that the method found in this research can be used to predict failure of the seal structure.

REFERENCES

- Bhushan, B., *Principles and Applications of Tribology*, John Wiley & Sons, New York, 1999, pp. 344-387, 474-585, 812-823, 896-928.
- Bisson, E.E., "Various Modes of Wear and Their Controlling Factors," *Evaluations of Wear Testing*, ASTM STP 446, American Society for Testing and Materials, 1969, pp. 1-22.
- Buck, S.G., "Estimating Heat Generation, Face Temperature and Flush Rate for Mechanical Seals", *Proceedings of PumpUsers Expo '99*, 1999, pp. 167-172.
- Bucks, S.G., "Materials for Seal Faces", *Pumps and Systems*, Jan. 2001, pp. 22-26.
- Bunshah, R.F., "Selection and Use of Wear Tests for Coatings", Selection and Use of Wear Tests for Coatings, ASTM STP 769, R.G. Bayer, Ed., American Society for Testing and Materials, 1982, pp.3-15.
- Bunshah, R.F., *Handbook of Hard Coatings*, Noyes Publications/ William Andrew Publishing, LLC, 2001, Norwich, NY. pp. 5-70, 229-341.
- Cao, D.M., Feng, B., Meng, W.J., Rehn, L.E., Baldo, P.M., Konsari, M.M., "Friction and Wear Characteristics of Ceramic Nanocomposite Coatings: Titanium Carbide/Amorphous Hydrocarbon", *Applied Physics Letters*, Vol. 79, No. 2, 2001, pp. 1-3.
- Etsion, I., Kligerman, Y., Halperin, G., "Analytical and Experimental Investigation of Laser-textured Mechanical Seal Faces", *Tribology Transactions*, Vol. 42, Iss. 3, 1999, pp 511-516.
- Evens, A.G., Marshall, D.B., "Wear Mechanisms in Ceramics", In *Fundamentals of Friction and Wear of Materials*, American Soc. Metals, Metals park, Ohio, 1981, pp. 439-452.
- Feng, B., "Microstructure Characterization and Mechanical Properties of Ceramic Nanocomposite Coatings", Thesis, Louisiana State University: Baton Rouge, 2001, pp. 39-42.
- Hagen, K.D., *Heat Transfer with Applications*, Prentice-Hall, Inc. Upper Saddle River, NJ, 1999, pp. 271-287.
- Heinrich, J., Roseneelder, O., Benker, W., Schelter, H., "Aspects of Material and Design of Optimized Silicon-carbide Seal Rings", *Lubrication Engineering*, Vol., 47, Iss. 5, 1991, pp 367-372.
- Jones, J. T. and Berard, M.F., *Ceramics-Industrial Processing and Testing*, Iowa State University Press, Ames, Iowa, 1972, p. 147.

Kelly, P.J., Arnell R.D., Hudson, M.D., Wilson, A.E.J., Jones, G., “Enhanced Mechanical Seal Performance Through CVD Diamond Films”, *Vacuum*, Vol. 61, 2001, pp 61-74.

Kountouris, D., “Fabrication Modeling and Testing of A Thrust Bearing Surface With Integral Micro Heat Exchanger”, Thesis, Louisiana State University: Baton Rouge, 1999, pp. 21-25, 61-93.

Stephens S.L., Kelly W.K., Demetris K., Jeff M., “A Pin Fin Microheat Sink for Cooling Macroscale Conformal Surfaces Under the Influence of Thrust and Frictional Force”, *Journal of Microelectromechanical System*, Vol. 10, No. 2, 2001, pp.222-231

Stephens S.L., Kelly W.K., Seshu S., Andy B.M., Meletis E.I., “Mechanical Property Evaluation and Failure Analysis of Cantilevered LIGA Nickel Microposts”, *Journal of Microelectromechanical System*, Vol. 10, No. 3, September 2001, pp. 347-359.

Madou, Marc J., *Fundamentals of Microfabrication*, CRC Press LLC, Boca Raton, 1997, pp. 275-309.

Marques, C., “Heat Transfer of A Microstructure-covered Cylinder in Crossflow”, Thesis, Louisiana State University: Baton Rouge, 1997, pp. 5-49.

Meng, W.J., Tittsworth, R.C., Rehn, L.E., “Mechanical Properties and Microstructure of TiC/amorphous Hydrocarbon nanocomposite Coatings”, *Thin Solid Film*, 377-378, 2000, pp.222-232.

Merati, P., Okita, N.A., Phillips, R.L., Jacobs, L.E., “Experimental and Computational Investigation of Flow and Thermal Behavior of A Mechanical Seal”, *Tribology Transaction*, 1999, Vol. 42, Iss 4, pp. 731-738.

Merchant, M.E., “The Mechanism of Static Friction”, *Journal of Applied Physics*, Vol. 11, No.3, 1940, p. 230.

Peterson, M.B., Winer, W.O., *Wear Control Handbook*, ASME, New York, 1980, pp. 727-754.

Phillips, R.L., Jacobs, L.E., Merati, P., “Experimental Determination of the Thermal Characteristics of A Mechanical Seal and Its Operating Environment”, *Tribology Transaction*, Vol. 40, Iss 4, 1997, pp. 559-568.

Rabinowicz, E., *Friction and Wear of Materials*, John Wiley and Sons, Inc, New York, 1965, pp.118-119

Warring, R.H., *Seals and Sealing Handbook*, Gulf Publishing Company, Houston, 1981, pp. 237-270

Turcotte, H.L., Wilson, H.B., *Computer Applications in Mechanics of Materials Using MATLAB*, Prentice Hall, Upper saddle River, 1998, pp.31-38.

APPENDIX 1

FLEXPDE CODE FOR MICRO HEAT EXCHANGER HEAT TRANSFER CALCULATION

1. FLEXPDE Code Outline

FLEXPDE code is written according to the method introduced in section 5.2.. The code is composed of several blocks as shown in Appendix I. In the coordinates block, coordinate geometry is defined. Here 3D cartesian coordinate (X,Y,Z) is used. In the selects block, some selections, such as accuracy of the calculation and elements type for meshing, are made to control the program. Quadratic elements are used for this calculation. In the variables block, the only variable in this problem – temperature – is defined. In the definitions block, all the constants, coefficients are given values and values of certain indirect parameters such as coefficient of heat convection in the seal structure are calculated. In the initial value section, variable temperature is given an initial value. In the equations section, the governing equation (in our case, equation 5.13) is defined. The extrusion section defines layers and surfaces for 3D modeling. In the boundaries section, geometry domains are defined and boundary conditions associated with those domains are given. In the last few sections, parameters been monitored during the calculation process, results been plotted and summery of some parameters after the calculation and time response of the variable are defined.

2. FLEXPDE Code

```
title 'Heat exchanger'  
coordinates  
    cartesian3  
select  
    GRIDARC=90
```

nodelimit=5000
 thermal_colors painted
 variables
 temp
 definitions

k_Ni = 91.7	{thermal conductivity for Ni (W/mK)}
cp_Ni = 461	{heat capacity for Ni (J/kgK)}
ro_Ni = 8900	{density of Ni (kg/m ³)}
k_Cu = 393	{thermal conductivity for Cu (W/mK)}
cp_Cu = 385.2	{heat capacity for Cu (J/kgK)}
ro_Cu = 8933	{heat capacity for Cu (kg/m ³)}
k_Fe = 16.3	{thermal conductivity for Fe (W/mK)}
cp_Fe = 502	{heat capacity for Fe (J/kgK)}
ro_Fe = 7850	{heat capacity for Fe (kg/m ³)}
k_Al = 170	{thermal conductivity for Al (W/mK)}
cp_Al = 880	{heat capacity for Al (J/kgK)}
ro_Al = 2702	{heat capacity for Al(kg/m ³)}
rho=ro_Fe	
Hf = 40	{free convection boundary coupling}
Ta = 25+273	{ambient temperature}
f=0.1	{Frition coefficient}
nrot=3000	{Rotating speed}
fn=10*0.45*9.8	{Normal Load}
ro=1.4*25.4e-3/2	{outside diameter of lower piece}
ri=1.043*25.4E-3/2	{inside diameter of lower piece}
rco=ro	
rci=ri	
ph=0.5e-3	{Post height}
pd=0.18e-3	{Post diameter}
ps=0.285e-3	{Distant between posts}
oh=0.3e-3	{Overplate thickness}
htu=0.6*25.4e-3	{upper piece height}
htd=1.072*25.4e-3	{lower piece height}
hb=1*25.4e-3	{Bottom plate thickness}
db=0.8*25.4e-3	
odal=1.655*25.4e-3	{Outside dia. of Al bush}
idal=ro*2	
hal=0.6*25.4e-3	{Al bush height}
a=pi*(rco ² -rci ²)	

```

press=fn/a
v=nrot*pi*(rci+rco)/60
heat=f*press*v
pv=press*v
Af=2*pi*(rci+rco)/2*ph*(ps-pd)/ps

! Different coolant flow rate
md4=0.6742e-3
md5=1.191e-3
md6=2e-3

! *****
!Below are for the calculation of convection heat transfer coefficient
!inside heat exchanger
!*****

md=md6
mu=184e-7
K_Air=26.3e-3
Pr=0.7
re=md*pd/Af/mu
Fc=1
Cc=if (re<500 and re>=1) then 1.04 else if (re>=500 and re<1000) then 0.71 else
0.35
m=if (re<500 and re>=1) then 0.4 else if (re>=500 and re<1000) then 0.5 else 0.6
n=0.36
Nu=Fc*Cc*re**m*Pr**n
{Nu=0.0649*re**0.8267}
{Nu=0.0197*re**1.0017}

Heff0=Nu*k_Air/pd
Heff=1
H=Heff
k=k_Ni
cp=cp_Ni
! *****

an = ps/ri          { this is the angular size of the repeated segment }
crot = cos(an)     { the sine and cosine needed in the transformation }
srot = sin(an)
dbx=db*cos(an/2)
dby=db*sin(an/2)
rix=ri*cos(an/2)
riy=ri*sin(an/2)
rcix=rci*cos(an/2)
rciy=rci*sin(an/2)
rox=ro*cos(an/2)
roy=ro*sin(an/2)

```

```

rcox=rco*cos(an/2)
rcoy=rco*sin(an/2)
stax=10e-3*cos(an/2)
stay=10e-3*sin(an/2)
mesh_spacing = 50e-3

```

initial value

```
temp = 332          {initial temperature}
```

equations

```
div(k*grad(temp)) =rho* cp*dt(temp)
```

EXTRUSION

```

SURFACE  "m4"  Z=-htd-hb
  LAYER   "m34"
SURFACE  "m3"  Z=-htd
  LAYER   "m23"
SURFACE  "m2"  Z=-oh-ph
  LAYER   "m12"
SURFACE  "m1"  Z=-oh
  LAYER   "m01"
SURFACE  "pm0" Z=0
  LAYER   "p10"
SURFACE  "p1"  Z=htu

```

BOUNDARIES

region 5

```

layer "m34" k=k_Fe H=Hf rho=ro_Fe cp=cp_Fe
layer "m23" void
layer "m12" void
layer "m01" void
layer "p10" void

```

```

start (stax,-stay)
line to (dbx,-dby)
natural(temp) = -H*(temp - Ta)
arc(center=0,0) to (dbx,dby)
nobc(temp)
periodic(x*crot+y*srot, -x*srot+y*crot)
line to (stax,stay)
line to finish

```

region 4

```

surface "m2" natural(temp) = -Heff*(temp - Ta)
surface "m1" natural(temp) = -Heff*(temp - Ta)

```

```

layer "m34" k=k_Fe H=0 rho=ro_Fe cp=cp_Fe
layer "m23" k=k_Fe H=Hf rho=ro_Fe cp=cp_Fe
layer "m12" void
layer "m01" k=k_Ni H=Hf rho=ro_Ni cp=cp_Ni
layer "p10" void

```

```

start (rix,-riy)
line to (rox,-roy)
natural(temp) = -H*(temp - Ta)
arc(center=0,0) to (rox,roy)
nobc(temp)
line to (rix,riy)
natural(temp) = 0
arc(center=0,0) to finish

```

region 1 'up'

```

SURFACE "pm0" natural(temp)=heat

```

```

layer "m34" k=k_Fe H=0 rho=ro_Fe cp=cp_Fe
layer "m23" k=k_Fe H=0 rho=ro_Fe cp=cp_Fe
layer "m12" void
layer "m01" k=k_Ni H=0 rho=ro_Ni cp=cp_Ni
layer "p10" k=k_Cu H=Hf rho=ro_Cu cp=cp_Cu

```

```

start (rcix,-rciy)
line to (rcox,-rcoy)
natural(temp)=0
arc(center=0,0) to (rcox,rcoy)
line to (rcix,rciy)
natural(temp) = 0
arc(center=0,0) to finish

```

region 3

```

layer "m34" k=k_Fe H=0 rho=ro_Fe cp=cp_Fe
layer "m23" k=k_Fe H=0 rho=ro_Fe cp=cp_Fe
layer "m12" k=k_Ni H=Heff rho=ro_Ni cp=cp_Ni
layer "m01" k=k_Ni H=0 rho=ro_Ni cp=cp_Ni
layer "p10" k=k_Cu H=0 rho=ro_Cu cp=cp_Cu

```

```

repeat i=0 to 14
  start (ri+(i+0.5)*ps-0.5*pd,0)
  natural(temp) = -H*(temp - Ta)
  arc (center= (ri+(i+0.5)*ps),0) angle=360 to finish
endrepeat

```

time 0 to 1200 by 10

monitors

for t = 0 by 10 to 1200

contour(temp) on surface z=0

contour (temp) on surface y=0 as "temp"

plots

for t = 0 by 10 to 1200

elevation(Temp) from (ri+2.5e-3,0,-htd) to (ri+2.5e-3,0,htu) as "Temp"

grid(x,y,z)

contour(temp) on surface z=0.4e-3

contour(temp) on surface z=-0.2e-3

contour(Temp) on y=0 zoom(rix,-2e-3,5e-3,5e-3)

elevation(k_Ni*(dz(temp))) from (ri,0,-1e-4) to (ro,0,1e-4) as "Heat Flux"

summary

report (re) as "raynolds"

report (Cc) as "Cc"

report (m) as "m"

report (Heff) as "Heff"

report (Heat) as "Total Heat"

histories

history(temp) at (ri+2.5e-3,0,1e-3) export format "#t#r,#i"

end

APPENDIX 2 MATLAB CODE 1

```

%Calculation for maximum shear stress on top of posts
clear all;
clc;
format long;
pi=3.14159;

n=10;
mu=0.1;

%ad=800e-6;
ad=[0.285e-3:0.143e-3:1e-3];
%ad=[0.3e-3:0.05e-3:0.8e-3];
[na,nt]=size(ad);

for k=1:nt
ro=1.4*25.4e-3/2;
ri=1.043*25.4e-3/2;

p_tot=0;

cir_nr=floor((ro-ri)/ad(k))
dr=(ro-ri)/cir_nr;

ri=ri-0.5*dr;
p_nr=zeros(cir_nr,1);
cir_rad=zeros(cir_nr,1);
p_dia=zeros(cir_nr,1);
for i=1:cir_nr
    cir_rad(i)=ri+i*dr;
    p_nr(i)=floor(pi*2*cir_rad(i)/ad(k));
    p_tot=p_tot+p_nr(i);
    p_dia(i)=180e-6;

end

cir_rad
p_nr
p_tot

%%%%%%%%%%%%%%%%%%%%%%%%%%%%%%%%%%%%%%%%%%%%%%%%%%%%%%%%%%%%%%%%%%%%%%%%
torque=2*mu*n*(ro^3-ri^3)/3/(ro^2-ri^2);
cir_nr=length(p_nr);

```

```

b=zeros(cir_nr,1);
a=zeros(cir_nr,cir_nr);

for i=1:cir_nr-1
    for j=1:cir_nr
        if i==j
            a(i,j)=cir_rad(i+1);
        end
        if i==j-1
            a(i,j)=-cir_rad(i);
        end
    end
end

b(cir_nr)=abs(torque);
a(cir_nr,:)=(p_nr.*(pi/4*cir_rad).^2);

tau=a\b;
tau=tau'

taumax(k)=tau(i+1);
p_t(k)=p_tot;
c_n(k)=cir_nr;
%fprintf('shear stress is %8.6f MPa\n',tau/1e6);
end
%%%%%%%%%%
fprintf('Max. shear stress is %8.6f MPa\n',taumax/1e6);

```

APPENDIX 3 MATLAB CODE 2

```

% Calculate maximum normal force and torque a seal can sustain
clear all;
clc;
pi=3.14159;
n=10;
mu=0.1;
ph=0.5e-3;
ad=[0.285e-3:0.143e-3:1e-3];
[na,nt]=size(ad);

for j=1 : nt
ro=1.4*25.4e-3/2;
ri=1.043*25.4E-3/2;

a=ad(j);
b=a;
p_tot=0;

cir_nr=floor((ro-ri)/a);
dr=(ro-ri)/cir_nr;

ri=ri-0.5*dr;

for i=1:cir_nr
    cir_rad(i)=ri+i*dr;
    p_nr(i)=floor(pi*2*cir_rad(i)/b);
    p_tot=p_tot+p_nr(i);
    p_dia(i)=180e-6;

end

cir_rad
p_nr
p_tot
As=pi*p_dia(1)^2/4;
%%%%%%%%%%%%%%%%%%%%%%%%%%%%%%%%%%%%%%%%%%%%%%%%%%%%%%%%%%%%%%%%%%%%%%%%
taomax=59e6;

sum=0;
for i= 1:cir_nr
    sum=sum+p_nr(i)*cir_rad(i)^2;
end

x=1/p_tot/As+32*mu*(ro^3-ri^3)*cir_rad(cir_nr)...

```

```
*ph/pi/p_dia(1)^3/(ro^2-ri^2)/sum;  
Nf(j)=taomax/x;  
T(j)=2*mu*(ro^3-ri^3)*Nf(j)/(ro^2-ri^2)/3;  
  
p_t(j)=p_tot;  
  
cir_rad=0;  
p_nr=0;  
p_tot=0;  
end  
  
fprintf('Normal force is %8.3f N\n',Nf);  
fprintf('Torque is %8.3f N.m\n',T);
```

APPENDIX 4 CALCULATION OF WEAR RATE

The wear rate obtained in chapter 3 of this thesis was the value of volume of material loss per unit distant of sliding per unit normal load. It was calculated from equation 3.3 in which normal load P , rotating speed V and operation time t were preset in the experiment and thus were known. The volume loss was obtained by measuring the wear scar using a stylus surface profiler.

The wear scar was a circular ring of which the width was approximately 2mm. The cross section of the wear scar was measured using a TENCOR ALFA-STEP surface profiler, which had a horizontal resolution $2\ \mu\text{m}$ and a vertical resolution $1\ \mu\text{m}$. A typical wear scar cross-section profile measured from the stylus profiler is shown in Figure A1.

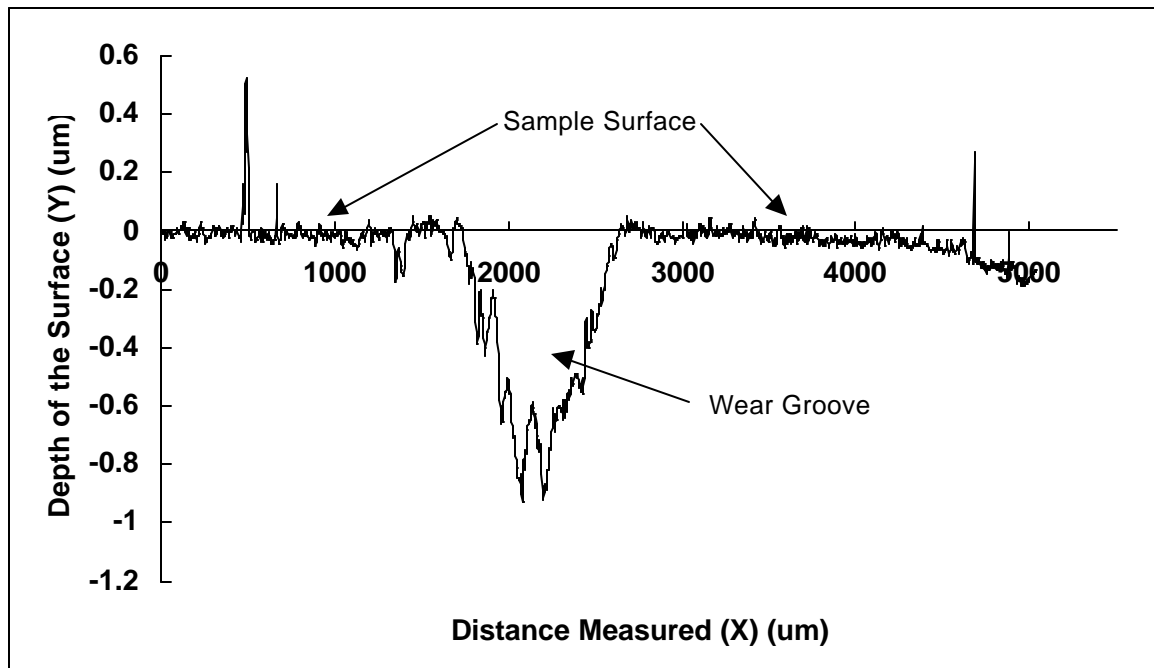


Figure A1 Typical wear groove cross-section obtained from stylus profiler

Because the groove depth data was sampled every two micrometers in X direction, the wear groove cross-section area was computed from

$$A = \sum_{i=a}^b h_i x$$

where a and b were the sample number of the starting and ending of the wear groove, h_i was the depth of every sample point within sample point a and b, x was equal to 2 micron.

The volume loss was then calculated from

$$\Delta n = 2p R_{avg} A$$

where R_{avg} was the average radius of wear groove. Total of four measurements were done for each sample. Four volume losses were calculated and the average of them was taken as the final result.

Then using equation 3.3, the wear rate was calculated.

VITA

Qiu, Yifan was born on January 1st, 1972, in Beijing, People's Republic of China. In July 1990, he finished high school and was accepted in the Mechanical Engineering Department at Science and Technology University, Beijing. After obtaining his bachelor of engineering degree from the university in 1994, he was employed by the Beijing Central Engineering and Research Incorporation of Iron and Steel Industry as a mechanical engineer. He worked for five years before starting his graduate study in Mechanical Engineering Department at Louisiana State University in 1999. Now, he is a candidate for the degree of Master of Science in Mechanical Engineering, which will be conferred in May, 2002.